JOURNAL OF PETROLOGY

Journal of Petrology, 2021, 1–33
doi: 10.1093/petrology/egaa114
Advance Access Publication Date: 8 January 2021
Original Manuscript

OXFORD

Mineralogy Constraints on Magmatic Processes Controlling Adakitic Features of Early Permian High-magnesium Diorites in the Western Tianshan Orogenic Belt

Peng-Li He[1,2], Xiao-Long Huang [1,2,*], Fan Yang[1,2] and Xue Wang[1,2]

[1]State Key Laboratory of Isotope Geochemistry, Guangzhou Institute of Geochemistry, Chinese Academy of Sciences, Guangzhou, 510640, China; [2]CAS Center for Excellence in Deep Earth Science, Guangzhou, 510640, China

*Corresponding author. E-mail address: xlhuang@gig.ac.cn

Received 13 January 2020; Accepted 21 December 2020

ABSTRACT

Whole-rock geochemistry, usually changed by magmatic processes, might provide misleading information on the petrogenesis of adakites. The Heishantou porphyritic diorites in Nileke, Western Tianshan orogenic belt record complex magma chamber processes, such as magma replenishment, fractional crystallization and crustal contamination, and thus, provide ideal samples for tracing the magmatic processes that generate the typically high Sr and La contents and Sr/Y and La/Yb ratios of adakites. *In situ* clinopyroxene and amphibole compositions of Heishantou porphyritic diorites (271 ± 2 Ma) are characterized by low Yb and Y content with high Sr/Y and La/Yb ratios, from which calculated early magmas resemble typical adakites derived from partial melting of a subducted slab. But whole-rock composition shows low MgO, Ni and Cr, thus, the Heishantou diorites were previously regarded as the result of partial melting of thickened lower crust. Plagioclase phenocrysts exhibit complex compositional zoning due to magma replenishment, and the rims have higher $^{87}Sr/^{86}Sr$ ratio and Sr content than the cores, indicating crustal assimilation. The cores of zoned clinopyroxene phenocrysts have high $Mg^{\#}$, Cr and Ni but low Yb and Y with high Sr/Y and La/Yb ratios, which are consistent with the high $Mg^{\#}$ of primary adakitic magmas. Magmatic processes have significantly changed the primary adakitic features of Yb, Y and Sr content, Sr/Y and La/Yb ratios, in addition to $Mg^{\#}$ values. The Heishantou primitive high-$Mg^{\#}$ adakite was derived from partial melting of a delaminated lower crust followed by storage, recharge, and assimilation in a crustal magma chamber. The Western Tianshan orogenic belt experienced a succession of lower crust delamination events in the Early Permian that involved melting of thickened lower crust, subsequent lithospheric detachment and asthenospheric upwelling.

Key words: adakitic diorite; compositional zoning; delaminated lower crust; magmatic processes; Western Tianshan orogenic belt

INTRODUCTION

Adakite originally refers to intermediate to felsic rocks derived from the partial melting of relatively young (≤ 25 Ma) subducted oceanic crust (Defant & Drummond, 1990). These rocks have pronounced high Sr (>400 ppm), low heavy rare earth elements (HREE; Yb ≤ 1·8 ppm) and Y (≤ 18 ppm), and show strongly fractionated REE patterns ($[La/Yb]_N$ > 10; Defant &

Drummond, 1990). However, some igneous rocks with such geochemical features might be petrogenetically unrelated to subducted oceanic crust, but instead derived from the partial melting of delaminated lower crust (Xu *et al.*, 2002; Wang *et al.*, 2006a), thickened lower crust (Atherton & Petford, 1993; Hou *et al.*, 2004; Wang *et al.*, 2005; Huang *et al.*, 2009) or adakitic crust (Moyen, 2009; Ma *et al.*, 2015). In general, adakites from different tectonic settings show distinctive geochemical features (e.g. Defant & Drummond, 1990; Martin, 1999; Wang *et al.*, 2007a), and some diagrams based on whole-rock geochemical data, such as SiO_2 vs MgO (or $Mg^{\#}$), Ni and Cr, have been widely used to distinguish their tectonic settings (e.g. Kay & Kay, 2002; Wang *et al.*, 2007a; Huang *et al.*, 2009; Long *et al.*, 2015). However, magmatic processes such as magma mixing, crustal assimilation, and garnet and/or amphibole fractional crystallization might also produce adakitic features, such as high Sr/Y and La/Yb ratios, or change the MgO (or $Mg^{\#}$), Ni, and Cr content in the rocks (Castillo *et al.*, 1999; Macpherson *et al.*, 2006; Rodriguez *et al.*, 2007; Streck *et al.*, 2007; Rooney *et al.*, 2011). Whole-rock geochemistry usually loses the record of early magmatic processes, thus, may provide misleading clues on petrogenesis and related tectonic settings. In contrast, *in situ* mineral compositions record detailed magmatic processes, such as magma mixing, recharging, contamination, and residence time in the magma chamber (e.g. Davidson *et al.*, 2001, 2007; Ramos *et al*, 2005; Charlier *et al.*, 2008). Such processes could have shaped the primary features of adakitic magmas that are key for identifying their petrogenetic and tectonic evolutionary histories.

In this study, we focus on the high-$Mg^{\#}$ adakitic rocks in the Heishantou area of Western Tianshan orogen in the southwestern part of the Central Asian Orogenic Belt (CAOB) (Fig. 1c), which were initially proposed to be derived from partial melting of either a thickened mafic lower crust (Zhao *et al.*, 2008; Tang *et al.*, 2017b) or delaminated lower crust (Li *et al.*, 2019). The Heishantou adakitic rocks contain abundant clinopyroxene, both as phenocrysts and matrix crystals, and minor amphibole phenocrysts. Such a mafic mineral assemblage is possibly related with primitive adakites and probably records the details of early magmatic processes that could have shaped the primary features of adakitic magmas. Thus, the Heishantou adakitic rocks are ideal object for testing the petrogenesis of adakites by using mineral geochemistry. We present *in situ* elemental and Sr isotopic compositions of plagioclase, amphibole and clinopyroxene phenocrysts and whole-rock major, trace elemental and Sr–Nd–Hf isotopic data of the Heishantou adakitic rocks to investigate their primary features, magma sources and magmatic processes, and to constrain the Permian tectonic evolution of the Western Tianshan orogenic belt. In addition, we investigate how magmatic processes affect the adakitic signatures of these rocks.

GEOLOGICAL BACKGROUND AND SAMPLE DESCRIPTION

Geological background

The CAOB (Zonenshain et al., 1990), situated between the European, Siberian, Tarim and North China cratons (Fig. 1a), is the largest Phanerozoic accretionary orogeny, which formed through long-term accretion of arcs, accretionary complexes, seamounts, oceanic plateaus and continental blocks (Coleman, 1989; Sengör *et al.*, 1993; Xiao & Santosh, 2014). The Chinese Tianshan Orogen, located in the southwestern part of the CAOB, separates the Tarim Basin to the south and the Junggar Basin to the north (Fig. 1a, b). There are four tectonic units recognized in the western segment of the Chinese Tianshan Orogen (Western Tianshan), including the North Tianshan, Yili Block, Central Tianshan and South Tianshan, which are respectively separated by the North Tianshan Suture, the North Nalati Suture, and the South Central Tianshan Suture from north to south (Fig. 1b; Allen *et al.*, 1993; Gao *et al.*, 2009). The details of these four tectonic units are described in previous literature (Han et al., 2011; Xiao *et al.*, 2013; He *et al.*, 2016). There are intense debates about the details of the Permian tectonic evolution of the Western Tianshan, such as whether the subduction of the South Tianshan ocean was completed by then (e.g. Gao *et al.*, 2009; Han *et al.*, 2011; Xiao *et al.*, 2013; Xiao & Santosh, 2014) and whether the Tarim mantle plume played a role in the widespread Permian magmatism in the area (e.g. Qin *et al.*, 2011; Zhang & Zou, 2013a, b; Zhang *et al.*, 2014; He *et al.*, 2016; Xue *et al.*, 2016; Zheng et al., 2016; Han et al., 2019). The presence of Permian bimodal volcanic rocks and A-type granitoids in the Tianshan Orogen is likely consistent with a post-orogenic setting (Long *et al.*, 2011; Gou *et al.*, 2012; Zhang & Zou, 2013a, b; Li *et al.*, 2015a; Xia *et al*, 2016). However, the detailed mechanism for these magmatisms is poorly constrained.

Adakitic rocks in the Tianshan Orogen were mostly formed during the Paleozoic. Pre-Permian adakitic rocks are mainly distributed in the Dananhu arc in the eastern segment of the Chinese Tianshan Orogen (Eastern Tianshan) (e.g. Xiao *et al.*, 2017; Zhang *et al.*, 2020) and sporadically scattered in the Western Tianshan (Fig. 1; Wang *et al.*, 2007b; Qian *et al.*, 2009; Tang *et al.*, 2010; Xie *et al.*, 2013; Xu *et al.*, 2013; Yin *et al.*, 2016, 2017; Li *et al.*, 2019). Most of them show depleted whole-rock Sr–Nd isotopes and were interpreted to be derived from partial melting of subducted oceanic crust (Wang *et al.*, 2007b; Xu *et al.*, 2013; Yin *et al.*, 2016, 2017; Li *et al.*, 2019). Those with enriched Sr–Nd isotopes might be attributed to crustal assimilation (Tang *et al.*, 2010; Xie *et al.*, 2013) or be derived from the partial melting of thickened lower crust (Qian *et al.*, 2009). Permian adakitic rocks in the Tianshan orogen are relatively rare and were interpreted as continental crust related magmatism in post-orogenic setting (Huang *et al.*, 2012; Tang *et al.*, 2017b; Li *et al.*, 2019; Fig. 1). Among them, some

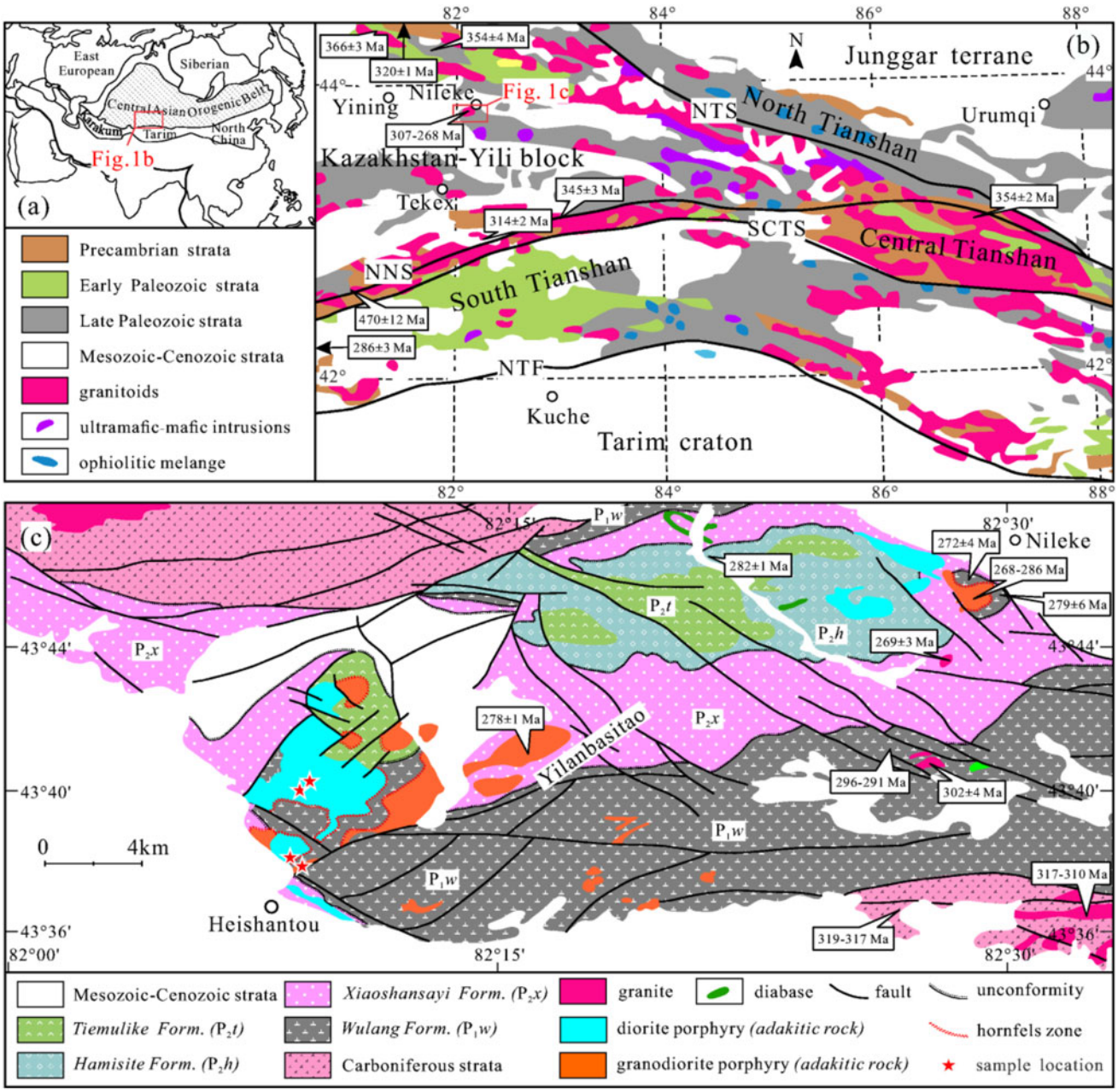

Fig. 1 (a) Tectonic sketch map of the Central Asia Orogenic Belt (modified after Xiao *et al.*, 2013). (b) Geological map of the Western Tianshan orogenic belt in China–Kyrgyzstan contiguous regions (modified from Gao *et al.*, 2009). Abbreviations: NTS, North Tianshan Suture; NNS, Nikolaev Line–North Nalati Suture; SCTS, South Central Tianshan Suture; NTF, North Tarim Fault. (c) Simplified geological map of the southwest Nileke area, showing rock types, strata and sample locations (modified after Gongliu Geological Map at 1:200000 scale; BGMRXUAR, 1979). Geochronological data of adakitic rocks in the Western Tianshan are from Zhao *et al.* (2003), Wang *et al.* (2007b), Qian *et al.* (2009), Tang *et al.* (2010, 2017b), Huang *et al.* (2012), Xie *et al.* (2013), Xu *et al.* (2013), Yin *et al.* (2016, 2017) and Li et al. (2019). Geochronological data of magmatic rocks in the Nileke area are from Zhao *et al.* (2003), Liu *et al.* (2012), Li *et al.* (2013a, 2019), Yan *et al.* (2013), Zhao (2013), Tang *et al.* (2014, 2017a, b) and He *et al.* (2018).

high-Al amphibole-bearing adakitic rocks in the Nileke area were interpreted to be products of high pressure crystallization of melts derived from the partial melting of thickened continental lower crust (Tang *et al.*, 2017b). However, the late Carboniferous adakitic rocks in the Nileke area have much higher Nb/Ta and Dy/Yb ratios than the early Permian adakitic rocks (Li *et al.*, 2019), and these were interpreted as lower crustal thickening and consequent orogenic root delamination induced by eclogitization of thickened lower crust (Li *et al.*, 2019).

Sample description

The Heishantou pluton near Nileke County is located in the northern magmatic belt of the Yili Block. This belt is mainly composed of Permian and Upper Carboniferous volcanic-sedimentary strata and some intrusive rocks.

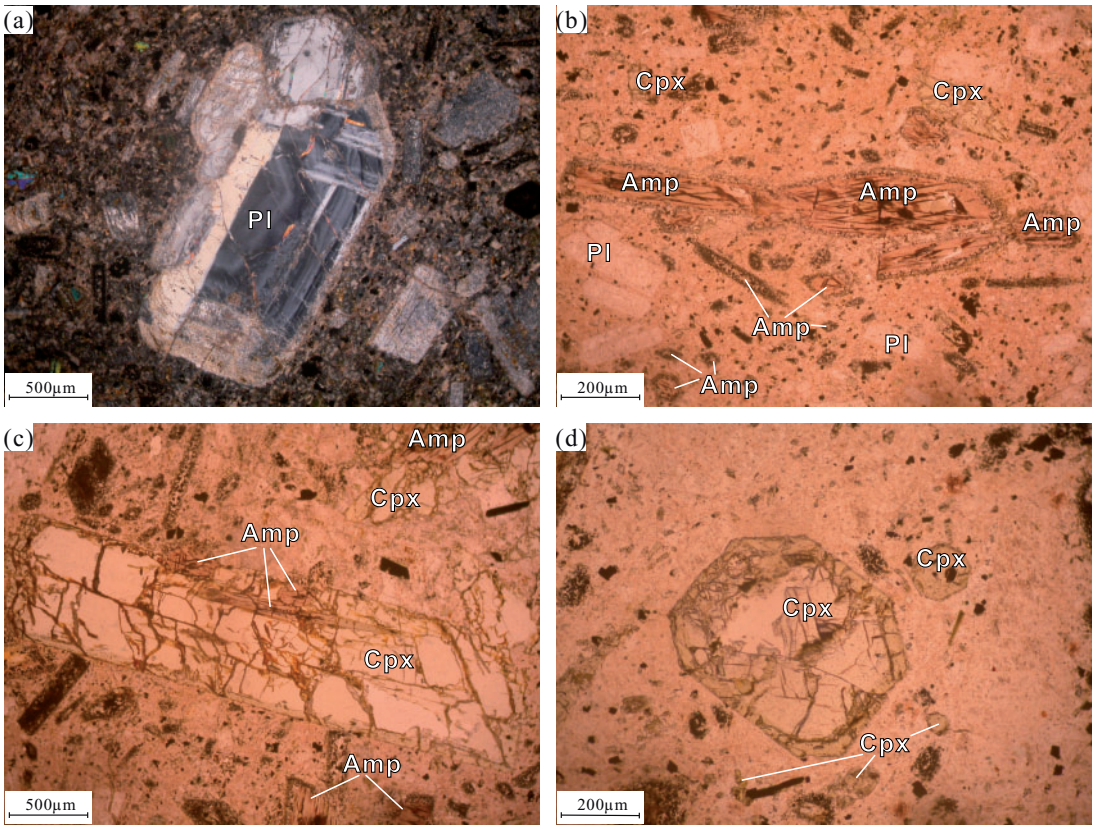

Fig. 2 Representative petrographic characteristics of Heishantou porphyric diorite: (a) the zoned plagioclase (Pl) phenocryst (cross-polarized light); (b) euhedral amphibole (Amp) phenocrysts; the rims were altered to fine-grained Fe–Ti oxides (plane-polarized light); (c, d) euhedral clinopyroxene (Cpx) phenocrysts with colorless core and greenish thin rim (plane-polarized light), showing prismatic (c) and octagonal cross-sections (d).

The Lower Permian volcano-sedimentary formation is termed the Wulang Formation, which consists of sandstone, basalt, basaltic andesite, shoshonite and rhyolite. The Wulang basalts and bimodal volcanic rocks were formed in a post-collisional setting (Ye *et al.*, 2013; Chen *et al.*, 2015; He *et al.*, 2018). The Middle Permian strata in the area contain the Xiaoshansayi, Hamisite and Tiemulike Formations from bottom to top (Fig. 1c). The Xiaoshansayi and Tiemulike Formations mainly consist of conglomerate, sandstone, siltstone and mudstone. The Hamisite Formation consists of clastic rocks, volcanic tuff and breccia, and shoshonitic basalt to rhyolite rocks, which were proposed to be derived from partial melting of thickened lithosphere of the Yili Block (Tang *et al.*, 2017b; He *et al.*, 2018). The Xiaoshansayi Formation unconformably overlies the Wulang Formation, and is overlain uncoformably by the Hamisite Formation (Fig. 1c). Early Permian intrusive rocks in Nileke area are mainly adakitic granodiorite porphyries, or A-type granites (Zhao *et al.*, 2008; Li *et al.*, 2013a, 2015a; Tang *et al.*, 2017a). The Heishantou pluton is dominantly composed of porphyritic diorite (Fig. 1c) and intruded into the Wulang Formation with hornfels surrounding the intrusions (Fig. 1c). Small crustal xenoliths are sparsely distributed in the diorite. The phenocrysts consist predominantly of plagioclase and clinopyroxene with minor amphibole (Fig. 2). Plagioclase phenocrysts are euhedral with variable grain sizes from ~100 μm to > 2 cm, and show complex compositional zoning (Fig. 2a). Clinopyroxene phenocrysts are subhedral and elongate with variable grain sizes from > 1 cm to < 100 μm that decrease gradually to the size of matrix clinopyroxene (Fig. 2c, d). They always show normal compositional zoning with a large colorless core and narrow greenish rim (Fig. 2c, d). Amphibole phenocrysts are subhedral with grain sizes from > 2 cm to ~100 μm, and partially altered with tiny Fe–Ti oxides surrounding the phenocrysts (Fig. 2b). Some amphibole phenocrysts are partially enclosed by clinopyroxene (Fig. 2c). The groundmass is mainly composed of K-feldspar, albite, clinopyroxene and Fe–Ti oxides, with minor apatite and sphene.

ANALYTICAL METHODS

In situ zircon U–Pb and oxygen isotopic analyses were performed using the Cameca IMS 1280HR ion microprobes at the State Key Laboratory of Isotope Geochemistry (SKLaBIG), Guangzhou Institute of Geochemistry, Chinese Academy of Sciences (GIGCAS). The measurements of the Qinghu zircon standards during the course of this study yield the weighted mean values of $^{206}Pb/^{238}U$ age = 161·4 ± 2·4 Ma ($n = 6$) and $\delta^{18}O$ = 5·32 ± 0·32‰ ($n = 9$; 95% confidence level),

which are respectively consistent with the recommended values of 159·5 ± 0·2 Ma and 5·4 ± 0·2‰ (Li *et al.*, 2013b) within errors. Whole-rock major elements were analysed using a Rigaku RIX 2000 X-ray fluorescence spectrometer, and analytical errors are less than 2%. After dissolved by acid, the samples were analysed using a Perkin-Elmer Sciex ELAN 6000 inductively coupled plasma mass spectrometry (ICP-MS) for whole-rock trace elements. Analytical precision is 1–5%. The detection limit and analytical error for Nb are 0·2 ppm and 2%, and those for Ta are 0·05 ppm and 4%, respectively. Whole-rock Sr–Nd–Hf isotopic ratios were measured via a Neptune Plus multi-collector ICP-MS (MC-ICP-MS). Reference standards analysed along with samples give $^{87}Sr/^{86}Sr = 0{\cdot}710252 \pm 0.000005$ (95% confidence level) for NBS987, $^{143}Nd/^{144}Nd = 0{\cdot}512096 \pm 0{\cdot}000002$ (95% confidence level) for Shin Etsu JNdi-1, and $^{176}Hf/^{177}Hf = 0{\cdot}282182 \pm 0{\cdot}000002$ (95% confidence level) for JMC14374. The analytical methods are principally similar to the description in our previous study (He *et al.*, 2016).

Back-scattered-electron (BSE) images of the minerals were captured using a Carl Zeiss SUPRA55SAPPHIRE Field Emission-Scanning Electron Microscope (SEM) at GIG-CAS. *In situ* major elemental analyses and X-ray maps of minerals were obtained using a Cameca SXFive FE Electron Probe Microanalyzer (EPMA) at GIG-CAS. This EPMA is equipped with an electron optical column with field emission source, controlled by Cameca PeakSight software. Five wavelength dispersive spectrometers (WDS) with 14 crystals are installed, including three LLIF, one LIF, two LPET, two PET, one LTAP, one TAP and four PCs (W–Si layered-dispersion elements, also known as pseudo-crystals). Rowland circle radius of the WDS spectrometer is 160 mm, which is large enough to extremely diffract some overlapping elemental peaks. For example, there is no overlap between Sr $K\alpha$ and Si $K\beta$, which will happen when using a smaller Rowland circle. The PC crystals (PC0, PC1, PC2, and PC3) are characterized by offering greater count rates, decreased spectral resolution (reducing peak shape and shift effects) and multiple-order X-ray suppression, and thus are specified to measure the light elements from Be to Na. In this study, we used the PC1 to measure F. A verification routine was operated every day by moving the spectrometers to the theoretical position of a well-defined line, for calibrating the WDS spectrometers from drift caused by temperature-related changes in diffraction crystal *d*-spacing. An operating condition of 15 kV accelerating voltage and 20 nA beam current was used during the course of this study. A variable peak counting time (8–180 s) was designed based on the intensity of characteristic X-ray line and desired precision for the element. Calibration standards used for feldspar analysis were albite (Na), almandine (Mg), sanidine (Si, K), hematite (Fe), plagioclase (Ca), barite (Ba) and Celestite (Sr). Calibration standards for amphibole and pyroxene analyses were jadeite (Na, Al), diopside (Si, Mg, Ca), orthoclase (K), rutile (Ti), Cr_2O_3 (Cr), hematite (Fe), rhodonite (Mn), nickel silicide (Ni), topaz (F) and tugtupite (Cl) from SPI company. The PAP (Pouchou and Pichoir) procedure was used for matrix correction (Pouchou & Pichoir, 1991). The standards were measured as unknown specimen using the same calibration to test accuracy of each elemental calibration by confirming the $I_x/I_{std} = 1$ (I_x and I_{std} are the intensities of the unknown specimen and the standard, respectively). In addition, SPI standards diopside and plagioclase were used as external standards to monitor the instrumental drift, and to show high reproducibility and accuracy (within error) as compared to the references (Supplementary Data Fig. S1; supplementary data are available for downloading at http://www.petrology.oxfordjournals.org). Major elemental X-ray mapping of clinopyroxene phenocrysts was conducted at 15 kV and 200 nA with focused beam, 2 μm pixel size and 200 ms dwell time per pixel.

In situ trace elemental analyses were conducted by LA-ICP-MS at the State Key Laboratory of Geological Processes and Mineral Resources, China University of Geosciences, Wuhan. This ICP-MS instrument is equipped with a GeoLas 2005 laser sampler and an Agilent 7500a system to acquire ion-signal intensities. Detailed operating conditions for the ICP-MS instrument, the laser ablation system and data reduction are the same as the description in Liu *et al.* (2008). A spot size of 40 μm and repetition rate of 6 Hz were applied during the analysis, and each analysis incorporated a background acquisition of approximately 20 −30 s (gas blank) followed by 50 s of data acquisition from the sample. Elemental contents were calibrated against multiple reference materials (BCR-2G, BIR-1G and BHVO-2G) without applying internal standardization (Liu *et al.*, 2008). External standard of National Institute of Standards and Technology SRM 610 was analysed after every nine sample spots. Analytical precision and accuracy for major elements and most trace elements are better than 5%.

In situ Sr isotope analysis for plagioclase was performed by LA-MC-ICP-MS at GIG-CAS, using a Neptune Plus MC-ICP-MS system coupled with a Resolution M50 193 nm ArF-excimer laser sampler. The analytical procedure and data processing was described by Zhang *et al.* (2015) in detail. Spot diameter of 82 μm, repetition rate of 7 Hz and ablation time of 29 s were applied. The United States Geological Survey (USGS) glass NKT-1G and plagioclase standard MkAn were used as external standards. Repeated analyses of NKT-1G and MkAn gave $^{87}Sr/^{86}Sr = 0{\cdot}70352 \pm 0{\cdot}00008$ (2σ; reference value $0{\cdot}70351 \pm 0{\cdot}00002$ by Elburg *et al.*, 2005) and $0{\cdot}70348 \pm 0{\cdot}00008$ (2σ; reference value $0{\cdot}70343 \pm 0{\cdot}00006$ by Kimura *et al.*, 2013).

RESULTS

In situ zircon U–Pb geochronology and O isotopes

Sample HST114 was selected for zircon U–Pb age and O isotope analyses. Zircons from sample HST114 are all

Table 1: SIMS zircon U–Pb analytical data for sample HST114 of the Heishantou diorite

Spots	U (ppm)	Th (ppm)	Th/U	$^{206}Pb/^{204}Pb$ measured	f_{206} (%)	$^{207}Pb/^{206}Pb$ ($\pm1\sigma$)	$^{207}Pb/^{235}U$ ($\pm1\sigma$)	$^{206}Pb/^{238}U$ ($\pm1\sigma$)	$^{207}Pb/^{206}Pb$ age (Ma, $\pm1\sigma$)	$^{207}Pb/^{235}U$ age (Ma, $\pm1\sigma$)	$^{206}Pb/^{238}U$ age (Ma, $\pm1\sigma$)	Conc.(%)	$\delta^{18}O$	$\pm1\sigma$
1	209	121	0·58	11218	0·17	0·0511 ± 5	0·3036 ± 63	0·0431 ± 8	246 ± 24	269 ± 5	272 ± 5	99	5·74	0·09
2	117	58	0·49	4748	0·39	0·0498 ± 8	0·2933 ± 73	0·0427 ± 8	184 ± 38	261 ± 6	270 ± 5	97	5·60	0·10
3	181	150	0·83	6714	0·28	0·0512 ± 7	0·3065 ± 72	0·0435 ± 8	248 ± 30	271 ± 6	274 ± 5	99	5·52	0·09
4	138	72	0·52	4634	0·40	0·0506 ± 10	0·2974 ± 80	0·0426 ± 8	222 ± 45	264 ± 6	269 ± 5	98	6·94	0·11
5	147	95	0·64	6837	0·27	0·0510 ± 8	0·3009 ± 74	0·0428 ± 8	239 ± 38	267 ± 6	270 ± 5	99	6·05	0·09
6	168	84	0·50	10462	0·18	0·0522 ± 7	0·3417 ± 79	0·0475 ± 9	295 ± 31	298 ± 6	299 ± 5	100	5·39	0·08
7	304	236	0·78	11117	0·17	0·0513 ± 5	0·3068 ± 63	0·0434 ± 8	253 ± 22	272 ± 5	274 ± 5	99	5·78	0·07
8	257	139	0·54	5638	0·33	0·0498 ± 6	0·2931 ± 64	0·0427 ± 8	187 ± 26	261 ± 5	269 ± 5	97	6·32	0·12
9	249	178	0·71	7979	0·23	0·0517 ± 5	0·3076 ± 65	0·0431 ± 8	272 ± 24	272 ± 5	272 ± 5	100	6·10	0·09
10	218	206	0·94	6193	0·30	0·0512 ± 9	0·3035 ± 77	0·0430 ± 8	248 ± 41	269 ± 6	272 ± 5	99	5·96	0·09
11	143	92	0·64	5979	0·31	0·0516 ± 10	0·3013 ± 81	0·0424 ± 8	267 ± 45	267 ± 6	267 ± 5	100	6·42	0·12
12	119	68	0·57	6603	0·28	0·0503 ± 10	0·2978 ± 78	0·0429 ± 8	211 ± 44	265 ± 6	271 ± 5	98	6·11	0·08
13	97	44	0·45	4774	0·39	0·0511 ± 10	0·3041 ± 82	0·0431 ± 8	246 ± 46	270 ± 6	272 ± 5	99	6·01	0·08
14	236	132	0·56	11053	0·17	0·0514 ± 6	0·3080 ± 67	0·0434 ± 8	260 ± 27	273 ± 5	274 ± 5	99	5·98	0·10
15	89	35	0·39	3092	0·60	0·0501 ± 20	0·3004 ± 130	0·0435 ± 8	201 ± 89	267 ± 10	274 ± 5	97	7·48	0·11
16	243	237	0·98	5253	0·36	0·0528 ± 9	0·3127 ± 77	0·0430 ± 8	320 ± 37	276 ± 6	271 ± 5	102	6·27	0·09
17	153	84	0·55	1732	1·08	0·0533 ± 37	0·3280 ± 233	0·0447 ± 8	340 ± 148	288 ± 18	282 ± 5	102	6·66	0·08
18	101	42	0·42	2804	0·67	0·0519 ± 14	0·3047 ± 101	0·0426 ± 8	280 ± 63	270 ± 8	269 ± 5	100	7·36	0·10

f_{206}: percentage of common ^{206}Pb in total measured ^{206}Pb.

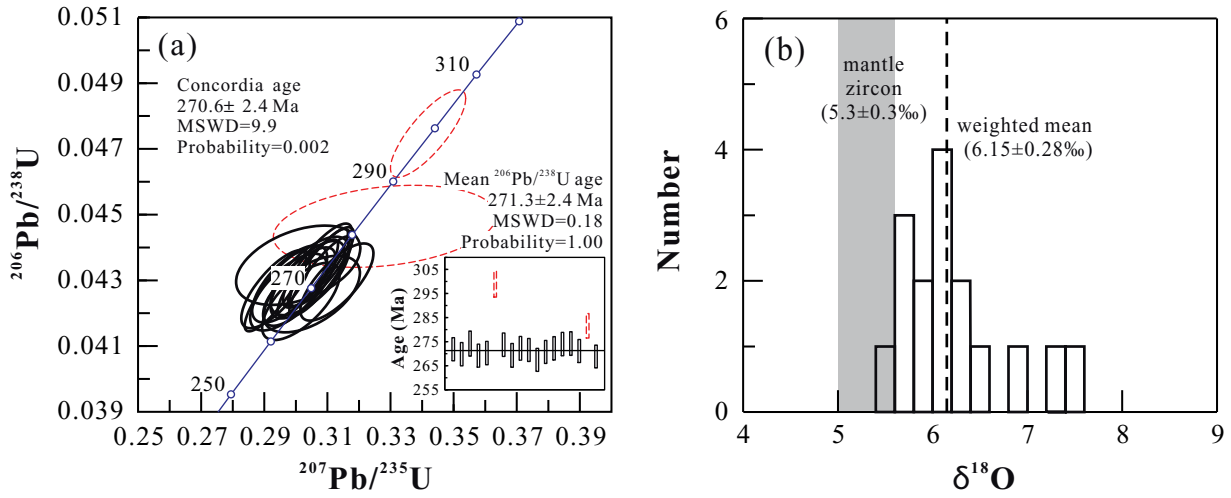

Fig. 3 (a) Concordia diagram for SIMS zircon U–Pb analyses of the Heishantou diorite (Sample HST114); inset shows $^{206}Pb/^{238}U$ ages and the weighted mean value; (b) histogram of *in situ* zircon $\delta^{18}O$ values for the Heishantou diorite; $\delta^{18}O$ values of mantle zircons are from Valley *et al.* (1998).

transparent euhedral prismatic grains that show well-developed concentric oscillatory zoning, indicating a magmatic origin. Eighteen analysed zircons have moderate U and Th content (89 −304 ppm and 35 − 237 ppm, respectively) with high Th/U ratios (0·39 − 0·98) (Table 1). Spot 6 has an old $^{206}Pb/^{238}U$ age (299 ± 5 Ma) that is interpreted as the age of inherited zircon. Spot 17 has a slightly old $^{206}Pb/^{238}U$ age (282 ± 5 Ma) due to its very low $^{206}Pb/^{204}Pb$ ratio that is inappropriate for the common Pb correction. The other sixteen analyses form a tight group and have concordant U–Pb ages (Table 1; Fig. 3a), yielding a weighted mean $^{206}Pb/^{238}U$ age of 271 ± 2 Ma (MSWD = 0·18), which is interpreted as the crystallization age. This is identical to the previous dating results for other adakites in the Nileke area (268 ± 5 Ma by $^{40}Ar/^{39}Ar$ dating method, Zhao *et al.*, 2003, and 272 ± 3 Ma by LA-ICP-MS zircon U–Pb dating method, Tang *et al.*, 2017b) within errors.

Zircons from sample HST114 have variable $\delta^{18}O$ values (5·52 −7·48‰), yielding a weighted mean value of 6·15 ± 0·28‰ (95% confidence level; Table 1; Fig. 3b), which is slightly higher than the values of mantle-derived zircons (5·3 ± 0·3‰; Valley *et al.*, 1998).

Whole-rock geochemistry

Samples of the Heishantou porphyric diorite contain moderate SiO_2 (55·1–66·6 wt %) and K_2O (1·7–2·8 wt %), which are more basic than other Permian adakites in the Tianshan Orogen (Fig. 4a and b). They have high Al_2O_3 (15·8–17·5 wt %) and Na_2O (3·8–7·3 wt %), and show low K_2O/Na_2O (0·2–0·6) and moderate $Mg^{\#}$ (31–53) (Table 2; Fig. 4). Their low Ni (7·5–35 ppm) and Cr (6·0–22 ppm) are comparable to those of other Permian adakitic rocks (Zhao *et al.*, 2008; Huang *et al.*, 2012; Tang *et al.*, 2017b; Li *et al.*, 2019) in the Western Tianshan (Fig. 4c and d).

The samples show highly fractionated chondrite-normalized REE patterns with insignificant Eu anomalies ($_{\delta}Eu$ = 0·83–1·01; Fig. 5a). They have high Sr (453–1875 ppm) and light rare earth elements (LREE) but low Y (5·1–8·6 ppm) and Yb (0·39–0·73 ppm) with high Sr/Y (73–220) and $[La/Yb]_N$ (21–41), which resemble the values of typical adakites (Defant & Drummond, 1990; Martin, 1999; Martin *et al.*, 2005) (Fig. 4e and f). Overall, adakites in the Nileke area show much higher Sr/Y and $[La/Yb]_N$ than most of other Paleozoic adakitic rocks in the Tianshan Orogen (Fig. 4e and f). On the primitive mantle-normalized multi-element variation diagrams, the samples of the Heishantou porphyric diorite are also characterized by pronounced negative Nb, Ta and Ti anomalies and a positive Sr anomaly (Fig. 5b).

Whole-rock Sr–Nd–Hf isotopes

Samples of Heishantou porphyric diorite exhibit narrow ranges of $^{87}Sr/^{86}Sr$, $^{143}Nd/^{144}Nd$ and $^{176}Hf/^{177}Hf$ ratios (Table 3; Fig. 6), characterized by low initial $^{87}Sr/^{86}Sr$ (0·7049–0·7053) and positive $\varepsilon_{Nd}(t)$ (+1·3 to +2·8) and $\varepsilon_{Hf}(t)$ (+7·2 to +8·7). The studied samples have distinct isotopic values from mid-ocean ridge basalt (MORB) but show affinity to the Carboniferous mafic and felsic rocks in the Western Tianshan (Fig. 6a; Chen *et al.*, 2001; Xia *et al.*, 2004, 2008; Zhu et al., 2006a, b; Wang *et al.*, 2006b, 2007b; Qian *et al.*, 2006; Ma *et al.*, 2008; Tang *et al.*, 2012, 2014; Yang *et al.*, 2012; Lin et al., 2015; Li *et al.*, 2015b; Ge *et al.*, 2015; He *et al.*, 2016; Xie *et al.*, 2016a). Bulk-rock Sr–Nd isotopic compositions of the studied samples are similar to those of other adakitic rocks in the Nileke area (Zhao *et al.*, 2008; Tang *et al.*, 2017b; Li *et al.*, 2019), which are comparable to the Early Permian felsic intrusive rocks but different from the basaltic volcanic rocks in the same area (Fig. 6a). In addition, their bulk-rock Nd–Hf isotopic compositions plot slightly above but parallel to the terrestrial array (Fig. 6b; Vervoort *et al.*, 2000). They lie between the Tianshan Carboniferous mafic rocks (320–300 Ma; He

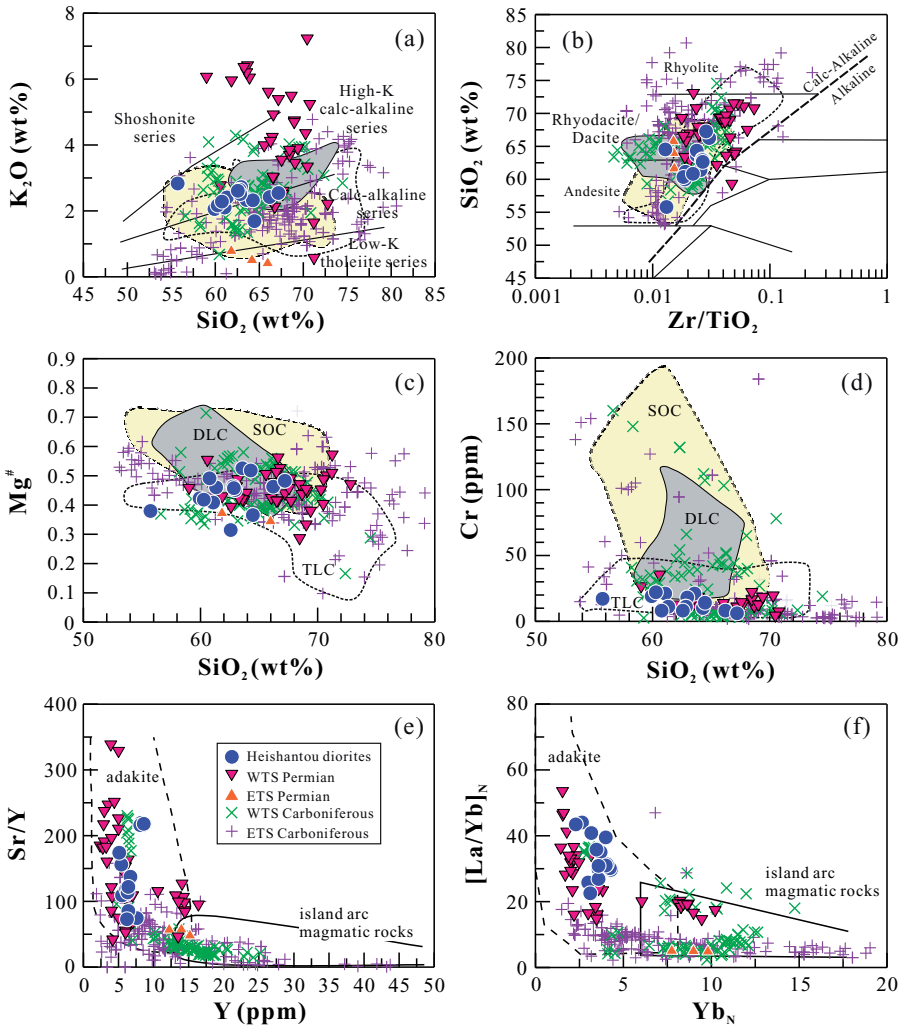

Fig. 4 (a) K_2O vs SiO_2 (the subdivision of subalkalic rocks is after Peccerillo & Taylor, 1976); (b) SiO_2 vs Zr/TiO_2 (the subdivision of rock types is after Winchester & Floyd, 1977); (c) $Mg^{\#}$ vs SiO_2; (d) Cr vs SiO_2; (e) Sr/Y vs Y; and (f) $[La/Yb]_N$ vs Yb_N for the Heishantou diorite. Fields of adakites from delaminated lower crust (DLC, grey field), subducted oceanic crust (SOC, yellow field) and thickened lower crust (TLC, dashed field) are after the compilation of Wang *et al.* (2006a). Fields of adakites and island arc magmatic rocks are from Defant & Drummond (1990) and Martin *et al.* (2005). Carboniferous and Permian adakitic rocks in the Tianshan area (WTS, Western Tianshan; ETS, Eastern Tianshan) are from Xiong *et al.* (2005b), Han *et al.* (2006), Wang *et al.* (2006b, 2007b, 2015, 2016, 2018), Zhang *et al.* (2006), Zhao *et al.* (2008), Su *et al.* (2009), Huang *et al.* (2012), Xie *et al.* (2013), Xu *et al.* (2013), Liu *et al.* (2016), Yin *et al.* (2016, 2017), Tang *et al.* (2017b), Xiao *et al.* (2017), Du *et al.* (2019), Li *et al.* (2019) and Long *et al.* (2020). Oxides were recalculated volatile-free.

et al., 2016; Xie *et al.*, 2016a, b) and Tarim mafic rocks at ~290 Ma (Yu *et al.*, 2011).

In situ mineral compositions and plagioclase Sr isotopes

Plagioclase Euhedral plagioclase phenocrysts in the Heishantou porphyric diorite have variable An content (24–63 mol %; Supplementary Data Table S1; supplementary data are available for downloading at http://www.petrology.oxfordjournals.org) but are mostly andesine. They have variable SrO (0·14–0·67 wt %) that overall are higher than those in adakites (Solander and Little Solander Islands; Foley *et al.*, 2013) and arc lavas (Tonga, Ryukyu, Kermadec, Kamchatka, Izu–Bonin, Honshu, Andean, Aleutian, Aeolian, Aegean, and Central American volcanic arc, compiled from GEOROC database; Fig. 7a). *In situ* plagioclase $^{87}Sr/^{86}Sr$ ratios vary within a narrow range of 0·70444–0·70505 (Table 4; Fig. 7b and c). Because the intensity of ^{88}Sr in plagioclase (3·66 – 8·74 V) is much higher than that of ^{85}Rb (< 0·02 V except for one measurement of 0·10 V), measured $^{87}Sr/^{86}Sr$ ratios can represent initial $^{87}Sr/^{86}Sr$ ratios of the analysed plagioclase (Table 4). The plagioclase $^{87}Sr/^{86}Sr$ ratios have a negative correlation with An content but a positive correlation with SrO content except for some analyses that have low $^{87}Sr/^{86}Sr$ but high SrO or low An content (Fig. 7b and c).

Plagioclase phenocrysts show complex compositional zoning (Fig. 8), with periodic variation of An content that increases abruptly and then overall gradually decreases from core to rim (Fig. 8). There are two parts within the crystal according to *in situ* $^{87}Sr/^{86}Sr$ values,

Table 2: Whole-rock major (wt %) and trace (ppm) elements of the Heishantou diorite

Sample	HST01	HST02	HST04	HST05	HST06	HST109	HST110	HST112	HST113	HST114	HST115	HST116	HST118	HST120	HST121
SiO_2	59·55	60·81	59·85	65·71	66·63	63·09	63·72	62·43	62·31	60·90	62·34	60·21	62·13	55·10	63·88
TiO_2	0·52	0·53	0·54	0·40	0·38	0·39	0·41	0·41	0·41	0·42	0·40	0·46	0·41	0·66	0·60
Al_2O_3	17·26	17·50	17·37	15·82	15·89	16·34	16·34	16·20	16·10	15·93	16·38	16·82	16·66	17·20	15·96
$Fe_2O_3^t$	5·09	4·77	5·16	3·32	3·04	4·01	4·17	4·39	4·39	4·42	4·42	4·50	3·72	5·35	4·75
MnO	0·06	0·06	0·05	0·06	0·04	0·06	0·04	0·06	0·06	0·06	0·05	0·05	0·05	0·11	0·05
MgO	1·88	1·66	1·87	1·44	1·43	2·24	2·26	1·82	1·91	1·90	1·88	2·19	0·86	1·65	1·38
CaO	6·57	5·77	5·82	3·71	3·25	3·09	2·25	2·58	2·69	3·74	2·50	3·01	3·38	6·43	2·06
Na_2O	4·61	4·92	4·83	3·78	4·14	4·27	4·31	4·76	4·79	4·47	4·47	4·47	4·96	5·94	7·26
K_2O	2·03	2·08	2·14	2·39	2·51	2·30	2·29	2·69	2·61	2·38	2·48	2·25	2·58	2·79	1·66
P_2O_5	0·34	0·34	0·33	0·18	0·16	0·17	0·15	0·23	0·23	0·27	0·21	0·26	0·26	0·33	0·23
LOI	1·45	1·10	1·31	2·42	1·65	3·25	3·15	3·57	3·71	4·78	4·04	4·84	4·25	3·30	1·23
Total	99·36	99·54	99·27	99·23	99·12	99·21	99·09	99·14	99·21	99·27	99·17	99·06	99·26	98·86	99·06
$Mg^{\#}$	42·3	40·8	41·8	46·2	48·2	52·5	51·8	45·1	46·3	46·0	45·7	49·1	31·4	37·9	36·5
Sc	9·2	8·9	8·7	4·5	4·6	6·6	6·9	6·4	7·0	7·4	6·6	7·1	6·6	10·4	10·3
V	131	143	131	62	56	79	86	83	85	86	85	93	80	148	131
Cr	19	21	22	8	6	21	10	18	11	11	11	8	8	17	14
Co	49·5	64·6	47·9	34·1	73·9	39·0	43·2	32·3	36·7	33·4	34·3	39·9	40·6	38·1	73·2
Ni	32·5	30·2	35·0	8·7	7·5	10·9	12·5	10·8	11·7	11·6	11·5	13·1	13·1	23·5	19·4
Cu	105	23·1	32·4	44·9	29·3	15·5	25·7	2·3	5·0	3·4	2·6	1·2	5·1	15·3	26·2
Zn	46	37	148	57	51	80	81	63	52	45	49	48	44	44	46
Ga	20·4	20·0	20·7	19·4	18·6	18·7	19·9	19·0	19·7	19·2	19·4	20·1	19·4	17·5	13·1
Ge	0·08	0·08	0·07	0·06	0·07	0·07	0·06	0·09	0·12	0·13	0·10	0·08	0·09	0·10	0·10
Rb	29·3	29·6	34·9	35·5	35·3	35·9	38·5	57·9	64·4	50·3	52·1	57·0	54·5	53·9	25·2
Sr	1800	1815	1750	843	888	665	601	727	717	568	548	453	782	1875	922
Y	8·2	8·4	8·1	5·4	5·1	6·0	5·5	6·1	6·3	7·6	6·4	6·2	6·4	8·6	6·7
Zr	99	102	100	123	110	94	99	110	110	109	108	103	111	88	78
Nb	3·5	3·5	3·4	4·1	3·7	2·9	3·2	3·8	3·9	4·0	3·9	4·4	3·8	2·6	2·4
Cs	2·93	3·31	3·48	2·74	1·67	5·29	7·39	11·4	15·2	7·27	6·17	11·5	7·60	5·27	2·23
Ba	733	775	736	738	804	525	780	637	534	448	451	491	746	2510	1000
La	30·1	30·2	30·1	27·6	23·6	18·3	16·6	25·3	30·7	29·3	22·8	29·4	26·2	37·4	30·7
Ce	67·1	66·0	66·0	55·8	48·7	37·4	34·7	55·3	64·5	65·2	50·4	63·4	57·9	78·7	68·7
Pr	8·30	8·25	8·04	6·39	5·42	4·46	3·99	6·66	7·75	7·99	6·01	7·53	6·69	9·73	8·71
Nd	32·9	32·7	32·0	22·6	19·7	17·2	15·1	24·5	28·2	30·2	23·2	28·9	25·2	38·7	34·8
Sm	4·86	4·91	4·33	3·38	2·89	2·62	2·65	3·69	3·59	4·18	2·98	3·87	3·73	6·03	5·74
Eu	1·18	1·27	1·22	0·75	0·72	0·75	0·61	0·80	0·98	0·98	0·72	0·93	0·87	1·50	1·29
Gd	2·74	2·82	2·77	1·81	1·62	1·90	1·44	1·91	2·15	2·60	1·71	2·21	2·02	3·28	2·79
Tb	0·36	0·38	0·34	0·22	0·22	0·25	0·18	0·24	0·22	0·32	0·25	0·26	0·24	0·35	0·30
Dy	1·67	1·69	1·66	1·04	0·96	1·12	1·01	1·16	1·19	1·64	1·26	1·31	1·35	1·66	1·69
Ho	0·33	0·32	0·32	0·19	0·17	0·22	0·22	0·22	0·25	0·31	0·23	0·25	0·26	0·32	0·30
Er	0·84	0·84	0·79	0·49	0·44	0·56	0·61	0·66	0·65	0·81	0·64	0·64	0·69	0·78	0·76
Tm	0·12	0·12	0·11	0·07	0·06	0·08	0·09	0·10	0·09	0·11	0·09	0·09	0·10	0·11	0·10
Yb	0·73	0·72	0·69	0·45	0·39	0·51	0·53	0·61	0·54	0·68	0·61	0·59	0·61	0·68	0·63
Lu	0·11	0·10	0·11	0·08	0·06	0·09	0·08	0·09	0·08	0·10	0·09	0·09	0·09	0·09	0·09
Hf	2·4	2·5	2·4	2·8	2·7	2·5	2·5	2·7	2·6	2·6	2·6	2·5	2·8	2·3	2·1

(continued)

Table 2:. Continued

Sample	HST01	HST02	HST04	HST05	HST06	HST109	HST110	HST112	HST113	HST114	HST115	HST116	HST118	HST120	HST121
Ta	0·15	0·15	0·20	0·23	0·18	0·15	0·16	0·16	0·18	0·18	0·18	0·17	0·22	0·20	0·20
Pb	9·2	7·9	8·5	10·9	10·2	12·1	9·5	3·1	2·3	1·6	1·3	2·3	3·3	10·4	6·5
Th	2·49	2·42	2·54	3·76	3·13	2·46	2·50	2·98	3·03	3·00	2·95	2·86	3·18	4·83	4·72
U	0·81	0·82	0·81	1·13	0·90	0·83	0·82	0·94	0·98	0·86	0·93	0·74	0·93	1·24	0·99
δEu	0·90	0·96	1·01	0·84	0·93	0·98	0·87	0·83	1·00	0·85	0·90	0·89	0·88	0·94	0·87
Nb/La	0·12	0·12	0·11	0·15	0·16	0·16	0·19	0·15	0·13	0·14	0·17	0·15	0·15	0·07	0·08
Sr/Y	220	216	216	156	174	111	109	119	114	74·7	85·6	73·1	122	218	138
$[La/Yb]_N$	27·9	28·3	29·5	41·4	40·9	24·2	21·2	28·0	38·4	29·1	25·3	33·7	29·0	37·2	32·9
Yb_N	2·94	2·90	2·78	1·81	1·57	2·06	2·14	2·46	2·18	2·74	2·46	2·38	2·46	2·74	2·54

$Mg^{\#} = Mg/(Mg+Fe^{T})\times 100$.
$\delta Eu = 2\times Eu_N/(Sm_N+Gd_N)$; N, chondrite normalized.

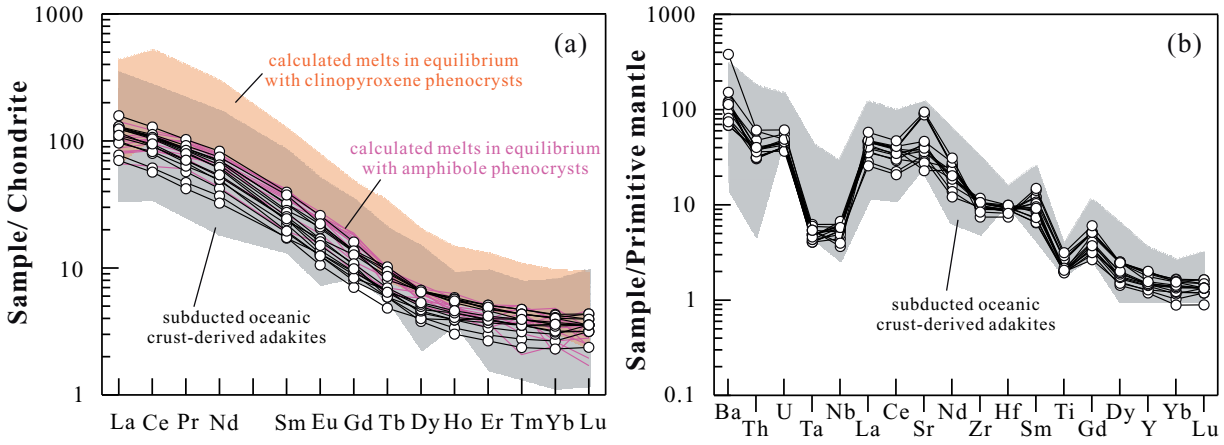

Fig. 5 (a) Chondrite-normalized REE patterns and (b) primitive mantle-normalized multielement diagrams of the Heishantou diorite. Normalization values of chondrite and primitive mantle are both from Sun & McDonough (1989). Field of subducted oceanic crust-derived adakites are from Defant & Drummond (1990) and Martin *et al.* (2005). REE compositions of melt in equilibrium with clinopyroxene and amphibole phenocrysts in the Heishantou diorite were calculated using partition coefficients listed in Tables 5 and 6, respectively.

Table 3: Whole-rock Sr–Nd–Pb–Hf isotopes of the Heishantou diorite

Sample	HST109	HST110	HST112	HST114	HST116	HST120	HST121
$^{87}Rb/^{86}Sr$	0·1562	0·1853	0·2304	0·2562	0·3640	0·0832	0·0791
$^{87}Sr/^{86}Sr$	0·705493	0·705624	0·706131	0·706258	0·706609	0·705397	0·705438
2σ	0·000008	0·000009	0·000008	0·000009	0·000010	0·000011	0·000009
$(^{87}Sr/^{86}Sr)_i$	0·7049	0·7049	0·7052	0·7053	0·7052	0·7051	0·7051
$^{147}Sm/^{144}Nd$	0·0921	0·1061	0·0911	0·0837	0·0810	0·0942	0·0997
$^{143}Nd/^{144}Nd$	0·512598	0·512590	0·512517	0·512516	0·512506	0·512574	0·512566
2σ	0·000005	0·000006	0·000006	0·000004	0·000005	0·000007	0·000004
$(^{143}Nd/^{144}Nd)_i$	0·5124	0·5124	0·5124	0·5124	0·5124	0·5124	0·5124
$\varepsilon_{Nd}(t)$	2·8	2·2	1·3	1·5	1·4	2·3	1·9
$^{176}Lu/^{177}Hf$	0·0051	0·0045	0·0047	0·0055	0·0051		0·0061
$^{176}Hf/^{177}Hf$	0·282886	0·282884	0·282856	0·282846	0·282850		0·282882
2σ	0·000004	0·000004	0·000004	0·000008	0·000005		0·000006
$(^{176}Hf/^{177}Hf)_i$	0·2829	0·2829	0·2828	0·2828	0·2828		0·2829
$\varepsilon_{Hf}(t)$	8·7	8·7	7·7	7·2	7·4		8·4

$^{87}Rb/^{86}Sr$, $^{147}Sm/^{144}Nd$ and $^{176}Lu/^{177}Hf$ isotope ratios are calculated using whole-rock Rb, Sr, Sm, Nd, Lu and Hf contents.
The errors of $^{87}Sr/^{86}Sr$, $^{143}Nd/^{144}Nd$ and $^{176}Hf/^{177}Hf$ are all 2σ.
$\varepsilon_{Nd}(t) = [(^{143}Nd/^{144}Nd)_S/(^{143}Nd/^{144}Nd)_{CHUR}\text{-}1] \times 10000$; $(^{143}Nd/^{144}Nd)_{CHUR} = 0{\cdot}512638$; $(^{147}Sm/^{144}Nd)_{CHUR} = 0{\cdot}1967$; $\varepsilon_{Hf}(t) = [(^{176}Hf/^{177}Hf)_S/(^{176}Hf/^{177}Hf)_{CHUR}\text{-}1] \times 10000$; $(^{176}Hf/^{177}Hf)_{CHUR}$=0·.282785; $(^{176}Lu/^{177}Hf)_{CHUR} = 0{\cdot}0336$; $t = 271$ Ma.

i.e. a low $^{87}Sr/^{86}Sr$ (0·7044–0·7047) core and a high $^{87}Sr/^{86}Sr$ (0·7047–0·7051) rim (Table 4; Fig. 8). For a plagioclase phenocryst, the core has lower SrO contents than the rim, and SrO contents in the core vary little with decreasing An content (Fig. 8). Abrupt increase of An content occurs in either the core or rim, and the boundary between the core and rim is resorbed (Fig. 8).

Clinopyroxene Clinopyroxenes in the Heishantou porphyric diorite are clustered in the pyroxene classification diagram and all plot within diopside field (Fig. 9a). The phenocrysts have colorless cores with greenish rims (Fig. 2c and d). The cores are mostly sector-zoned crystals consisting of prism and hourglass sectors, while the rims show concentric oscillatory compositional zonation (Fig. 10). Major elemental X-ray maps show clearly that prism sectors have lower Mg and higher Fe, Ti and Cr contents than hourglass sectors (Fig. 10), resembling the sector-zoned clinopyroxene described in Ubide *et al.* (2019). Overall, the cores including prism and hourglass sectors have higher $Mg^{\#}$ (78–84) and Cr_2O_3 (0·01–0·29 wt %) than the rims ($Mg^{\#}$ mostly 69–79, Cr_2O_3 mostly below detection limit to 0·02 wt %) (Fig. 10). However, the outermost parts of phenocryst rims compositionally overlap with the matrix clinopyroxenes (Supplementary Data Table S2; supplementary data are available for downloading at http://www.petrology.oxfordjournals.org; Fig. 9). The matrix clinopyroxenes have higher Al_2O_3 and lower MnO and Ti/Al than the cores of phenocrysts at comparable $Mg^{\#}$ values (Fig. 9).

Clinopyroxene phenocrysts have high Sr (149–228 ppm) and low Y (4–12 ppm) and Yb (0·3–0·9 ppm) with high Sr/Y ratios (15–41) and La/Yb ratios (4·8–10·4), compared to clinopyroxenes in the Aleutian primitive adakites and arc basalts (Yogodzinski & Kelemen, 1998) with corresponding $Mg^{\#}$ (Fig. 11a–d). Y and Yb concentrations in the zoned clinopyroxene phenocrysts increase with decreasing $Mg^{\#}$ from cores to rims and Sr

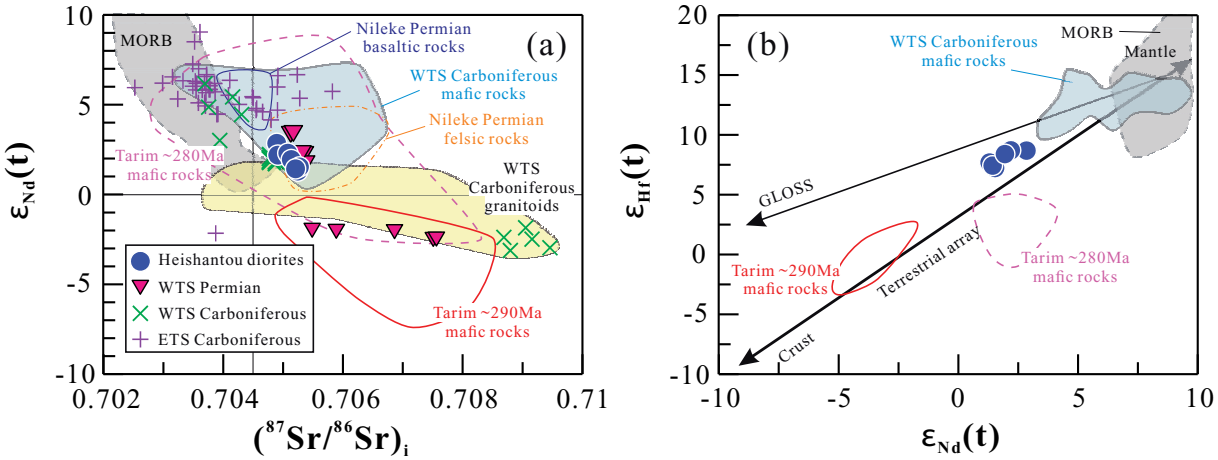

Fig. 6 (a) $\varepsilon_{Nd}(t)$ vs $(^{87}Sr/^{86}Sr)_i$; and (b) $\varepsilon_{Hf}(t)$ vs $\varepsilon_{Nd}(t)$ for the Heishantou diorite. The initial Sr–Nd–Hf isotopes were all calculated at 271 Ma. Nd–Hf GLOSS (global subducted sediments)-mantle array and terrestrial array are from Chauvel *et al.* (2008) and Vervoort *et al.* (2000), respectively. Sr–Nd isotopic data sources: Permian adakitic rocks in the Western Tianshan (WTS) (Zhao *et al.*, 2008; Huang *et al.*, 2012), Carboniferous adakitic rocks in the Western Tianshan (Wang *et al.*, 2007b; Xie *et al.*, 2013; Li *et al.*, 2019), Carboniferous adakitic rocks in the Eastern Tianshan (ETS) (Zhang *et al.*, 2006; Liu *et al.*, 2016; Wang *et al.*, 2016, 2018; Du *et al.*, 2019), Permian basaltic volcanic rocks in the Nileke area (Ye *et al.*, 2013), Permian felsic intrusive rocks in the Nileke area (Li *et al.*, 2013a, 2015a; Luo *et al.*, 2013; Yan *et al.*, 2013; Ding *et al.*, 2014; Chen *et al.*, 2015), Carboniferous mafic and felsic magmatic rocks in the Western Tianshan (Chen *et al.*, 2001; Xia *et al.*, 2004, 2008; Zhu et al., 2006a, b; Wang *et al.*, 2006b, 2007b; Qian *et al.*, 2006; Ma *et al.*, 2008; Tang *et al.*, 2012, 2014; Yang *et al.*, 2012; Lin et al., 2015; Li *et al.*, 2015b; Ge *et al.*, 2015; He *et al.*, 2016; Xie *et al.*, 2016a). Nd–Hf isotopic data source: Carboniferous mafic rocks in Western Tianshan (He *et al.*, 2016; Xie *et al.*, 2016a, b). Fields of the Tarim Permian mafic rocks are after the compilation of He *et al.* (2016). MORB data are based on Stracke *et al.* (2005).

concentrations greatly overlap (Fig. 11a–c), resulting in overall decreasing Sr/Y ratios from cores to rims. The rims of zoned Cpx phenocrysts have much lower Cr (< 6 ppm), Ni (< 87 ppm) concentrations and Dy/Yb ratios (2·8–3·3) than the cores (Table 5; Fig. 11e–g). The chondrite-normalized REE patterns are parallel and convex-upward for all clinopyroxene phenocrysts, and the rims show slightly negative Eu anomalies (Fig. 11h, Fig. 12). All clinopyroxene phenocrysts exhibit negative Nb, Zr, Hf and Ti anomalies on the primitive mantle-normalized multi-element variation diagrams (Fig. 12).The hourglass sectors in the sector-zoned cores also have higher REE and high field strength elements (HFSE) than the prism sectors, which is similar to the descriptions in Ubide *et al.* (2019).

Amphibole Amphibole phenocrysts in the Heishantou porphyric diorite have narrow ranges of FeO (8·2–9·8 wt %), MgO (14·7–16·1 wt %), CaO (11·6–12·0 wt %) and Na_2O (2·6–3·1 wt %), moderate TiO_2 (1·6–2·2 wt %), Cr_2O_3 (0·03–0·36 wt %), high F (2·1–3·2 wt %), and low Cl (< 0·02 wt %) (Table 6), and they belong to (fluor-)magnesiohastingsite. The Heishantou amphiboles show parallel and convex-upward REE patterns with high La/Yb ratios (6–14) and exhibit positive Sr and negative Nb, Zr and Hf anomalies on the trace elements patterns (Fig. 13). In addition, the Heishantou amphiboles exhibit higher Sr/Y ratios (53–127) and lower Y contents (6·1–9·6 ppm) than those in adakites (Solander and Little Solander Islands; Foley *et al.*, 2013) and arc lavas (Ewart & Taylor 1969; Samaniego *et al.*, 2010; Chiaradia *et al.*, 2011; Tiepolo *et al.*, 2012; Johnson *et al.*, 2013) (Fig. 14a). They also have much higher fluorine (0·9–3·2 wt %) than the amphiboles from arc-related adakites (Rodriguez *et al.*, 2007; Rooney *et al.*, 2011) (F < 1 wt %; Fig. 14b).

DISCUSSION

Petrogenesis of Heishantou adakitic diorite

The studied samples of the Heishantou diorite show various degrees of alteration (Fig. 2), and some samples have relatively high loss on ignition (LOI) (Table 2). Consequently, some large ion lithophile elements (LILE), such as Rb, Sr and Ba, might have been mobilized during alteration, whereas REE and HFSE are generally immobile during alteration (Pearce, 2014). Some samples have lower Sr contents than the others, which would be due to alteration because their Sr contents and Sr/Y ratios all decrease with increasing LOI (Supplementary Data Fig. S2; supplementary data are available for downloading at http://www.petrology.oxfordjournals.org). However, some less altered samples (LOI < 2 wt %) have the highest Sr (> 1600 ppm) and Sr/Y (> 200), indicating primary high Sr and Sr/Y of the rocks. In addition, both Nb/Zr and La/Yb of the studied samples are uncorrelated with LOI (Supplementary Data Fig. S2; supplementary data are available for downloading at http://www.petrology.oxfordjournals.org), and all samples show parallel REE and HFSE patterns (Fig. 5a, b), suggesting that these incompatible trace elements might be immobile and have preserved the original chemical characteristics despite the alteration.

Regarding the adakite definition originally given by Defant & Drummond (1990) and later summarized by

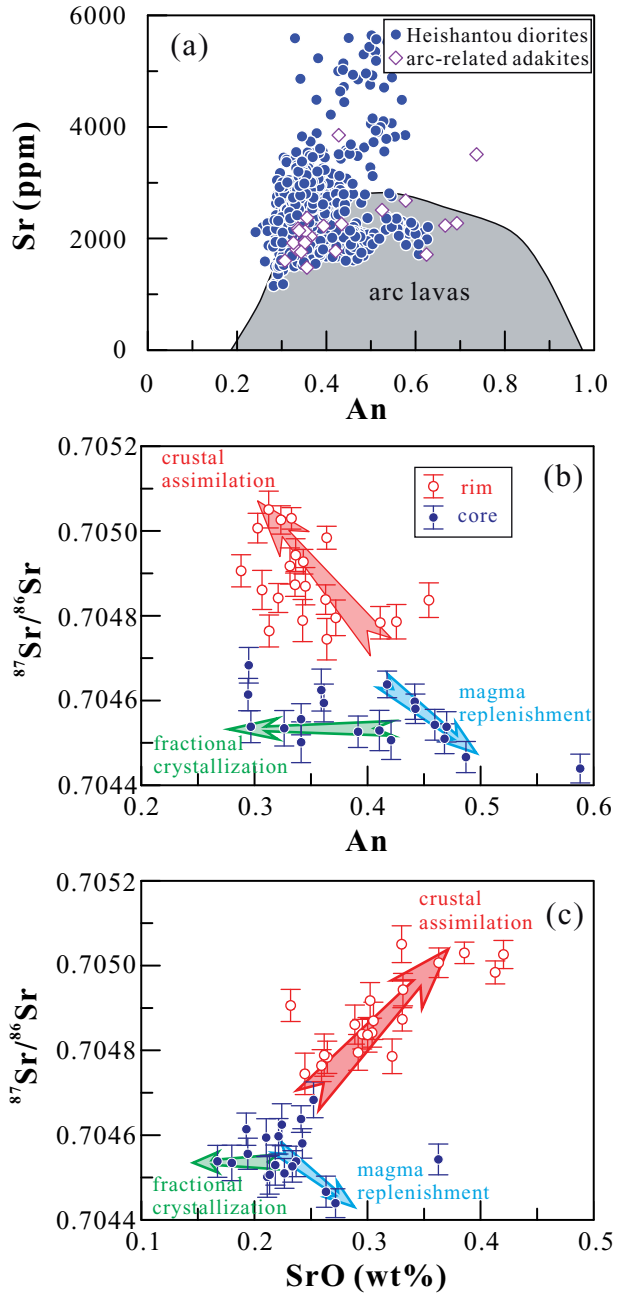

Fig. 7 (a) Sr vs An; (b) $^{87}Sr/^{86}Sr$ vs An; and (c) $^{87}Sr/^{86}Sr$ vs SrO for the plagioclase phenocrysts in the Heishangtou diorite. The plagioclases in arc-related adakites are from Solander and Little Solander Islands (New Zealand) (Foley *et al.*, 2013). The plagioclases in arc lavas are from Tonga, Ryukyu, Kermadec, Kamchatka, Izu-Bonin, Honshu, Andean, Aleutian, Aeolian, Aegean and Central American volcanic arc, which are compiled from GEOROC database (http://georoc.mpch-mainz.gwdg.de/georoc/).

Martin *et al.* (2005) and Moyen (2009), the Heishantou diorite samples display typical adakitic compositional features ($SiO_2 > 56\%$, $Al_2O_3 > 15\%$, $MgO < 3\%$, $Na_2O > 3{\cdot}5\%$, $Sr > 400$ ppm, $Y < 18$ ppm, $Yb < 1{\cdot}9$ ppm, and $Sr/Y > 40$ and $[La/Yb]_N > 10$; Table 2).

High Mg# of primary adakitic magma

There are three types of phenocrysts in the Heishantou diorite: plagioclase, amphibole and clinopyroxene. Plagioclase phenocrysts exhibit low An (mostly 24–50 mol %; Fig. 7a), which cannot be formed in the early magmatic stage. Amphibole and clinopyroxene phenocrysts are euhedral–subhedral prismatic or show polygon cross-sections (Fig. 2b–d), indicating that they are magmatic crystals. Chemical compositions of the cores and rims of clinopyroxene phenocrysts and the matrix ones change coherently (Fig. 9), suggesting clinopyroxene phenocrysts are intrinsic magmatic crystals of Heishantou diorite. A few amphibole crystals are partially enclosed by large clinopyroxenes (Fig. 2c) and amphibole crystals show similar REE patterns as clinopyroxenes (Figs. 12 and 13), indicating they were formed in the same magmatic system. Furthermore, calculated melts in equilibrium with clinopyroxene (see details in Table 5) and amphibole phenocrysts (see details in Table 6) all have similar REE patterns to the Heishantou diorites (Fig. 5a). Thus clinopyroxenes and amphiboles are cognate magmatic minerals of the Heishantou magma, and the core-rim compositional zonation of clinopyroxene phenocrysts (Fig. 10) could be due to multiple processes during magma evolution.

For the sector-zoned clinopyroxene cores, the hourglass sectors are compositionally different from the prism sectors (Fig. 10), which would be induced by different growth rates of two types of sectors because the incorporation of Al in tetrahedral coordination due to slow-growing in prism sector will promote the incorporation of HFSE and REE (Mollo & Hammer, 2017; Ubide *et al.*, 2019). Thus the sector-zoning is not necessarily associated with mixing or mingling process between different magmas, but would be developed in response to low degrees of undercooling, such as during slow magma ascent (Mollo & Hammer, 2017; Ubide *et al.*, 2019). Although hourglass sector grows faster than prism sector, the presence of sector-zoning represents a slow crystal growth rate, and two types of sectors can remain in local chemical equilibrium with the circumjacent melt (Ubide *et al.*, 2019). Therefore, the composition of sector-zoned cores would be reliable in characterizing the primary magmas of Heishantou diorites.

Both amphibole and clinopyroxene phenocrysts show high $Mg^{\#}$, with the former most likely crystallizing subsequent to the formation of the high $Mg^{\#}$ core of zoned clinopyroxene phenocrysts based on the following observations. The Dy/Yb ratios and TiO_2 contents of the zoned clinopyroxene phenocrysts are high in the cores and decrease to the rims (Fig. 11g). Since middle rare earth elements (MREE) are more compatible than HREE in amphibole (Dalpe & Baker, 2000; Hilyard *et al.*, 2000; Shimizu *et al.*, 2017), fractional crystallization of amphibole will lower Dy/Yb ratios in the melt. In addition, since amphibole is a titanium-rich mineral in basalt-andesite melts in contrast to clinopyroxene, its

Table 4: In situ plagioclase Sr isotopes of the Heishantou diorite

Spot	^{88}Sr (V)	^{85}Rb (V)	$^{87}Sr/^{86}Sr$	$^{87}Rb/^{86}Sr$	SiO_2	Al_2O_3	FeO^T	CaO	SrO	Na_2O	K_2O	Total	An%	Ab%	Or%
Line AA′															
#1	4·2	0·001	0·70459 ± 4	0·000692 ± 9	58·96	25·74	0·15	7·36	0·21	6·64	0·63	99·69	36·6	59·7	3·7
#2	3·8	0·001	0·70453 ± 4	0·000770 ± 7	60·10	25·07	0·14	6·60	0·18	6·90	0·74	99·73	33·0	62·6	4·4
#3	4·2	0·001	0·70450 ± 5	0·000936 ± 6	59·61	25·45	0·14	6·94	0·21	6·78	0·74	99·89	34·5	61·1	4·4
#4	4·9	0·005	0·70468 ± 4	0·003248 ± 11	60·93	24·71	0·18	5·99	0·25	7·09	1·04	100·19	29·9	64·0	6·2
#5	6·2	0·002	0·70494 ± 4	0·000847 ± 5	59·42	25·14	0·19	6·79	0·33	6·74	0·81	99·45	34·1	61·1	4·8
#6	7·1	0·002	0·70503 ± 3	0·000930 ± 7	59·80	24·93	0·20	6·47	0·42	6·74	0·91	99·54	32·7	61·8	5·5
#7	8·0	0·021	0·70501 ± 3	0·008240 ± 107	59·65	24·54	0·20	6·04	0·36	5·74	2·77	99·87	30·6	52·7	16·7
Line BB′															
#1	5·3	0·001	0·70447 ± 4	0·000472 ± 94	55·13	27·75	0·15	9·73	0·26	5·38	0·44	98·85	48·7	48·7	2·6
#2	4·8	0·002	0·70451 ± 5	0·001496 ± 250	56·88	26·60	0·14	8·49	0·21	6·09	0·55	98·98	42·1	54·7	3·3
#3	5·2	0·006	0·70454 ± 4	0·003326 ± 127	55·39	27·47	0·16	9·46	0·24	5·58	0·49	98·80	47·0	50·1	2·9
#4	4·5	0·003	0·70453 ± 5	0·001594 ± 143	57·15	26·52	0·16	8·27	0·22	6·15	0·63	99·09	41·0	55·2	3·7
#5	5·6	0·008	0·70478 ± 4	0·003877 ± 158	57·28	26·55	0·18	8·28	0·26	6·13	0·64	99·34	41·1	55·1	3·8
Line CC′															
#1	4·7	0·001	0·70451 ± 4	0·000631 ± 16	55·44	27·21	0·20	9·41	0·23	5·70	0·32	98·50	46·8	51·3	1·9
#2	4·6	0·002	0·70460 ± 4	0·001177 ± 12	56·46	26·99	0·16	8·98	0·22	6·00	0·41	99·22	44·2	53·4	2·4
#3	5·0	0·001	0·70458 ± 3	0·000347 ± 5	56·04	26·84	0·16	8·95	0·24	5·98	0·39	98·61	44·2	53·5	2·3
#4	4·6	0·001	0·70456 ± 4	0·000681 ± 6	59·22	25·18	0·14	6·94	0·19	6·97	0·66	99·31	34·1	62·0	3·9
#5	3·9	0·002	0·70454 ± 4	0·001208 ± 7	60·65	24·33	0·15	6·03	0·17	7·38	0·79	99·50	29·7	65·7	4·6
#6	4·2	0·002	0·70461 ± 4	0·001574 ± 8	60·58	24·40	0·16	6·01	0·19	7·40	0·85	99·60	29·4	65·6	5·0
#7	7·0	0·003	0·70487 ± 3	0·001262 ± 16	59·16	25·23	0·19	6·69	0·33	6·84	0·71	99·20	33·6	62·2	4·2
#8	8·7	0·003	0·70498 ± 3	0·001158 ± 15	58·16	25·44	0·22	7·33	0·41	6·55	0·81	98·98	36·4	58·9	4·8
#9	8·7	0·007	0·70503 ± 3	0·002528 ± 22	59·17	25·08	0·24	6·70	0·39	6·82	0·93	99·38	33·3	61·3	5·5
Line DD′-EE′															
#1	5·9	0·002	0·70480 ± 4	0·000737 ± 6	58·73	26·09	0·18	7·52	0·29	6·53	0·53	99·89	37·6	59·2	3·2
#2	6·1	0·002	0·70487 ± 4	0·000807 ± 4	59·55	25·57	0·17	7·00	0·30	6·83	0·56	99·97	34·9	61·7	3·3
#3	6·3	0·002	0·70484 ± 3	0·000890 ± 10	58·97	25·63	0·21	7·38	0·29	6·66	0·55	99·71	36·7	60·0	3·2
#4	5·9	0·002	0·70492 ± 4	0·000834 ± 5	59·63	25·14	0·18	6·69	0·30	6·88	0·66	99·49	33·6	62·5	3·9
#5	6·1	0·002	0·70479 ± 4	0·001213 ± 16	56·99	26·87	0·18	8·53	0·32	5·91	0·51	99·31	43·0	53·9	3·0
#6	5·5	0·005	0·70484 ± 3	0·002677 ± 9	60·20	25·13	0·17	6·52	0·30	6·90	0·88	100·11	32·5	62·3	5·2
Line FF′															
#1	4·5	0·020	0·70453 ± 4	0·012338 ± 705	57·69	26·09	0·19	7·92	0·23	6·37	0·47	98·96	39·6	57·6	2·8
#2	5·8	0·007	0·70444 ± 3	0·003450 ± 57	52·05	29·01	0·19	11·64	0·27	4·28	0·22	97·67	59·3	39·4	1·3
#3	5·5	0·006	0·70454 ± 4	0·003702 ± 44	56·06	27·45	0·16	9·17	0·36	5·67	0·28	99·15	46·4	51·9	1·7
#4	5·2	0·006	0·70464 ± 3	0·003672 ± 170	57·02	26·50	0·19	8·33	0·24	5·93	0·57	98·78	42·2	54·4	3·5
#5	4·2	0·004	0·70476 ± 4	0·003191 ± 50	59·99	24·82	0·17	6·29	0·26	6·90	0·90	99·33	31·7	62·9	5·4
Line GG′															
#1	4·1	0·002	0·70474 ± 5	0·001132 ± 26	58·59	25·67	0·16	7·28	0·24	6·59	0·68	99·21	36·4	59·6	4·0
#2	3·7	0·002	0·70479 ± 5	0·001736 ± 27	59·21	25·31	0·17	6·93	0·26	6·85	0·77	99·50	34·3	61·2	4·5
#3	4·9	0·004	0·70484 ± 4	0·002333 ± 42	55·93	27·22	0·18	9·08	0·30	5·70	0·51	98·94	45·4	51·6	3·0
#4	4·4	0·004	0·70491 ± 4	0·002823 ± 16	61·06	24·27	0·22	5·80	0·23	7·25	1·02	99·88	28·8	65·2	6·0
#5	4·9	0·005	0·70486 ± 5	0·003554 ± 61	60·21	24·66	0·18	6·19	0·29	7·08	0·99	99·64	30·7	63·5	5·8
#6	5·1	0·005	0·70505 ± 4	0·002777 ± 28	60·00	24·83	0·17	6·28	0·33	6·93	1·08	99·65	31·3	62·4	6·4

^{88}Sr and ^{85}Rb are the signal intensities.
An=Ca/(Na+K+Ca)×100, Ab=Na/(Na+K+Ca)×100, Or=K/(Na+K+Ca)×100.
Major elements' values are the average results of 4 points evenly surrounding the corresponding Sr isotopic ablation circle via CAMECA SX-Five FE EPMA in GIG-CAS.

saturation will also lower Ti contents in the melts. Thus, although a few amphiboles are partly enclosed by clinopyroxene phenocrysts, notable fractional crystallization of amphibole shortly after the crystallization of the cores of zoned clinopyroxene phenocrysts is needed to explain the decreasing Dy/Yb ratios and TiO_2 contents in rims of the zoned clinopyroxenes. Amphiboles in the Heishantou diorite show overall higher $Mg^{\#}$ (73–77) than those crystallizing from arc-related adakitic magmas ($Mg^{\#} \leq \sim 75$, Rodriguez *et al.*, 2007; Rooney *et al.*, 2011; Fig. 14b). The calculated melt in equilibrium with amphibole would have $Mg^{\#}$ of 44–51 when using $D_{Fe-Mg}^{amp-liq} = 0{\cdot}30$ (0·38–0·30 in the basaltic and andesitic system; Sisson & Grove, 1993; Nandedkar *et al.*, 2014) (Table 6). The cores of clinopyroxene phenocrysts also exhibit high $Mg^{\#}$ of 78–84, indicating high $Mg^{\#}$ of the primary magma. The Fe–Mg exchange partition coefficient between clinopyroxene and silicate melts varies over a wide range ($D_{Fe-Mg}^{cpx-liq} = 0{\cdot}28 \pm 0{\cdot}08$; Putirka, 2008), which is correlated with magmatic composition, oxygen fugacity, and temperature. Because $D_{Fe-Mg}^{cpx-liq}$ is systematically higher in basaltic melts (Kinzler, 1997; Bédard, 2014), and the estimated melt in equilibrium with amphiboles using chemometric equations by Zhang *et al.* (2017) and Humphreys *et al.* (2019) has SiO_2 contents of 51–58 wt %, it is reasonable to use a relatively high $D_{Fe-Mg}^{cpx-liq}$ ($\geq 0{\cdot}28$) for the compositional estimation of melts in equilibrium with the cores of clinopyroxene phenocrysts. The calculated $Mg^{\#}$ ($\geq$ 50–60; Supplementary Data Table S2, S5; supplementary

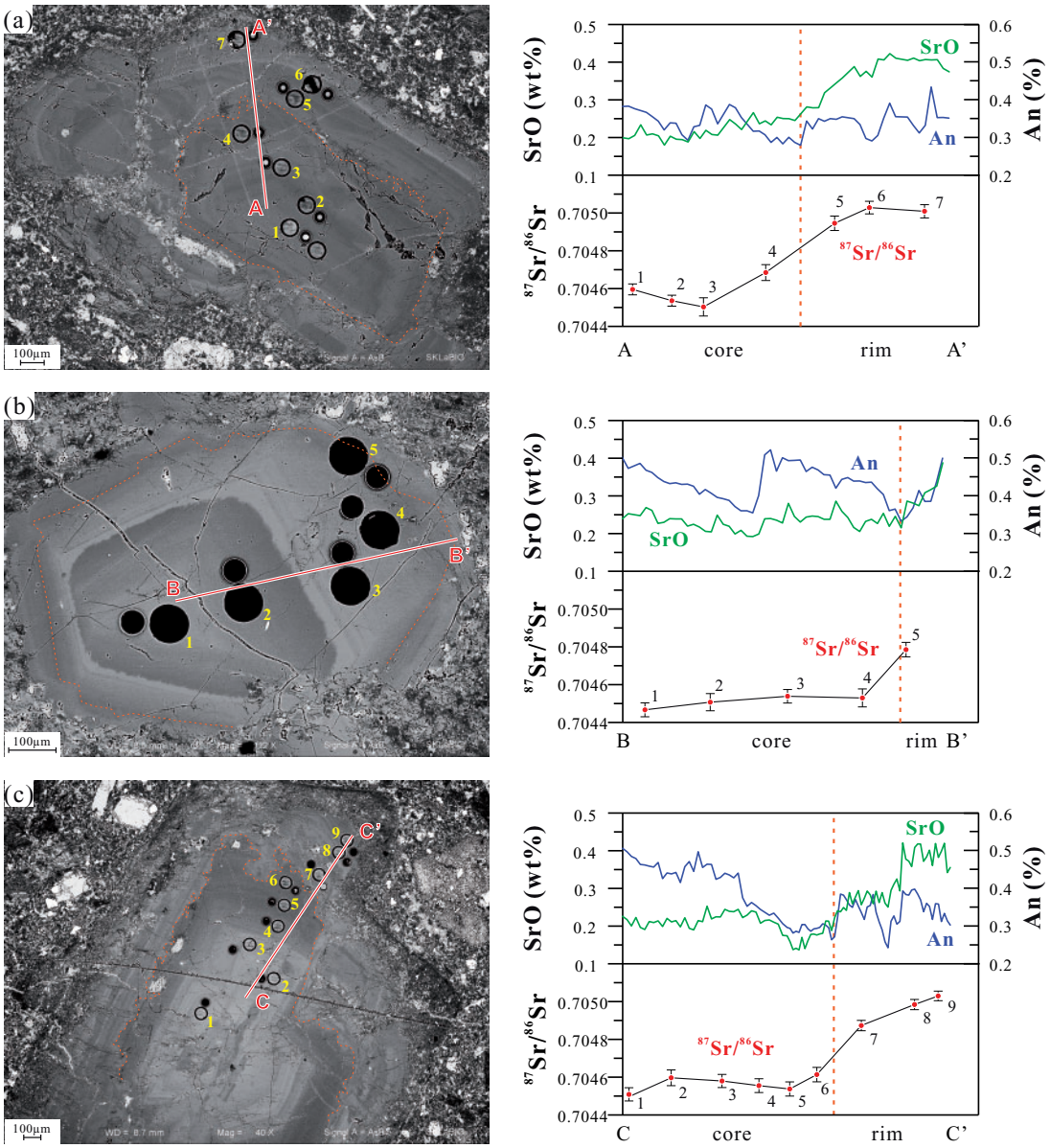

Fig. 8 BSE images, *in situ* Sr isotope and traverse analyses (SrO and An) of representative plagioclase phenocrysts in the Heishantou diorite. The boundary between the core and rim of the zoned plagioclase phenocryst is resorbed. $^{87}Sr/^{86}Sr$ and SrO contents overall increase from the core to rim.

data are available for downloading at http://www.petrology.oxfordjournals.org) is higher than that in equilibrium with amphibole, consistent with the supposition that clinopyroxene cores crystallized earlier than amphiboles. Therefore, the high $Mg^{\#}$ core of the zoned clinopyroxene phenocrysts records the earliest high-$Mg^{\#}$ characteristics of the Heishantou diorites.

The clinopyroxene phenocrysts in the Heishantou diorites have significantly higher Sr content and La/Yb ratios and lower Y and Yb content (Table 5) than those in the Aleutian primitive adakites derived from slab melts interacted with mantle olivine (Yogodzinski & Kelemen, 1998) (Fig. 11a–d). Calculated melts in equilibrium with zoned clinopyroxene phenocrysts change gradually from adakitic in the core towards low Sr/Y and high Yb, Y and La/Yb in the rim (Fig. 15), suggesting that the initial melts in equilibrium with the high-$Mg^{\#}$ cores of the zoned clinopyroxene phenocrysts were adakitic. Consistently, amphibole phenocrysts in the Heishantou diorites show much higher Sr/Y (53–127) and lower Y (6·14–14·6 ppm; Table 6) than those formed in arc lavas (Ewart & Taylor 1969; Samaniego *et al.*, 2010; Chiaradia *et al.*, 2011; Tiepolo *et al.*, 2012; Johnson *et al.*, 2013; Fig. 14a). They also have higher Sr/Y than the amphiboles in adakites formed by fractional crystallization of amphibole (e.g. Adamello in Central Alps; Tiepolo *et al.*, 2011) or low degree melting of a peridotitic mantle source interacted with slab melt

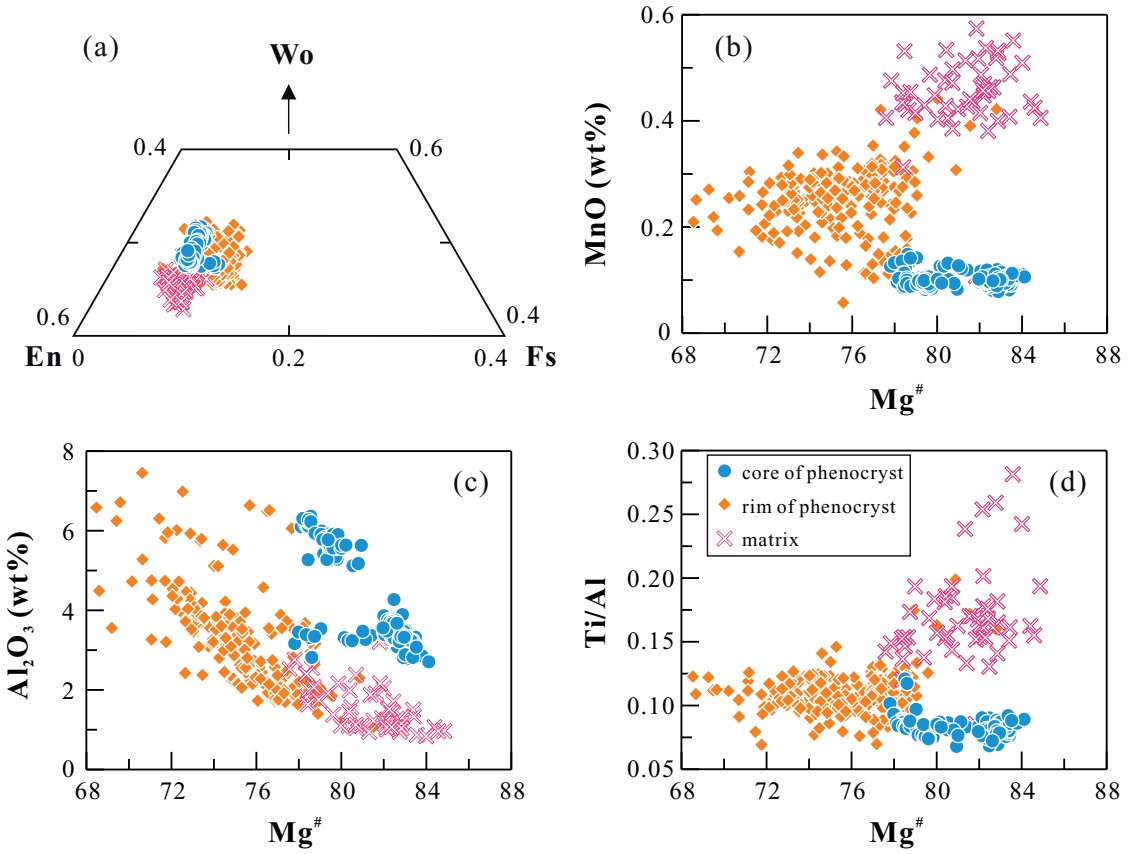

Fig. 9 (a) Pyroxene Wo–En–Fs triangular classification diagram; (b–d) MnO, Al_2O_3 and Ti/Al vs $Mg^{\#}$ for clinopyroxenes in the Heishantou diorite.

(e.g. Solander and Little Solander Islands in New Zealand; Foley *et al.*, 2013). Therefore, the early melt of the Heishantou diorite was likely adakitic.

The melts in equilibrium with the cores of the zoned clinopyroxene phenocrysts are high in Sr/Y and La/Yb, which is likely derived from partial melting of a deep source with residual garnet. Although high-pressure fractional crystallization of amphibole or garnet in early magma can also result in adakitic melts (Macpherson *et al.*, 2006; Alonso-Perez *et al.*, 2009; Zellmer *et al.*, 2012), it is not applicable to the Heishantou primary magmas for the following reasons: (i) notable fractionation of amphibole in the Heishantou diorite was after the formation of clinopyroxene cores; (ii) calculated oxygen fugacity using amphibole thermobarometor by Ridolfi *et al.* (2010) is about NNO + 1 (Table 6), indicating that the initial fO_2 is lower than NNO + 1 because the early fractionation of low ferric minerals (e.g. olivine and clinopyroxene) can effectively increase magmatic fO_2. This contradicts with the oxidizing condition (NNO + 5·5; Ulmer *et al.*, 2018) required for the formation of amphibole-rich cumulates (Alonso-Perez *et al.*, 2009); (iii) calculated water contents using amphibole thermobarometor by Ridolfi *et al.* (2010) (~ 5·4 wt %; Table 6) are lower than the required H_2O-rich conditions for stability of early igneous amphibole/garnet in andesitic liquids (H_2O > 7 wt % for equilibrium melts; Alonso-Perez *et al.*, 2009); (iv) the Heishantou amphibole phenocrysts have much higher F content and lower H_2O content than those from arc-related adakites (Rodriguez *et al.*, 2007; Rooney *et al.*, 2011) (Fig. 14b), indicating distinctive fluid compositions and excluding high-pressure fractional crystallization of high H_2O and low F amphibole that specifically occurred in an arc system (Macpherson *et al.*, 2006); and (v) garnet fractionation is always accompanied by clinopyroxene or amphibole crystallization in andesitic liquids (Alonso-Perez *et al.*, 2009), meaning the early fractionation of garnet would induce a continuous decrease of Al_2O_3 contents in the melts, which is clearly in contradiction with the trend of increasing Al_2O_3 from cores to rims of zoned clinopyroxene phenocrysts in the Heishantou diorites (Fig. 9). On the contrary, the Heishantou diorites have higher Nb/Ta ratios (15−8) than depleted mantle and MORB (Nb/Ta = ~15·5; Jochum *et al.*, 1997). Because amphibole/melt D_{Nb}/D_{Ta} is generally > 1·20 for arc magmas or the low H_2O magmas at high temperature (Li *et al.*, 2017), the later fractionation of amphiboles in the Heshantou diorites should have decreased Nb/Ta ratios of the residual magma, indicating intrinsically high Nb/Ta ratios of the primitive magmas, consistent with a deep melt source with residual rutile (Xiong *et al.*, 2005a; Moyen, 2009). Batch melting calculation of the Western Tianshan lower crust (using a mean value of granulite xenoliths from Zheng et al., 2006) with eclogite (0·7 clinopyroxene + 0·29 garnet + 0·01 rutile) as

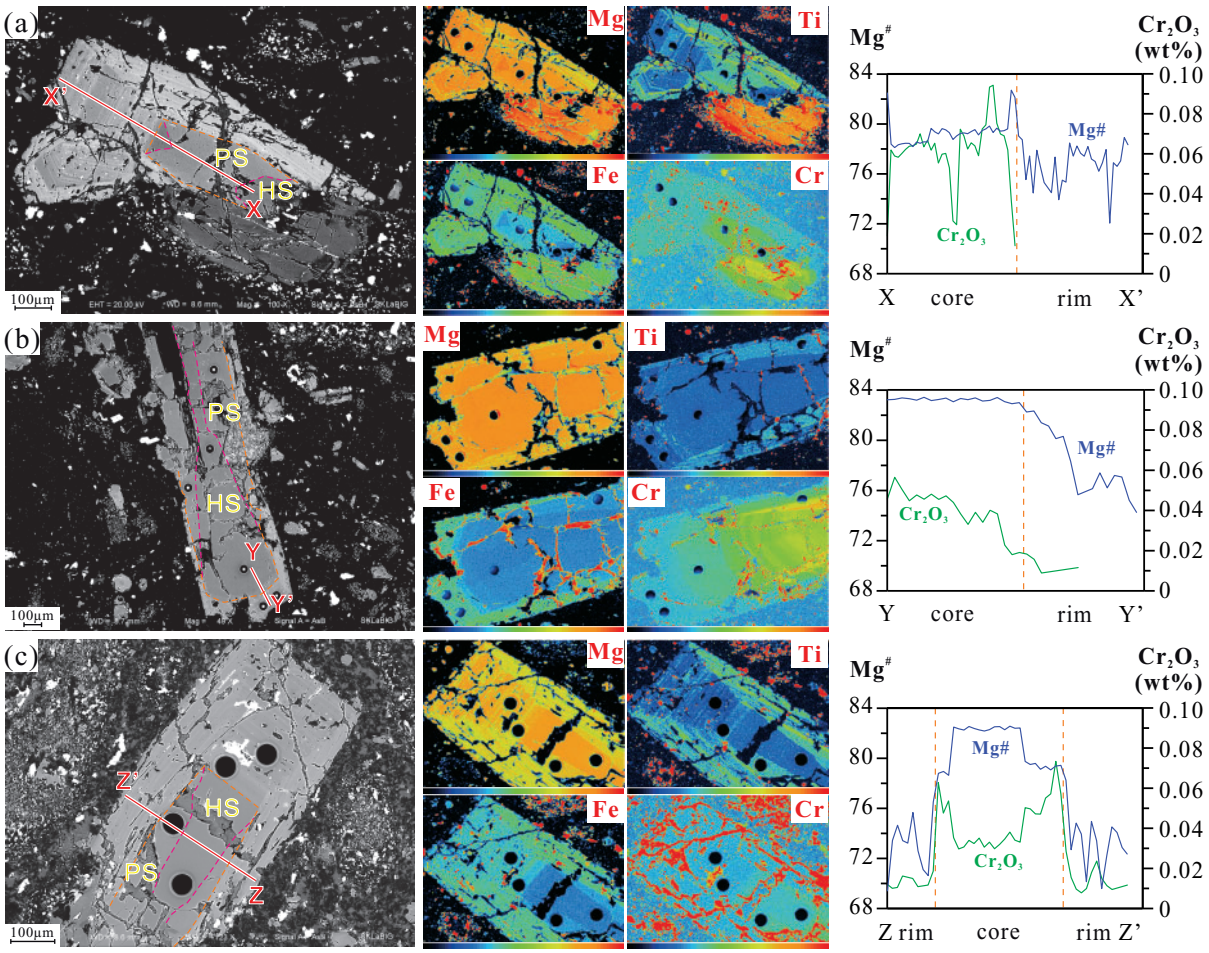

Fig. 10 BSE images, elemental (Mg, Fe, Ti, Cr) X-ray maps and traverse analyses (Cr_2O_3 and $Mg^{\#}$) of representative clinopyroxene phenocrysts in the Heishantou diorite. The sector-zoned core consists of homogeneous prism and hourglass sectors (PS and HS, respectively) and has high $Mg^{\#}$, while the rim shows the oscillatory zoning and has low $Mg^{\#}$. The scale of color bars for Mg, Fe, Ti and Cr X-ray maps are 0–100, 0–20, 0–4 and 0–16 cts/nA from dark blue to red, respectively.

restite matches high Sr/Y and La/Yb characteristics of the whole-rock, and calculated melts in equilibrium with the cores of clinopyroxenes and amphiboles (Fig. 15), confirming the involvement of garnet as a residual phase in the source. Therefore, the primary melts of Heishantou diorite are adakitic.

The high-$Mg^{\#}$ cores of zoned clinopyroxene phenocrysts have higher Cr and Ni than the low-$Mg^{\#}$ rims (Fig. 11e–f), suggesting that the early magma had higher Cr and Ni than the later melt. However, because the whole-rock geochemistry mainly depends on the composition of the later-evolved magma, the whole-rock Cr and Ni content of the Heishantou diorites is less than that of adakites derived from the partial melting of delaminated lower crust (Fig. 4d). Collectively, the primary adakitic melts related to the Heishantou diorite should be characterized by high $Mg^{\#}$ and low SiO_2 with high Cr and Ni content.

Petrogenesis of high-$Mg^{\#}$ adakitic rocks

Adakitic rocks can be formed by various mechanisms, such as partial melting of subducted oceanic slab with overlying mantle (Kay *et al.*, 1993; Drummond *et al.*, 1996; Rapp *et al.*, 1999; Martin *et al.*, 2005) or enriched mantle metasomatized by slab-derived adakite melts (Gao *et al.*, 2007), partial melting of delaminated lower continental crust (Xu *et al.*, 2002; Wang *et al.*, 2006a), thickened lower crust (Atherton & Petford, 1993; Hou *et al.*, 2004; Wang *et al.*, 2005; Huang *et al.*, 2009) or adakitic crust (Moyen, 2009; Ma *et al.*, 2015), high-pressure early fractional crystallization of a mantle-derived hydrous mafic parental magma (Macpherson *et al.*, 2006; Alonso-Perez *et al.*, 2009), or later assimilation and fractional crystallization (AFC) or mixing processes (Streck *et al.*, 2007; Chiaradia *et al.*, 2009; Castillo, 2012).

High-pressure melting of thickened lower crust, adakitic crust or oceanic slab would produce relatively low-$Mg^{\#}$ and high-SiO_2 adakitic melt (Atherton & Petford, 1993; Hou *et al.*, 2004; Huang *et al.*, 2009; Qian & Hermann, 2013), which is inconsistent with the primary high-$Mg^{\#}$ and low-SiO_2 melts of the Heishantou diorites. The models of high-pressure fractional crystallization, AFC and mixing processes could also be excluded because the early fractionation of garnet/amphibole

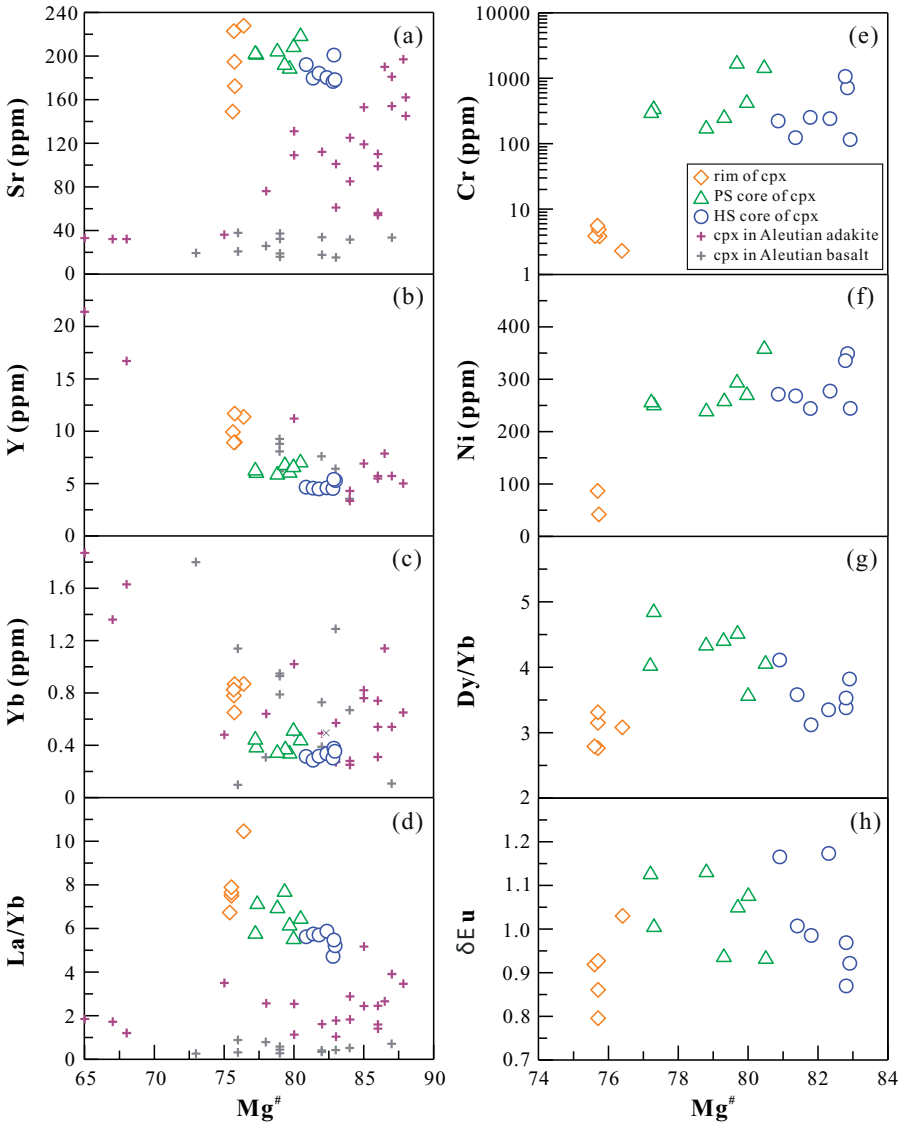

Fig. 11 Variation diagrams for representative trace elements concentrations or values of the clinopyroxene phenocrysts in the Heishantou diorite: Sr, Y, Yb, La/Yb, Cr, Ni, Dy/Yb and δEu vs $Mg^{\#}$. PS and HS are abbreviations for prism-sector and hourglass-sector, respectively. Clinopyroxene compositional data of Aleutian primitive adakites and arc basalts are from Yogodzinski & Kelemen (1998).

does not account for the primitively adakitic feature of the Heishantou diorites. The model of partial melting of subducted oceanic crust is most likely inapplicable to the Heishantou adakitic rocks because the subduction of the Northern and Southern Tianshan oceans beneath the Western Tianshan likely terminated before the Early Permian (~ 320–300 Ma; Gao *et al.*, 2011; Han *et al.*, 2011 and references therein). In addition, the Heishantou samples show relatively enriched Sr–Nd–Hf isotopes that are different from depleted MORB (Stracke *et al.*, 2005) and Carboniferous adakitic rocks derived from partial melting of subducted oceanic crust in the Tianshan orogenic belt (Zhang et al., 2006; Wang et al., 2007b, 2016, 2018; Liu et al., 2016; Du et al., 2019; Fig. 6a, b). Adjacent Permian magmatic rocks are bimodal rocks or A-type granitoids (Ye *et al.*, 2013; Li *et al.*, 2015a), consistent with a postorogenic extension setting. Partial melting of enriched mantle previously metasomatized by slab-derived adakite melts will produce a melt enriched in HFSE (Bourdon *et al.*, 2002; Martin *et al.*, 2005; Gao *et al.*, 2007), which is inconsistent with the HFSE-depleted feature of the Heishantou diorite samples (Fig. 5b).

Melting of thickened lower crust induced by mafic magma underplating is essentially a mixing model, which may result in reverse zoning, resorption surface, or composition gap in early minerals (Streck *et al.*, 2007; Chen *et al.*, 2013) when the time period before eruption is insufficient for the melt homogeneous. Both the early clinopyroxene and later low-An plagioclase show compositional zoning (Fig. 2, Fig. 8 and Fig. 10), indicating an overall heterogeneous melt throughout the magmatic evolution. However, clinopyroxene phenocrysts show normal zoning and have similar trace

Table 5: LA-ICP-MS in situ major (wt %) and trace (ppm) elements concentrations of clinopyroxene phenocrysts in the Heishantou diorites

Spot	Cpx-1			Cpx-2			Cpx-3			Cpx-4		Cpx-5		Cpx-6			Cpx-7		
	HSC	PSC	R	HSC	PSC	R	HSC	PSC	R	HSC	PSC	HSC	PSC	HSC	PSC	R	HSC	PSC	R
SiO_2	49·34	46·93	48·32	49·54	48·13	49·56	51·80	48·14	49·09	48·77	47·32	48·86	47·38	50·34	47·43	50·19	49·82	47·99	50·23
TiO_2	0·38	0·65	0·35	0·39	0·58	0·37	0·39	0·72	0·47	0·40	0·68	0·42	0·73	0·42	0·67	0·33	0·46	0·81	0·37
Al_2O_3	3·40	5·13	2·25	3·42	5·34	2·36	3·12	5·25	3·09	3·76	6·02	3·14	5·56	3·26	5·03	1·81	3·48	5·61	2·09
FeO^T	6·51	7·14	8·78	5·80	6·29	8·31	6·08	7·23	8·35	6·13	6·76	6·19	6·98	6·24	7·15	8·52	6·40	7·32	8·33
MnO	0·11	0·10	0·30	0·11	0·10	0·28	0·11	0·10	0·17	0·10	0·10	0·11	0·10	0·11	0·10	0·31	0·11	0·11	0·26
MgO	17·03	15·98	15·94	15·71	14·53	14·56	15·30	13·81	14·59	16·54	14·86	16·87	15·02	15·27	14·90	14·83	15·16	13·92	14·57
CaO	22·52	23·23	22·91	24·25	24·01	23·69	22·52	23·94	23·50	23·41	23·19	23·76	23·42	23·68	23·94	23·24	23·87	23·39	23·39
Na_2O	0·35	0·42	0·44	0·36	0·45	0·39	0·37	0·43	0·36	0·40	0·48	0·31	0·42	0·35	0·42	0·38	0·37	0·45	0·38
$Mg^{\#}$	82·3	80·0	76·4	82·8	80·5	75·7	81·8	77·3	75·7	82·8	79·7	82·9	79·3	81·4	78·8	75·6	80·9	77·2	75·7
Sc	70·7	91·3	43·4	81·3	96·3	44·4	70·3	84·6	77·6	79·0	90·2	88·2	96·8	73·3	86·7	41·0	75·4	91·3	50·4
V	133	185	150	136	188	164	136	189	191	152	211	129	195	138	198	143	145	200	161
Cr	242	449	2·30	716	1531	3·84	253	361	5·59	1068	1789	116	265	124	182	3·87	223	314	4·87
Co	37·3	33·9	38·4	35·5	34·5	40·4	33·5	34·4	44·2	35·9	33·8	35·8	33·5	36·0	35·4	39·1	36·5	36·0	41·3
Ni	278	274	bdl	350	362	bdl	245	254	87·0	336	298	245	262	269	243	bdl	272	260	42·1
Sr	180	210	228	201	220	172	184	203	223	177	190	178	194	180	206	149	192	204	195
Y	4·56	6·74	11·4	5·39	7·18	11·7	4·46	6·18	8·91	4·52	6·20	5·32	6·89	4·55	6·02	9·91	4·65	6·42	8·92
Zr	9·95	18·2	25·4	10·6	17·7	27·2	10·2	16·6	31·0	8·72	15·8	11·7	19·8	10·1	16·7	21·7	10·1	19·9	23·4
Nb	0·01	0·01	bdl	0·01	0·02	0·02	bdl	0·02	0·02	0·01	0·01	0·02	0·01	0·06	0·01	0·03	bdl	0·04	0·02
La	1·97	2·94	9·09	2·07	2·95	6·86	1·80	2·86	6·71	1·43	2·18	1·84	2·99	1·63	2·49	5·58	1·77	2·67	4·87
Ce	10·1	14·6	35·1	10·0	14·0	29·3	9·27	13·3	27·0	7·19	11·0	9·63	13·4	8·80	13·4	25·9	9·41	13·8	23·1
Pr	2·03	3·19	6·25	2·23	3·02	5·88	1·80	3·11	5·32	1·67	2·38	2·12	2·92	1·80	2·90	5·18	2·01	2·79	4·63
Nd	12·6	18·1	33·1	13·9	18·7	32·0	11·7	17·7	27·3	10·2	14·8	12·8	18·4	11·4	15·7	27·6	11·5	17·1	24·8
Sm	3·22	4·94	7·09	3·79	4·65	7·15	2·86	4·48	5·65	2·44	3·96	3·40	5·06	3·16	4·03	6·32	3·10	3·96	5·91
Eu	1·05	1·53	2·04	0·93	1·24	1·75	0·86	1·24	1·65	0·70	1·22	0·89	1·33	0·88	1·29	1·64	1·02	1·31	1·58
Gd	2·03	3·42	4·54	2·50	3·16	4·83	2·35	2·71	7·13	1·85	2·90	2·29	3·25	1·96	2·66	4·18	2·05	2·91	4·16
Tb	0·22	0·38	0·64	0·27	0·36	0·55	0·22	0·30	0·46	0·22	0·33	0·26	0·37	0·17	0·32	0·50	0·23	0·36	0·43
Dy	1·13	1·88	2·68	1·33	1·84	2·73	0·99	1·93	2·43	1·02	1·59	1·35	1·70	1·02	1·55	2·31	1·29	1·85	2·15
Ho	0·19	0·33	0·64	0·22	0·29	0·45	0·18	0·25	0·41	0·18	0·28	0·22	0·29	0·19	0·26	0·39	0·22	0·24	0·34
Er	0·51	0·69	1·24	0·54	0·64	1·13	0·46	0·78	1·07	0·46	0·60	0·51	0·72	0·46	0·60	1·03	0·46	0·64	0·88
Tm	0·06	0·09	0·22	0·07	0·09	0·15	0·06	0·07	0·14	0·06	0·06	0·07	0·09	0·07	0·07	0·14	0·06	0·09	0·13
Yb	0·34	0·52	0·87	0·38	0·45	0·87	0·32	0·40	0·88	0·30	0·35	0·35	0·38	0·29	0·36	0·83	0·31	0·46	0·65
Lu	0·04	0·05	0·20	0·04	0·06	0·13	0·04	0·06	0·09	0·03	0·05	0·07	0·07	bdl	0·05	0·13	0·06	0·06	0·08
Hf	0·59	0·99	1·40	0·52	0·97	1·18	0·50	0·98	1·56	0·54	0·87	0·64	1·03	0·45	0·88	0·96	0·56	1·14	0·97
Ta	bdl	bdl	0·13	bdl	bdl	bdl	bdl	bdl	bdl	bdl	bdl	0·02	bdl	bdl	bdl	0·01	0·02	bdl	bdl
Pb	1·25	0·09	0·55	0·16	0·14	0·36	0·09	0·15	0·14	0·16	0·12	0·13	0·13	0·12	0·19	0·44	0·16	0·18	0·27
Th	0·03	0·02	0·20	0·02	0·03	0·06	0·03	0·03	0·05	0·01	0·02	0·01	0·03	bdl	0·03	0·09	0·03	0·04	0·06
U	0·04	bdl	0·20	bdl	0·01	0·01	bdl	bdl	0·01	bdl	bdl	0·01	bdl	bdl	0·01	0·05	0·01	bdl	0·02
Dy/Yb	3·32	3·62	3·08	3·50	4·09	3·14	3·09	4·83	2·76	3·40	4·54	3·86	4·47	3·52	4·31	2·78	4·16	4·02	3·31
Sr/Y	39·5	31·2	20·0	37·3	30·6	14·7	41·3	32·8	25·0	39·2	30·6	33·5	28·2	39·6	34·2	15·0	41·3	31·8	21·9
La/Yb	5·79	5·65	10·45	5·45	6·56	7·89	5·63	7·15	7·64	4·77	6·23	5·26	7·87	5·62	6·92	6·72	5·71	5·80	7·49

(continued)

Table 5:. Continued

Spot	Cpx-1			Cpx-2			Cpx-3			Cpx-4		Cpx-5		Cpx-6			Cpx-7		
	HSC	PSC	R	HSC	PSC	R	HSC	PSC	R	HSC	PSC	HSC	PSC	HSC	PSC	R	HSC	PSC	R
δEu	1·17	1·08	1·03	0·87	0·94	0·86	0·99	1·01	0·80	0·97	1·05	0·92	0·94	1·01	1·13	0·92	1·17	1·13	0·93
trace elements partition coefficients calculated using equations established by Bédard (2014)																			
D_{La}	0·10	0·08	0·09	0·10	0·09	0·10	0·12	0·09	0·09	0·09	0·08	0·09	0·08	0·10	0·08	0·10	0·10	0·09	0·10
D_{Ce}	0·12	0·10	0·11	0·12	0·11	0·12	0·15	0·11	0·12	0·12	0·10	0·12	0·10	0·13	0·10	0·13	0·13	0·11	0·13
D_{Pr}	0·18	0·15	0·17	0·19	0·17	0·19	0·22	0·17	0·18	0·17	0·16	0·18	0·16	0·20	0·16	0·19	0·19	0·16	0·20
D_{Nd}	0·26	0·22	0·24	0·26	0·24	0·26	0·31	0·24	0·26	0·25	0·22	0·25	0·22	0·28	0·22	0·28	0·27	0·23	0·28
D_{Sm}	0·40	0·34	0·37	0·41	0·37	0·41	0·49	0·37	0·40	0·39	0·35	0·39	0·35	0·44	0·35	0·43	0·42	0·37	0·43
D_{Gd}	0·50	0·42	0·47	0·51	0·46	0·51	0·59	0·46	0·49	0·48	0·43	0·48	0·44	0·54	0·44	0·53	0·52	0·46	0·53
D_{Tb}	0·55	0·47	0·52	0·56	0·51	0·56	0·65	0·51	0·54	0·53	0·48	0·54	0·49	0·59	0·49	0·58	0·57	0·51	0·59
D_{Dy}	0·56	0·49	0·53	0·57	0·52	0·57	0·66	0·52	0·56	0·54	0·50	0·55	0·50	0·60	0·50	0·59	0·58	0·52	0·60
D_{Ho}	0·55	0·48	0·52	0·55	0·51	0·55	0·62	0·51	0·54	0·53	0·49	0·53	0·49	0·58	0·49	0·57	0·56	0·51	0·57
D_{Er}	0·52	0·46	0·50	0·53	0·49	0·53	0·60	0·49	0·52	0·51	0·47	0·51	0·47	0·55	0·47	0·55	0·54	0·49	0·55
D_{Tm}	0·55	0·48	0·52	0·55	0·52	0·55	0·62	0·52	0·54	0·53	0·49	0·54	0·50	0·58	0·50	0·57	0·56	0·51	0·57
D_{Yb}	0·54	0·48	0·51	0·54	0·50	0·54	0·61	0·50	0·53	0·52	0·48	0·52	0·49	0·56	0·49	0·56	0·55	0·50	0·56
D_{Lu}	0·54	0·48	0·52	0·55	0·51	0·55	0·61	0·51	0·54	0·53	0·49	0·53	0·49	0·57	0·49	0·57	0·56	0·51	0·57
D_{Y}	0·57	0·49	0·53	0·57	0·53	0·57	0·65	0·53	0·56	0·55	0·50	0·55	0·51	0·60	0·51	0·59	0·58	0·52	0·60
D_{Sr}	0·08	0·08	0·08	0·08	0·08	0·08	0·08	0·08	0·08	0·08	0·08	0·08	0·08	0·08	0·08	0·08	0·08	0·08	0·08
composition of melt equilibrating with clinopyroxenes																			
$(La/Yb)_{N\text{-melt}}$	21·8	22·8	40·5	20·4	25·5	29·5	19·7	27·9	29·0	18·2	24·9	20·1	31·4	20·5	27·5	24·7	21·2	22·7	27·4
$Yb_{N\text{-melt}}$	2·56	4·41	6·89	2·83	3·60	6·48	2·13	3·20	6·69	2·32	2·91	2·70	3·15	2·08	2·98	5·99	2·28	3·70	4·68
Sr/Y_{melt}	283	191	133	265	197	103	332	209	170	269	189	232	175	292	213	109	296	201	159
Y_{melt}	8·06	13·7	21·4	9·42	13·6	20·4	6·85	11·7	16·0	8·26	12·3	9·67	13·6	7·60	11·9	16·7	8·00	12·3	15·0
Mg_{melt}	56·6	52·8	47·5	57·5	53·6	46·7	55·7	48·8	46·6	57·4	52·3	57·6	51·8	55·0	51·0	46·5	54·2	48·7	46·6

HSC, hourglass sector core; PSC, prism sector core; R, rim.
bdl: below detection limit.
$Mg^{\#} = Mg/(Mg+FeT)\times100$; $\delta Eu = 2\times Eu_N/(Sm_N+Gd_N)$; N, chondrite normalized.
$Mg^{\#}$ of melt equilibrating with clinopyroxene phenocryst is calculated using $D_{Fe\text{-}Mg} = 0.28$.

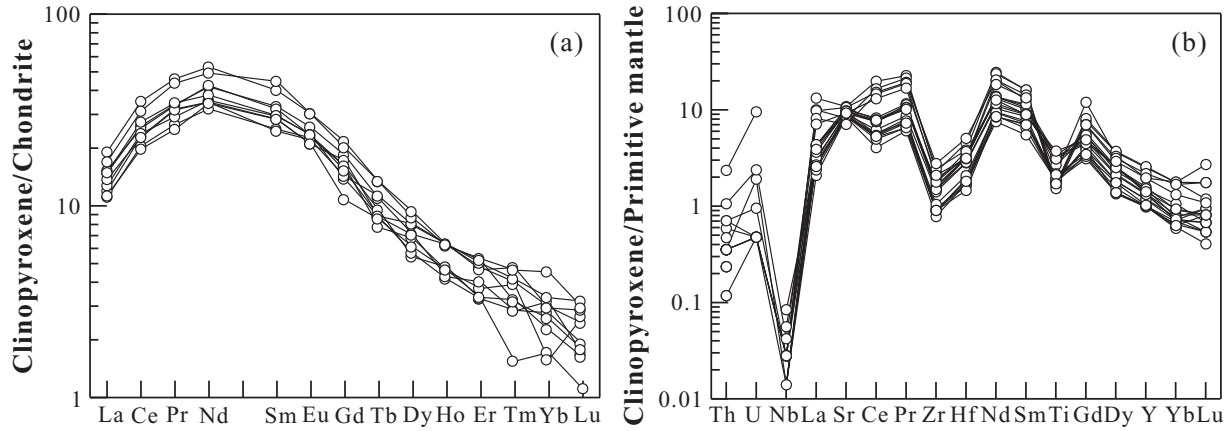

Fig. 12 (a) Chondrite-normalized REE patterns; and (b) primitive mantle-normalized multi-element diagrams for clinopyroxene phenocrysts in the Heishantou diorite. Normalization values are the same as Fig. 5.

element patterns between the cores and the rims (Fig. 12), and the calculated melt composition in equilibrium with clinopyroxene or amphibole phenocrysts are also similar to the whole-rock (Fig. 5a). This is in favor of a single parental magma but obviously argues against the model of melting of thickened lower crust triggered by mafic magma underplating. Alternatively, partial melting of a delaminated lower continental crust would be a reasonable genetic model for the primary high-$Mg^{\#}$ adakitic melt of the Heishantou diorites. Melting of delaminated mafic lower crust would likewise produce relatively low-$Mg^{\#}$ and high-SiO_2 melt originally (Atherton & Petford, 1993; Hou *et al.*, 2004; Huang *et al.*, 2009; Qian & Hermann, 2013). However, the melt will interact with mantle peridotite inevitably during its way up to the crust, and this will increase its concentrations of compatible elements (like Mg, Ni, Cr; Yogodzinski & Kelemen, 1998, Rapp *et al.*, 1999; Martin *et al.*, 2005). In this case, the originally high SiO_2 and low $Mg^{\#}$, Cr and Ni melts generated by partial melting of the delaminated lower crust will interact with asthenosphere during their ascent, resulting in low SiO_2 and high $Mg^{\#}$, Cr and Ni. The Sr–Nd isotopes of the Heishantou diorite samples are slightly more enriched than those of Permian basaltic volcanic rocks in the Nileke area but are more depleted than those of other Permian adakitic rocks formed by partial melting of thickened lower crust in the Tianshan orogenic belt (e.g. Chuanwulu complex; Huang *et al.*, 2012; Fig. 6a), which supports a hybrid source that involves continental crustal materials and mantle. Consistently, the zircon O isotopes of the Heishantou diorite samples are relatively homogeneous ($\delta^{18}O = 5{\cdot}4 - 6{\cdot}6$, except for three discrete zircons with $\delta^{18}O$ of $6{\cdot}9 - 7{\cdot}5$ probably due to crustal assimilation during magmatic evolution; Fig. 3b), but in the range between mantle ($5{\cdot}3‰ \pm 0{\cdot}3‰$; Valley *et al.*, 1998) and continental crustal materials ($8‰$ to $> 10‰$; Valley *et al.*, 2005).

Early Permian lower crust delamination in the Western Tianshan orogenic belt

Lower crustal delamination is a complex process involving initial lower crustal thickening, subsequent partial melting to form denser eclogite or garnet-bearing restite, and the final detachment of overthickened lower crust (Lustrino, 2005; Huang *et al.*, 2008). The hypothesis of lithosphere delamination is well established by numerical experiments and modeling based on rheological and physical properties of the lithosphere (Elkins-Tanton, 2007; Gogus & Ueda, 2018) and is also supported by geophysical and geological evidence at continental plate convergent zones (e.g. Tilmann *et al.*, 2003; Wang *et al.*, 2007a; Baratin *et al.*, 2016). Indeed, there are some clues on Early Permian delamination of the continental lithosphere in the Tianshan orogenic belt. For example, plenty of Permian mafic–ultramafic intrusions in the Eastern Tianshan–Beishan area were proposed as products from asthenosphere upwelling after lithosphere delamination (Tang *et al.*, 2011; Xue *et al.*, 2016). Late Paleozoic magmatism along the Awulale Mountains in the Yili Block changed from calc-alkaline (~311 Ma) to shoshonitic (294–251 Ma), which may be attributed to geodynamic transformation of the Western Tianshan from Late Carboniferous collision to Early Permian delamination of the lithospheric mantle (Yang *et al.*, 2012). Permian post-collisional magmatism and local low-pressure and high-temperature metamorphism in the Western Tianshan are attributed to delamination of the thickened continental lithosphere and upwelling of the asthenosphere (Han *et al.*, 2011). In the Kyrgyz South Tien Shan (west of the Chinese Tianshan Orogen), the coeval Early Permian granitoids (including I-type, shoshonitic and peraluminous) and alkaline intrusions were post-collisional magmatism most likely produced by delamination of lithospheric mantle (Konopelko *et al.*, 2018).

In the Nileke area, there are abundant adakitic rocks (*c.*278–307 Ma) that are slightly older than the

Table 6: EPMA major (wt %) and trace (ppm) elements concentrations of amphibole phenocrysts in the Heishantou diorite

Spot	#1	#2	#3	#4	#5	#6	#7	#8	#9	#10
EPMA major (wt %)										
SiO_2	41·02	41·61	41·26	41·64	41·16	42·28	41·85	40·55	41·46	41·28
TiO_2	1·77	1·56	1·64	1·58	1·65	2·06	2·20	1·91	1·82	1·52
Al_2O_3	13·50	13·45	13·07	12·85	13·60	12·47	12·51	14·07	13·14	13·65
FeO^T	8·95	8·24	8·92	8·41	8·86	9·28	9·49	9·81	9·69	8·49
MnO	0·05	0·10	0·06	0·05	0·08	0·10	0·09	0·09	0·09	0·07
MgO	15·71	15·74	16·09	15·89	15·57	15·40	15·28	14·68	15·43	15·56
CaO	11·87	11·76	11·85	12·00	12·01	11·66	11·57	11·90	11·80	11·75
Na_2O	2·82	2·94	2·88	2·85	2·76	2·82	3·07	2·56	2·66	2·89
K_2O	0·89	0·89	0·91	0·86	0·91	0·65	0·59	0·85	0·79	0·90
F	2·59	2·54	3·05	3·17	2·35	1·78	1·52	0·94	2·24	1·98
Cl	bdl	bdl	bdl	bdl	bdl	0·02	bdl	bdl	bdl	bdl
Total	99·26	99·24	99·91	99·49	99·22	98·55	98·19	97·37	99·14	98·48
$Mg^{\#}$	75·8	77·3	76·3	77·1	75·8	74·7	74·2	72·7	74·0	76·6
LA-ICP-MS trace (ppm)										
Sc	79·4	72·5	77·3	65·9	74·9	65·2	70·0	63·2	65·4	69·4
V	326	319	323	347	332	478	458	358	348	325
Cr	1111	2684	1365	4334	1293	188	231	12·1	21·7	2725
Co	62·4	64·8	63·1	62·9	62·2	73·5	71·4	67·2	64·2	62·1
Ni	743	855	747	1168	682	246	287	381	245	814
Rb	2·32	1·63	1·90	4·86	2·01	6·66	6·01	3·38	3·38	1·98
Sr	904	789	850	820	816	641	706	966	1024	765
Y	7·97	6·51	6·99	6·87	6·43	8·02	8·40	9·61	9·14	6·14
Zr	18·1	11·1	12·8	13·7	15·3	19·8	22·3	28·8	24·1	10·2
Nb	0·37	0·41	0·44	0·43	0·38	0·94	0·93	0·69	0·84	0·30
Ba	187	146	170	177	162	118	140	227	220	150
La	3·50	2·63	2·83	3·62	3·02	3·25	3·53	4·52	4·02	2·67
Ce	15·9	12·6	14·0	15·5	14·6	13·9	16·7	21·4	19·1	12·1
Pr	3·21	2·52	3·04	3·17	2·77	3·01	3·27	4·36	4·15	2·38
Nd	19·5	15·0	16·3	19·8	16·6	16·2	17·7	24·7	23·0	16·0
Sm	5·04	3·84	4·33	4·89	4·49	3·75	4·52	6·12	6·82	4·32
Eu	1·49	1·31	1·22	1·35	1·37	1·28	1·36	1·76	1·75	1·22
Gd	3·78	3·31	3·54	3·32	2·84	2·93	3·13	4·45	4·13	2·21
Tb	0·41	0·36	0·33	0·29	0·33	0·42	0·33	0·50	0·50	0·32
Dy	1·80	1·37	1·44	1·72	1·79	2·01	2·04	2·20	2·37	1·55
Ho	0·36	0·27	0·23	0·26	0·24	0·36	0·36	0·35	0·35	0·26
Er	0·79	0·54	0·54	0·61	0·66	0·77	0·83	0·88	0·86	0·55
Tm	0·10	0·04	0·07	0·10	0·07	0·12	0·11	0·12	0·08	0·08
Yb	0·51	0·29	0·47	0·27	0·54	0·50	0·56	0·77	0·44	0·38
Lu	0·06	0·03	0·05	0·07	0·04	0·07	0·08	0·07	0·05	0·04
Hf	1·00	0·64	0·69	0·48	0·75	0·99	0·99	1·33	1·44	0·53
Ta	0·02	0·01	0·01	0·02	bdl	0·02	0·05	0·02	0·05	0·03
Pb	0·69	0·76	0·90	1·47	0·72	1·64	2·23	1·00	1·52	0·70
Th	0·03	0·02	0·03	0·03	0·02	0·02	0·03	0·06	0·06	0·02
U	0·01	0·01	bdl	0·04	0·01	0·04	0·05	0·03	0·06	bdl
Sr/Y	113	121	122	119	127	80	84	100	112	125
La/Yb	6·9	9·0	6·0	13·5	5·6	6·5	6·3	5·9	9·2	6·9
D_{La}	0·090	0·090	0·089	0·083	0·096	0·094	0·134	0·121	0·089	0·115
D_{Ce}	0·154	0·154	0·152	0·143	0·164	0·160	0·231	0·208	0·152	0·195
D_{Pr}	0·242	0·242	0·237	0·225	0·257	0·250	0·365	0·328	0·237	0·306
D_{Nd}	0·350	0·350	0·342	0·327	0·369	0·360	0·529	0·475	0·340	0·441
D_{Sm}	0·552	0·552	0·534	0·520	0·576	0·564	0·835	0·748	0·529	0·692
D_{Eu}	0·623	0·623	0·601	0·589	0·647	0·635	0·943	0·843	0·595	0·781
D_{Gd}	0·674	0·674	0·647	0·639	0·696	0·685	1·017	0·909	0·641	0·843
D_{Tb}	0·698	0·698	0·667	0·664	0·717	0·708	1·050	0·938	0·661	0·873
D_{Dy}	0·694	0·694	0·660	0·661	0·708	0·702	1·038	0·927	0·654	0·866
D_{Ho}	0·666	0·666	0·630	0·635	0·675	0·672	0·991	0·885	0·625	0·830
D_{Er}	0·622	0·622	0·586	0·594	0·627	0·626	0·920	0·822	0·582	0·775
D_{Tm}	0·571	0·571	0·536	0·546	0·572	0·573	0·839	0·750	0·532	0·711
D_{Yb}	0·518	0·518	0·484	0·496	0·517	0·520	0·758	0·677	0·482	0·645
D_{Lu}	0·468	0·468	0·436	0·449	0·465	0·469	0·681	0·609	0·434	0·583
D_Y	0·678	0·678	0·642	0·646	0·689	0·684	1·010	0·902	0·637	0·845
D_{Sr}	0·420	0·405	0·405	0·395	0·420	0·395	0·413	0·420	0·451	0·411
ΔNNO	1·3	1·3	1·4	1·3	1·2	1·1	1·0	1·0	1·2	1·2
H_2O_{melt} (wt%)	5·2	5·4	4·7	5·0	5·5	5·4	5·3	6·3	5·5	5·6
$Mg_{\#melt}$	48·4	50·5	49·1	50·3	48·4	47·0	46·3	44·5	46·0	49·5

(continued)

Table 6:. Continued

Spot	#1	#2	#3	#4	#5	#6	#7	#8	#9	#10
$SiO_{2\ melt}$ (wt%)	53·0	53·7	53·0	55·1	53·6	57·8	56·5	54·3	55·6	53·5
$(La/Yb)_{N\text{-}melt}$	28·5	35·2	25·8	52·2	22·2	26·5	25·1	26·9	23·7	39·9
$Yb_{N\text{-}melt}$	5·74	3·55	5·58	3·05	6·11	3·87	4·90	4·69	7·01	3·83
Sr/Y_{melt}	183	192	194	208	207	204	184	189	189	240
Y_{melt}	11·8	10·1	10·8	9·97	9·40	7·94	9·31	9·65	11·4	10·4

$Mg^{\#} = Mg/(Mg+Fe^{T})\times 100$.
Amphibole-liquid partition coefficients for elements are calculated using mineral composition model established by Shimizu *et al.* (2017) (D_{REE}) and Humphreys *et al.* (2019) (D_Y and D_{Sr}).
Oxygen fugacity (ΔNNO) and water content (H_2O_{melt}) of melt equilibrating amphibole phenocryst are calculated using amphibole thermobarometor by Ridolfi *et al.* (2010).
$Mg^{\#}$ of melt equilibrating amphibole phenocryst is calculated using $D_{Fe\text{-}Mg} = 0{\cdot}30$.
SiO_2 of melt equilibrating amphibole phenocryst is calculated using amphibole chemometric equations by Zhang *et al.* (2017).
bdl: below detection limit.

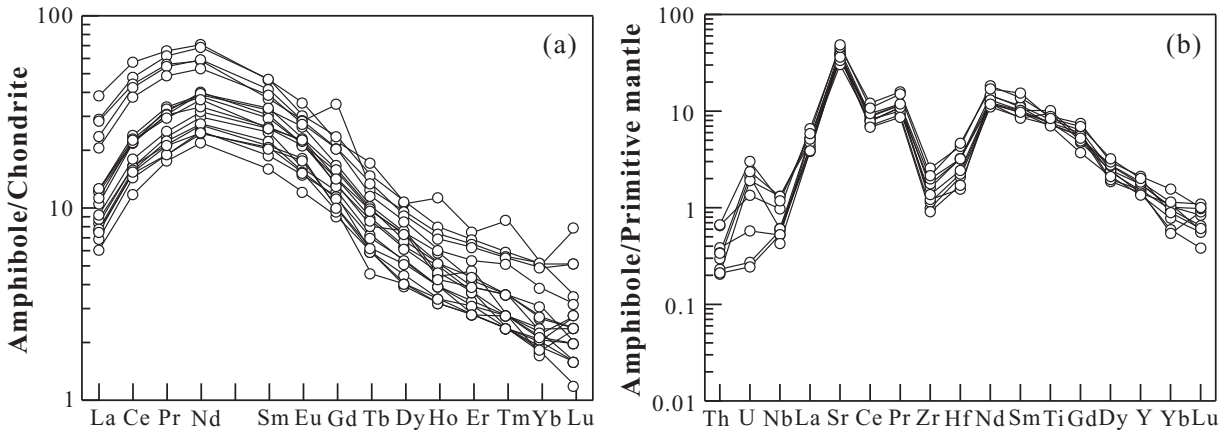

Fig. 13 (a) Chondrite-normalized REE patterns; and (b) primitive mantle-normalized multi-element diagrams for amphibole phenocrysts in the Heishantou diorite. Normalization values are the same as Fig. 5.

Heishantou diorite (Fig. 1c), such as the Yilanbasitao granodiorite porphyrites, Qunjigou dacites and Mosi zaote quartz albite porphyries (Zhao *et al.*, 2008; Tang *et al.*, 2017b; Li et al., 2019). These early adakitic rocks have high SiO_2 and low $Mg^{\#}$, Cr and Ni, which were suggested to be derived from partial melting of a thickened lower crust (Li *et al.*, 2019). The adakitic monzonite–syenite at 286 Ma in southwestern Tianshan is also likely derived from the melt of a thickened lower crust because of their enriched Sr–Nd–Hf isotopes (Huang *et al.*, 2012). This implies a thickened lower crust before the generation of the Heishantou adakitic rocks, probably due to the collision between the Junggar terrane, Yili block and Tarim craton during the Late Carboniferous. In addition, there are plenty of Early Permian magmatic rocks in the Tianshan orogenic belt, including bimodal volcanic rocks, mafic-ultramafic intrusions and A-type granites, which were proposed to be from the partial melting of asthenosphere upwelling (Mao *et al.*, 2005; Yang *et al.*, 2012; Xue *et al.*, 2016). Early Permian massive basaltic rocks are also widespread in the Nileke and adjacent area (Ye *et al.*, 2013; Li *et al.*, 2015b), suggesting a strong thermal perturbation that was probably related to mantle upwelling. Therefore, Late Carboniferous to Permian magmatic rocks in the Western Tianshan contain records of a combined previous partial melting of thickened lower crust and subsequent asthenosphere upwelling process that may have led to lithospheric delamination.

Due to collision between the Tarim craton, the Kazakhstan–Yili block and the Junggar terrane (Gao *et al.*, 2009; Han *et al.*, 2011; Xiao *et al.*, 2013), lower crust of the Tianshan Orogen was extruded and thickened and then transformed to eclogite assemblages at high pressures. The increasing density of the eclogitic lower crust caused a gravitational instability and detached with underlying lithospheric mantle into the asthenosphere. Consequently, post-collisional extension initially took place in the Early Permian, which might steepen the previous suture zones and cause backwards propagation of the thrusts within the lithosphere. These processes can provide channels for the emplacement of mafic magmas in the crust (Lustrino, 2005). The widespread bimodal magmatism verifies the existence of extensive rifts acting as the channels of mafic magma in the Tianshan Orogen (e.g. Shu *et al.*, 2011; Chen *et al.*, 2015). The involvement of high-temperature mafic magma might have triggered the partial melting of thickened lower crust (e.g. Zhao *et al.*, 2008; Huang *et al.*, 2012), which produced high-Si and low-$Mg^{\#}$ adakites and accelerated the detachment of 'eclogitic' lower crust by weakening the

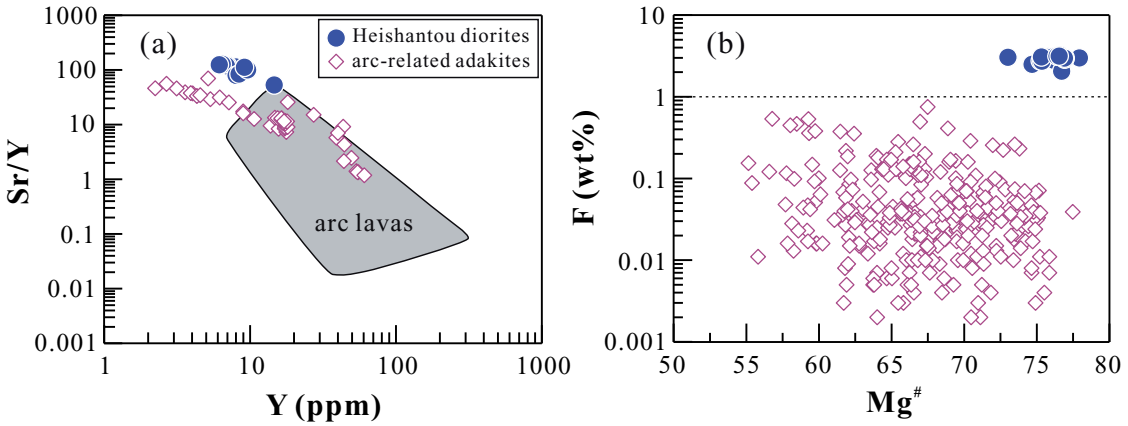

Fig. 14 (a) Sr/Y vs Y and (b) F vs $Mg^{\#}$ of amphibole phenocrysts in the Heishantou diorite. Amphibole compositional data of arc lavas are from Andean arc, Ryukyu arc and Taupo volcanic zone in New Zealand (Ewart & Taylor, 1969; Samaniego *et al.*, 2010; Chiaradia *et al.*, 2011; Tiepolo *et al.*, 2012; Johnson *et al.*, 2013). Amphibole Sr–Y data of arc-related adakites are from Adamello in Central Alps (Tiepolo *et al.*, 2011) and Solander and Little Solander Islands in New Zealand (Foley *et al.*, 2013). Amphibole F–$Mg^{\#}$ data of arc-related adakites are compiled from Rodriguez *et al.* (2007) and Rooney *et al.* (2011).

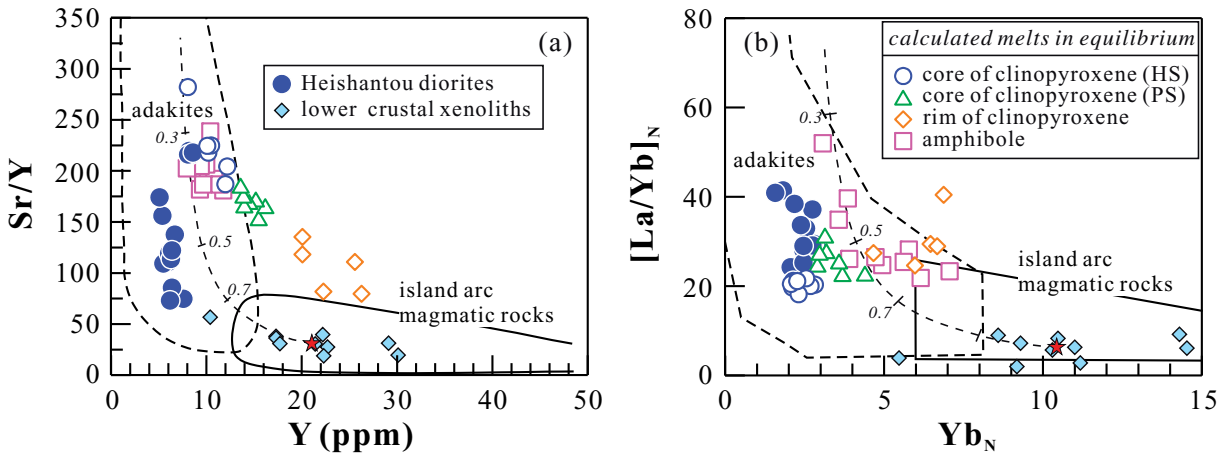

Fig. 15 (a) Sr/Y vs Y; and (b) $[La/Yb]_N$ vs Yb_N for the calculated melts in equilibrium with amphiboles and the cores and rims of clinopyroxenes in the Heishantou diorite. PS and HS are abbreviations for prism sector and hourglass sector, respectively. Dashed line represents partial melting curve for average composition of lower crustal xenoliths in Southwest Tianshan (Zheng *et al.*, 2006), leaving the residue of eclogite (0·7 clinopyroxene + 0·29 garnet + 0·01 rutile). Partition coefficients between minerals and silicate melt in lower crustal partial melting simulation are from Bédard (2006), Severs *et al.* (2009) and Qian & Hermann (2013). The fields of adakites and island arc magmatic rocks are the same as Fig. 4.

lithosphere keel and increasing the density contrast between the lower crust and underlying asthenospheric mantle. The partial melting of sinking lower crust and subsequent interaction with surrounding mantle materials might produce primary low SiO_2 but high-$Mg^{\#}$, Ni and Cr adakitic melts in Heishantou area (Fig. 16).

Effects of magmatic processes on adakitic signatures

Adakite was first used to describe the intermediate to felsic rock that is derived from partial melting of young subducted oceanic crust (Defant & Drummond, 1990). High Sr, Sr/Y and La/Yb (low HREE and Y) are the most widely used geochemical criteria for identifying an adakite (e.g. Moyen, 2009). Thus, many authors have termed rocks with similar chemical signatures (Sr > 400 ppm, Sr/Y > 40 and $[La/Yb]_N$ > 10) as adakites, adakitic rocks or adakite-like rocks, regardless of their origin. However, the geochemical features of adakite can change significantly through magmatic processes, such as assimilation and fractional crystallization (AFC) and mixing (Streck *et al.*, 2007; Chiaradia *et al.*, 2009; Castillo, 2012), which might be misleading for interpreting their petrogenesis and related tectonic settings. For example, previous studies reported plenty of Paleozoic adakitic/adakite-like rocks in the Tianshan Orogenic Belt (Fig. 1b–c), but few of them exactly meet the original chemical definition of adakites (Defant & Drummond, 1990; Martin *et al.*, 2005; Moyen, 2009), because their whole-rock composition might cover both non-adakite and adakite fields when using the geochemical

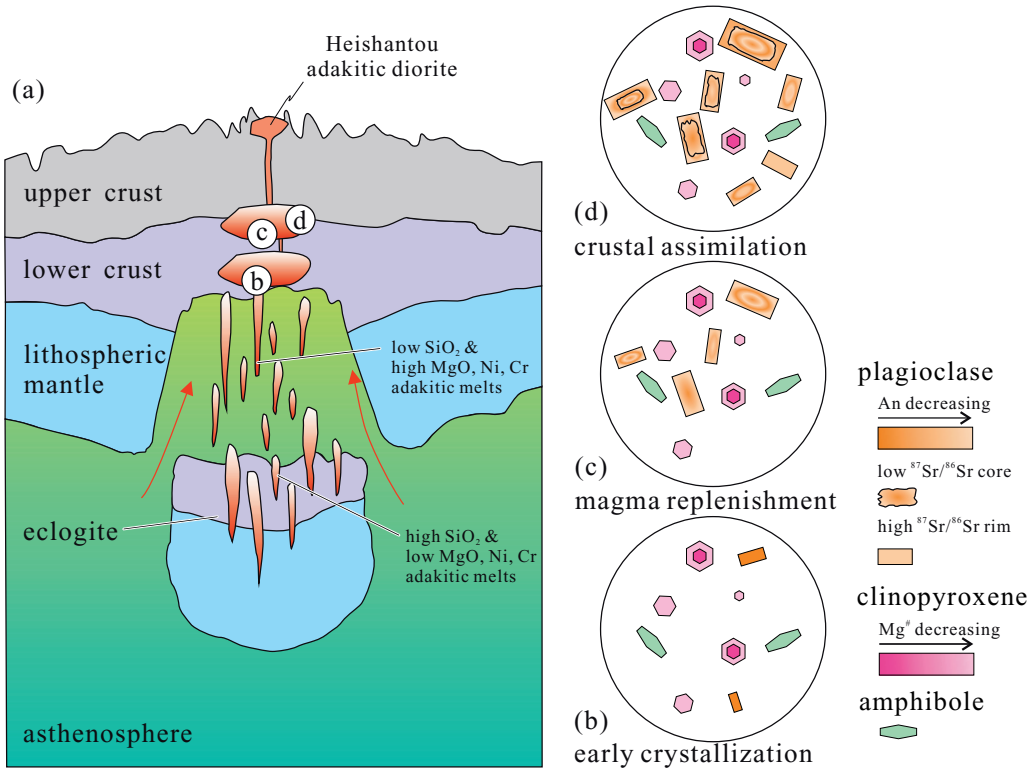

Fig. 16 Schematic illustration of the processes that generated the Heishantou adakitic rocks. Discussion is in the text. (a) The partial melting of sinking lower crust produced high SiO_2 low MgO adakitic melts, which became low SiO_2 high MgO when reacted with the surrounding asthenospheric mantle during their slow ascent to the crustal chamber. During the slow magma ascent, high-$Mg^{\#}$ clinopyroxene cores formed with sector-zoning, and early high-An plagioclases formed with high Sr contents and low $^{87}Sr/^{86}Sr$ ratios. (b) After the fractional crystallization of dominantly high-$Mg^{\#}$ clinopyroxene, amphibole and minor plagioclase, the melt became low $Mg^{\#}$, Sr/Y and high Y and formed the low-$Mg^{\#}$ rims of the clinopyroxenes. (c) As magma pooling in the crustal chamber, plagioclases were crystallizing with decreasing An content in the normal differentiation, but An contents may increase abruptly due to temporal magma replenishment. (d) During the residence of magma in the crustal chamber, the assimilation of surrounding crustal rock resulted in high $^{87}Sr/^{86}Sr$ such that the rims of the zoned plagioclase phenocrysts have relatively high $^{87}Sr/^{86}Sr$. The early-crystallized plagioclases were partially dissolved with resorption surfaces and then regrew with the highest Sr content due to the gradually strengthening crustal assimilation.

criterions such as the Sr/Y, Y, $[La/Yb]_N$ and Yb_N parameters (Fig. 4e and f). This suggests that these so-called adakitic/adakite-like rocks might have suffered intense magma chamber processes that would have erased the original signatures of primary magmas. However, such effects were always neglected or considered extremely insufficient in previous studies. Mineralogical investigations on the petrogenesis of the Heishantou diorite provide an example of how the typical characteristics of adakite, particularly Sr, Sr/Y and La/Yb, change with magmatic evolution.

The Heishantou diorite contains some felsic xenoliths and inherited zircons (299 ± 5 Ma; Table 1), suggesting crustal assimilation during magmatic evolution. Plagioclase phenocrysts show slightly lower initial $^{87}Sr/^{86}Sr$ ratios than the whole-rock values, which indicate the AFC process, because pure fractional crystallization cannot change Sr isotopes in subsolidus conditions. Consistently, $^{87}Sr/^{86}Sr$ values of zoned plagioclase phenocrysts increase in the rim (Fig. 8, 16d) and show negative correlations with An content (Fig. 7b). The zoned plagioclase phenocrysts show notably elevated Sr content in the rim (Fig. 8). The partition coefficient of Sr between plagioclase and silicate melts mostly depends on chemical composition of plagioclase (especially An; Blundy & Wood, 1991; Bindeman *et al.*, 1998). The An contents of cores and rims of plagioclase phenocrysts appear to overlap (Fig. 8), indicating overall similar D_{Sr}^{pl-liq} during the crystallization. Thus notably elevated Sr content in the rims of plagioclase phenocrysts would be attributed to high Sr in the final melts rather than induced by the change of partition coefficient.

The cores of plagioclase phenocrysts show two distinct trends in the diagrams of $^{87}Sr/^{86}Sr$ v s An and SrO (Fig. 7b and c). One trend is characterized by decreasing $^{87}Sr/^{86}Sr$ with increasing An and SrO, which is likely due to magma replenishment as evidenced by the abrupt increase of An content across the rounded and resorption boundary in zoned plagioclase phenocrysts (Fig. 8b). Thus, high Sr content in the plagioclases is likely formed in the less evolved magma. The other trend is characterized by relatively constant $^{87}Sr/^{86}Sr$ with decreasing An and SrO, corresponding to fractional crystallization. Plagioclase as the dominant carrier of Sr in the rock-forming minerals will extract Sr from the

melts during its fractional crystallization and result in low Sr in the residual melts, which may account for the generally positive correlation between SrO and An (Fig. 7a). Thus, magma replenishment and fractional crystallization have opposite effects on SrO concentrations in the Heishantou adakitic melts.

Because garnet is one of the most important carriers of Y and HREE, and amphibole also has higher partition coefficients for HREE and Y than for LREE and Sr (Dalpe & Baker, 2000; Hilyard *et al.*, 2000; Shimizu *et al.*, 2017), fractional crystallization of such minerals will efficiently increase the Sr/Y and La/Yb ratios of residual melts and strongly impact the adakitic features. Thus, adakitic melt can be produced from basaltic magma via high-pressure fractional crystallization of garnet or amphibole in the early evolution of an arc system (Castillo *et al.*, 1999; Macpherson *et al.*, 2006; Rodriguez *et al.*, 2007; Alonso-Perez *et al.*, 2009; Rooney *et al.*, 2011). As mentioned above, in the Heishantou diorites, notable amphiboles crystallized slightly later than the cores of clinopyroxene phenocrysts. Partition coefficients for Y and HREE between amphibole and silicate melts mainly depend on the SiO_2 content of the coexisting melt and gradually increase from < 1 to > 1 with increasing SiO_2 (Tiepolo *et al.*, 2000). According to the mineral composition model established by Shimizu *et al.* (2017), the partition coefficients for Y and HREE between amphibole and the early magma of the Heishantou diorite are roughly less than one (Table 6). In addition, both Y and HREE are incompatible elements but are more compatible than LREE also for clinopyroxene in basaltic-andesite systems (Norman *et al.*, 2005; Bédard 2014). Therefore, the effect of the fractionation of clinopyroxene and amphibole is to increase Y, HREE and La/Yb in the residual magma. As expected, the clinopyroxene phenocrysts in the Heishantou diorite samples show increasing Y, HREE and La/Yb from core to rim, consistent with the trend of magma evolution (Fig. 11b–d). Furthermore, Sr is more incompatible than Y for both clinopyroxene and amphibole in basaltic–andesitic magma (Green *et al.*, 1993; Norman *et al.*, 2005), suggesting that the fractionation of amphibole and clinopyroxene will increase Sr/Y in the residual melt (Rodriguez *et al.*, 2007; Rooney *et al.*, 2011; Castillo, 2012). However, the clinopyroxene phenocrysts in the Heishantou diorite samples show decreasing Sr/Y ratios with indistinctive Sr content between core and rim. This is apparently inconsistent with the effect of fractional crystallization of amphibole or clinopyroxene, but would be due to the dilution effect of early plagioclase fractionation (Fig. 16b). The change from no Eu anomaly in the cores of clinopyroxene phenocrysts to slightly negative Eu anomaly in the rims suggests small amount of plagioclase crystallization after the formation of clinopyroxene cores. Plagioclase in the studied samples is highly evolved with low An content (mostly 30–50%; Fig. 7a and b), but some cores with high An content ($>$ 60%; Fig. 7a) may have been generated in an early primitive melt. Because plagioclase has much lower distribution coefficients for REE (except for Eu) and Y than clinopyroxene and amphibole in the basaltic-andesite system (Dalpe & Baker, 2000; Norman *et al.*, 2005), its fractionation will lower the Sr concentration and Sr/Y ratio but may not change the La/Yb ratio in the residual melt. Therefore, early fractionation of clinopyroxene and amphibole with minor plagioclase would increase Y, Yb and La/Yb but decrease Sr/Y in the adakitic melts (Fig. 15).

In addition to the Sr, Y and REE content in adakites, $Mg^{\#}$, Cr and Ni are also widely used for ascertaining the local tectonic evolution (e.g. Kay & Kay, 2002; Wang *et al.*, 2007a; Huang *et al.*, 2009; Long *et al.*, 2015) and are differentiated greatly during magma evolution. Whole-rock $Mg^{\#}$ values and Cr, Ni content of the Heishantou diorite samples are relatively low and plot in the field of 'thickened lower crust-derived adakitic rocks' on the diagram of SiO_2 vs $Mg^{\#}$, Cr or Ni (Fig. 4c and d). However, primitive magma in equilibrium with high-$Mg^{\#}$ cores of zoned clinopyroxene phenocrysts has much higher $Mg^{\#}$ and Cr and likely plots into the field of 'delaminated lower crust-derived adakitic rocks'. Fractional crystallization of clinopyroxene and amphibole can lower $Mg^{\#}$, Cr and Ni in the residual melt, which is shown by decreases of $Mg^{\#}$, Cr and Ni from the cores to rims in the zoned clinopyroxene phenocrysts (Fig. 11e and f).

Collectively, whole-rock geochemistry can change and greatly differ from primitive melt during magma evolution and thus needs to be carefully examined to understand the primitive magma origins (e.g. Muntener & Ulmer, 2006; Muntener *et al.*, 2008; Alonso-Perez *et al.*, 2009; Moyen, 2009). The zoning textures in some minerals can record the complicated processes of magma evolution (Davidson *et al.*, 2007; Streck *et al.*, 2007; Foley *et al.*, 2013; Ustunisik *et al.*, 2014). *In situ* mineral compositions, such as MgO, Ni and Cr in clinopyroxene and amphibole, provide critical evidence in addition to whole-rock geochemistry for identifying the primary features of adakitic rocks (Streck *et al.*, 2007; Sato *et al.*, 2013). Plagioclase, as the most important Sr-bearing mineral, plays an important role in the Sr content and Sr/Y ratios of the adakitic rocks. *In situ* Sr isotopes of plagioclase are widely used to decipher the magmatic processes such as magma mixing, recharging, contamination, and residence time in the magma chamber (e.g. Davidson *et al.*, 2001, 2007; Ramos *et al.*, 2005; Charlier *et al.*, 2008). Petrogenesis and related tectonics of the adakitic rocks should be deciphered based on integrated investigation of both whole-rock geochemistry and *in situ* elemental and isotopic compositions of the minerals.

CONCLUSION

The Heishantou diorite in the Western Tianshan orogenic belt was formed at the end of the Early Permian (271 Ma). The rocks have high Sr and low Y and HREE with high Sr/Y and La/Yb ratios, resembling a typical

adakite, but they are also characterized by low $Mg^{\#}$, Cr and Ni. The cores of zoned clinopyroxene phenocrysts have high $Mg^{\#}$, Cr, Ni and Sr, but low Y and HREE with high Sr/Y and La/Yb ratios, which suggest an initially high-$Mg^{\#}$ feature of the adakitic magma.

The Heishantou diorite was derived from the partial melting of delaminated lower crust, and the interaction of the lower crustal partial melt with asthenosphere resulted in low SiO_2 and high $Mg^{\#}$, Cr and Ni of primary adakitic melts. The Western Tianshan orogenic belt has experienced previous partial melting of a thickened lower crust and subsequent asthenospheric upwelling processes that resulted in lithospheric delamination.

The characteristic features of adakite, such as Sr content and Sr/Y and La/Yb ratios, can be highly altered due to magmatic processes and should be deciphered based on an integrated investigation of both whole-rock geochemistry and *in situ* elemental and isotopic mineral compositions of clinopyroxene, amphibole and plagioclase.

ACKNOWLEDGEMENTS

The data used in this work are listed in supplementary data. We thank Le Zhang and Jinglong Ma for their assistance with whole-rock Sr–Nd–Hf isotopic, and plagioclase Sr isotopic analyses, Zhaochu Hu for the help with *in situ* mineral trace elemental analyses, and Xiaoping Xia, Yin Liu and Xianglin Tu for their help with zircon Cameca U–Pb dating and O isotopic analyses, and whole-rock elemental analyses. We are grateful to Elburg Marlina, Pat Castillo, Maureen Feineman and two anonymous reviewers for their careful reviews and constructive comments, which greatly improved the manuscript, and thank Prof. Georg Zellmer for his editorial handling of this paper. This is contribution No. IS-2981 from GIGCAS.

FUNDING

This research is funded by the Strategic Priority Research Program (B) of the Chinese Academy of Sciences [XDB18020204] and the National Natural Science Foundation of China [NSFC Projects 41703033, 41625007].

SUPPLEMENTARY DATA

Supplementary data are available at *Journal of Petrology* online.

REFERENCES

Allen, M., Windley, B. & Zhang, C. (1993). Palaeozoic collisional tectonics and magmatism of the Chinese Tienshan. *Tectonophysics* **220**, 89–115.

Alonso-Perez, R., Müntener, O. & Ulmer, P. (2009). Igneous garnet and amphibole fractionation in the roots of island arcs: experimental constraints on andesitic liquids. *Contributions to Mineralogy and Petrology* **157**, 541–558.

Atherton, M. P. & Petford, N. (1993). Generation of sodium-rich magmas from newly underplated basaltic crust. *Nature* **362**, 144–146.

Baratin, L. M., Mazzotti, S., Chery, J., Vernant, P., Tahayt, A. & Mourabit, T. (2016). Incipient mantle delamination, active tectonics and crustal thickening in Northern Morocco: Insights from gravity data and numerical modeling. *Earth and Planetary Science Letters* **454**, 113–120.

Bédard, J. H. (2006). Trace element partitioning in plagioclase feldspar. *Geochimica Et Cosmochimica Acta* **70**, 3717–3742.

Bédard, J. H. (2014). Parameterizations of calcic clinopyroxene Melt trace element partition coefficients. *Geochemistry, Geophysics, Geosystems* **15**, 303–336.

Bindeman, I. N., Davis, A. M. & Drake, M. J. (1998). Ion microprobe study of plagioclase-basalt partition experiments at natural concentration levels of trace elements. *Geochimica Et Cosmochimica Acta* **62**, 1175–1193.

BGMRXUAR (Bureau of Geology and Mineral Resources of Xinjiang Uygur Autonomous Region). (1979). *Regional Geology of Xinjiang Autonomous Region. Geological Memoirs (Map No. 51, Scale 1:200000)*. Beijing, Geological Publishing House (in Chinese).

Blundy, J. D. & Wood, B. J. (1991). Crystal-chemical controls on the partitioning of sr and ba between plagioclase feldspar, silicate melts, and hydrothermal solutions. *Geochimica Et Cosmochimica Acta* **55**, 193–209.

Bourdon, E., Eissen, J. P., Monzier, M., Robin, C., Martin, H., Cotten, J. & Hall, M. L. (2002). Adakite-like lavas from Antisana volcano (Ecuador): Evidence for slab melt metasomatism beneath the Andean Northern volcanic zone. *Journal of Petrology* **43**, 199–217.

Castillo, P. R. (2012). Adakite petrogenesis. *Lithos* **134-135**, 304–316.

Castillo, P. R., Janney, P. E. & Solidum, R. U. (1999). Petrology and geochemistry of Camiguin Island, southern Philippines: insights to the source of adakites and other lavas in a complex arc setting. *Contributions to Mineralogy and Petrology* **134**, 33–51.

Charlier, B. L. A., Wilson, C. J. N. & Davidson, J. P. (2008). Rapid open-system assembly of a large silicic magma body: time-resolved evidence from cored plagioclase crystals in the Oruanui eruption deposits, New Zealand. *Contributions to Mineralogy and Petrology* **156**, 799–813.

Chauvel, C., Lewin, E., Carpentier, M., Arndt, N. T. & Marini, J. C. (2008). Role of recycled oceanic basalt and sediment in generating the Hf–Nd mantle array. *Nature Geoscience* **1**, 64–67.

Chen, B., Jahn, B. M. & Suzuki, K. (2013). Petrological and Nd-Sr-Os isotopic constraints on the origin of high-Mg adakitic rocks from the North China Craton: Tectonic implications. *Geology* **41**, 91–94.

Chen, D. L., Liu, L., Che, Z. C. & Luo, J. H. (2001). Geochemical characteristis and tectonic implication of Carboniferous volcanites in the Luotuogou area of Middle Tianshan. *Acta Petrologica Sinica* **17**, 378–384 [in Chinese with English abstract].

Chen, G. W., Deng, T., Liu, R., Xia, H. & Liu, Q. (2015). Geochemistry of bimodal volcanic rocks in Permian Taerdetao Formation in Awulale area of western Tianshan, Xinjiang. *Acta Petrologica Sinica* **31**, 105–118 [in Chinese with English abstract].

Chiaradia, M., Muntener, O., Beate, B. & Fontignie, D. (2009). Adakite-like volcanism of Ecuador: lower crust magmatic evolution and recycling. *Contributions to Mineralogy and Petrology* **158**, 563–588.

Chiaradia, M., Othmar, M. & Bernardo, B. (2011). Enriched basaltic andesites from mid-crustal fractional crystallization,

recharge, and assimilation (Pilavo Volcano, Western Cordillera of Ecuador). *Journal of Petrology* **52**, 1107–1141.
Coleman, R. G. (1989). Continental growth of Northwest China. *Tectonics* **8**, 621–635.
Dalpe, C. & Baker, D. R. (2000). Experimental investigation of large-ion-lithophile-element-, high-field-strength-element- and rare-earth-element-partitioning between calcic amphibole and basaltic melt: the effects of pressure and oxygen fugacity. *Contributions to Mineralogy and Petrology* **140**, 233–250.
Davidson, J., Tepley, F., Palacz, Z. & Meffan-Main, S. (2001). Magma recharge, contamination and residence times revealed by in situ laser ablation isotopic analysis of feldspar in volcanic rocks. *Earth and Planetary Science Letters* **184**, 427–442.
Davidson, J. P., Morgan, D. J., Charlier, B. L. A., Harlou, R. & Hora, J. M. (2007). Microsampling and isotopic analysis of igneous rocks: Implications for the study of magmatic systems. *Annual Review of Earth and Planetary Sciences* **35**, 273–311.
Defant, M. J. & Drummond, M. S. (1990). Derivation of some modern arc magmas by melting of young subducted lithosphere. *Nature* **347**, 662–665.
Ding, Z. X., Xue, C. J., Zhao, X. B., Yan, Y. H., Yaxiaer, Y., Feng, B., Luo, H., Zu, B., Zhang, Q. & Dai, Z. J. (2014). Geochronology, geochemistry and petrogenesis of the Early Permian rhyolite and its constraints on the lithosphere deep processes of the Western Awulale, Xinjiang. *Earth Science Frontiers* **21**, 196–210 [in Chinese with English abstract].
Drummond, M. S., Defant, M. J. & Kepezhinskas, P. K. (1996). Petrogenesis of slab-derived trondhjemite-tonalite-dacite/adakite magmas. *Earth and Environmental Science Transactions of the Royal Society of Edinburgh* **87**, 205–215.
Du, L., Zhang, Y. Y., Huang, Z. Y., Li, X. P., Yuan, C., Wu, B. & Long, X. P. (2019). Devonian to carboniferous tectonic evolution of the Kangguer Ocean in the Eastern Tianshan, NW China: Insights from three episodes of granitoids. *Lithos* 350–351, 105243.
Elburg, M., Vroon, P., van der Wagt, B. & Tchalikian, A. (2005). Sr and Pb isotopic composition of five USGS glasses (BHVO-2G, BIR-1G, BCR-2G, TB-1G, NKT-1G). *Chemical Geology* **223**, 196–207.
Elkins-Tanton, L. T. (2007). Continental magmatism, volatile recycling, and a heterogeneous mantle caused by lithospheric gravitational instabilities. *Journal of Geophysical Research* **112**, B03405.
Ewart, A. & Taylor, S. R. (1969). Trace element geochemistry of the rhyolitic volcanic rocks, Central North Island. *Contributions to Mineralogy and Petrology* **22**, 127–146.
Foley, F. V., Pearson, N. J., Rushmer, T., Turner, S. & Adam, J. (2013). Magmatic evolution and magma mixing of quaternary adakites at solander and little Solander Islands, New Zealand. *Journal of Petrology* **54**, 703–744.
Gao, J., Klemd, R., Qian, Q., Zhang, X., Li, J. L., Jiang, T. & Yang, Y. Q. (2011). The collision between the Yili and Tarim blocks of the Southwestern Altaids: Geochemical and age constraints of a leucogranite dike crosscutting the HP-LT metamorphic belt in the Chinese Tianshan Orogen. *Tectonophysics* **499**, 118–131.
Gao, J., Long, L. L., Klemd, R., Qian, Q., Liu, D. Y., Xiong, X. M., Su, W., Liu, W., Wang, Y. T. & Yang, F. Q. (2009). Tectonic evolution of the South Tianshan orogen and adjacent regions, NW China: geochemical and age constraints of granitoid rocks. *International Journal of Earth Sciences* **98**, 1221–1238.
Gao, Y. F., Hou, Z. Q., Kamber, B. S., Wei, R. H., Meng, X. J. & Zhao, R. S. (2007). Adakite-like porphyries from the southern Tibetan continental collision zones: evidence for slab melt metasomatism. *Contributions to Mineralogy and Petrology* **153**, 105–120.
Ge, S. S., Zhai, M. G., Safonova, I., Li, D. P., Zhu, X. Y., Zuo, P. F. & Shan, H. X. (2015). Whole-rock geochemistry and Sr–Nd-Pb isotope systematics of the Late Carboniferous volcanic rocks of the Awulale metallogenic belt in the western Tianshan Mountains (NW China). *Lithos* **228-229**, 62–77.
Green, T. H., Adam, J. & Site, S. H. (1993). Proton microprobe determined trace element partition coefficients between pargasite, augite and silicate or carbonatitic melts. *EOS. Transactions of the American Geophysical Union* **74**, 340.
Gogus, O. H. & Ueda, K. (2018). Peeling back the lithosphere: Controlling parameters, surface expressions and the future directions in delamination modeling. *Journal of Geodynamics* **117**, 21–40.
Gou, L. L., Zhang, L. F., Tao, R. B. & Du, J. X. (2012). A geochemical study of syn-subduction and post-collisional granitoids at Muzhaerte River in the Southwest Tianshan UHP belt, NW China. *Lithos* **136-139**, 201–224.
Han, B. F., He, G. Q., Wang, X. C. & Guo, Z. J. (2011). Late Carboniferous collision between the Tarim and Kazakhstan-Yili terranes in the western segment of the South Tian Shan Orogen, Central Asia, and implications for the Northern Xinjiang, western China. *Earth-Science Reviews* **109**, 74–93.
Han, C. M., Xiao, W. J., Zhao, G., Mao, J. W., Yang, J. M., Wang, Z. L., Yan, Z. & Mao, Q. Q. (2006). Geological characteristics and genesis of the Tuwu porphyry copper deposit, Hami, Xinjiang, Central Asia. *Ore Geology Reviews* **29**, 77–94.
Han, Y. G., Zhao, G. C., Cawood, P. A., Sun, M., Liu, Q. & Yao, J. H. (2019). Plume-modified collision orogeny: The Tarim-western Tianshan example in Central Asia. *Geology* **47**, 1001–1005.
He, J. W., Zhang, Y. Z., Wang, Y. J., Qian, X. & Sun, L. H. (2018). Late Paleozoic post-collisional setting of the North Tianshan, NW China: New insights from geochronology, geochemistry and Sr–Nd isotopic compositions of the Permian Nileke volcanic rocks. *Lithos* **318-319**, 314–325.
He, P. L., Huang, X. L., Xu, Y. G., Li, H. Y., Wang, X. & Li, W. X. (2016). Plume-orogenic lithosphere interaction recorded in the Haladala layered intrusion in the Southwest Tianshan Orogen. *Journal of Geophysical Research: Solid Earth* **121**, 1525–1545.
Hilyard, M., Nielsen, R. L., Beard, J. S., Patino-Douce, A. & Blencoe, J. (2000). Experimental determination of the partitioning behavior of rare earth and high field strength elements between pargasitic amphibole and natural silicate melts. *Geochimica Et Cosmochimica Acta* **64**, 1103–1120.
Hou, Z. Q., Gao, Y. F., Qu, X. M., Rui, Z. Y. & Mo, X. X. (2004). Origin of adakitic intrusives generated during mid-Miocene east-west extension in southern Tibet. *Earth and Planetary Science Letters* **220**, 139–155.
Huang, F., Li, S. G., Dong, F., He, Y. S. & Chen, F. K. (2008). High-Mg adakitic rocks in the Dabie orogen, central China: Implications for foundering mechanism of lower continental crust. *Chemical Geology* **255**, 1–13.
Huang, H., Zhang, Z., Kusky, T., Zhang, D., Hou, T., Liu, J. & Zhao, Z. (2012). Geochronology and geochemistry of the Chuanwulu complex in the South Tianshan, western Xinjiang, NW China: Implications for petrogenesis and Phanerozoic continental growth. *Lithos* **140-141**, 66–85.
Huang, X. L., Xu, Y. G., Lan, J. B., Yang, Q. J. & Luo, Z. Y. (2009). Neoproterozoic adakitic rocks from Mopanshan in the western Yangtze Craton: Partial melts of a thickened lower crust. *Lithos* **112**, 367–381.

Humphreys, M. C. S., Cooper, G. F., Zhang, J., Loewen, M., Kent, A. J. R., Macpherson, C. G. & Davidson, J. P. (2019). Unravelling the complexity of magma plumbing at Mount St. Helens: a new trace element partitioning scheme for amphibole. *Contributions to Mineralogy and Petrology* **174**, 9.

Jochum, K. P., Pfander, J., Snow, J. E. & Hofmann, A. W. (1997). Nb/Ta in mantle and crust. *EOS. Transactions of the American Geophysical Union* **78**, 804.

Johnson, E. R., Kamenetsky, V. S. & McPhie, J. (2013). The behavior of metals (Pb, Zn, As, Mo, Cu) during crystallization and degassing of rhyolites from the Okataina Volcanic Center, Taupo Volcanic Zone, New Zealand. *Journal of Petrology* **54**, 1641–1659.

Kay, R. W. & Kay, S. M. (2002). Andean adakites: three ways to make them. *Acta Petrologica Sinica* **18**, 303–311.

Kay, S. M., Ramos, V. A. & Marquez, M. (1993). Evidence in Cerro-Pampa volcanic-rocks for slab-melting prior to ridge-trench collision in southern South-America. *The Journal of Geology* **101**, 703–714.

Kimura, J. I., Takahashi, T. & Chang, Q. (2013). A new analytical bias correction for in situ Sr isotope analysis of plagioclase crystals using laser-ablation multiple-collector inductively coupled plasma mass spectrometry. *Journal of Analytical Atomic Spectrometry* **28**, 945–957.

Kinzler, R. J. (1997). Melting of mantle peridotite at pressures approaching the spinel to garnet transition: Application to mid-ocean ridge basalt petrogenesis. *Journal of Geophysical Research: Solid Earth* **102**, 853–874.

Konopelko, D., Wilde, S. A., Seltmann, R., Romer, R. L. & Biske, Y. S. (2018). Early Permian intrusions of the Alai range: Understanding tectonic settings of Hercynian post-collisional magmatism in the South Tien Shan, Kyrgyzstan. *Lithos* **302-303**, 405–420.

Li, L., Xiong, X. L. & Liu, X. C. (2017). Nb/Ta fractionation by amphibole in hydrous basaltic systems: Implications for arc magma evolution and continental crust formation. *Journal of Petrology* **58**, 3–28.

Li, N. B., Niu, H. C., Shan, Q., Jiang, Y. H., Zeng, L. J., Yang, W. B. & Pei, Z. (2013a). Zircon U–Pb geochronology and geochemistry of post-collisional granitic porphyry from Yuantoushan, Nileke, Xinjiang. *Acta Petrologica Sinica* **29**, 3402–3412 [in Chinese with English abstract].

Li, N. B., Niu, H. C., Shan, Q. & Yang, W. B. (2015a). Two episodes of Late Paleozoic A-type magmatism in the Qunjisayi area, western Tianshan: Petrogenesis and tectonic implications. *Journal of Asian Earth Sciences* **113**, 238–253.

Li, N. B., Niu, H. C., Yang, W. B., Lai, C. K. & Zhao, Z. H. (2019). Orogenic root delamination induced by eclogitization of thickened lower crust in the Chinese Western Tianshan: constraints from adakites. *Journal of Geophysical Research: Solid Earth* **124**, 11089–11104.

Li, N. B., Niu, H. C., Zhang, X. C., Zeng, Q. S., Shan, Q., Li, C. Y., Yan, S. & Yang, W. B. (2015b). Age, petrogenesis and tectonic significance of the ferrobasalts in the Chagangnuoer iron deposit, western Tianshan. *International Geology Review* **57**, 1218–1238.

Li, X. H., Tang, G. Q., Gong, B., Yang, Y. H., Hou, K. J., Hu, Z. C., Li, Q. L., Liu, Y. & Li, W. X. (2013b). Qinghu zircon: A working reference for microbeam analysis of U–Pb age and Hf and O isotopes. *Chinese Science Bulletin* **58**, 4647–4654. [

Lin, L., Qian, Q., Wang, Y. L., Gao, J., Jiang, T. & Liu, X. (2015). Gabbroic pluton in the Dahalajunshan Formation volcanic rocks from northern Zhaosu, western Tianshan: Age, geochemistry and geological implications. *Acta Petrologica Sinica* **31**, 1749–1760 [in Chinese with English abstract].

Liu, H. Q., Xu, Y. G., Wei, G. J., Wei, J. X., Yang, F., Chen, X. Y., Liu, L. & Wei, X. (2016). B isotopes of Carbon iferous-Permian volcanic rocks in the Tuha basin mirror a transition from subduction to intraplate setting in Central Asian Orogenic Belt. *Journal of Geophysical Research: Solid Earth* **121**, 7946–7964.

Liu, X., Qian, Q., Su, W. & Li, J. L. (2012). Pluton from Muhanbasitao in the western of Awulale, Western Tianshan: Geochemistry, geochronology and geological implications. *Acta Petrologica Sinica* **28**, 2401–2413 [in Chinese with English abstract].

Liu, Y. S., Hu, Z. C., Gao, S., Gunther, D., Xu, J., Gao, C. G. & Chen, H. H. (2008). In situ analysis of major and trace elements of anhydrous minerals by LA-ICP-MS without applying an internal standard. *Chemical Geology* **257**, 34–43.

Long, L. L., Gao, J., Klemd, R., Beier, C., Qian, Q., Zhang, X., Wang, J. B. & Jiang, T. (2011). Geochemical and geochronological studies of granitoid rocks from the Western Tianshan Orogen: Implications for continental growth in the southwestern Central Asian Orogenic Belt. *Lithos* **126**, 321–340.

Long, X. P., Wilde, S. A., Wang, Q., Yuan, C., Wang, X.-C., Li, J., Jiang, Z. Q. & Dan, W. (2015). Partial melting of thickened continental crust in central Tibet: Evidence from geochemistry and geochronology of Eocene adakitic rhyolites in the northern Qiangtang Terrane. *Earth and Planetary Science Letters* **414**, 30–44.

Long, X. P., Wu, B., Sun, M., Yuan, C., Xiao, W. J. & Zuo, R. (2020). Geochronology and geochemistry of Late Carboniferous dykes in the Aqishan-Yamansu belt, eastern Tianshan: Evidence for a post-collisional slab breakoff. *Geoscience Frontiers* **11**, 347–362.

Luo, Y., Shan, Q., Zeng, Q. S., Li, N. B., Jiang, Y. H. & Zeng, L. J. (2013). Geochemistry of Permian potassic mafic volcanic rocks in western Awulale Mountains. *Geochimica* **42**, 544–556 [in Chinese with English abstract].

Lustrino, M. (2005). How the delamination and detachment of lower crust can influence basaltic magmatism. *Earth-Science Reviews* **72**, 21–38.

Ma, Q., Zheng, J. P., Xu, Y. G., Griffin, W. L. & Zhang, R. S. (2015). Are continental "adakites" derived from thickened or foundered lower crust? *Earth and Planetary Science Letters* **419**, 125–133.

Ma, Z. P., Xia, L. Q., Xu, X. Y., Xia, Z. C., Li, X. M. & Wang, L. S. (2008). Geochemical characteristics and petrogenesis of the Early Paleozoic igneous rocks from Bayinbuluke, Southern Tianshan. *Acta Petrologica Sinica* **24**, 2289–2300 [in Chinese with English abstract].

Macpherson, C. G., Dreher, S. T. & Thirlwall, M. F. (2006). Adakites without slab melting: High pressure differentiation of island arc magma, Mindanao, the Philippines. *Earth and Planetary Science Letters* **243**, 581–593.

Mao, J. W., Goldfarb, R. J., Wang, Y. T., Hart, C. J., Wang, Z. L. & Yang, J. M. (2005). Late Paleozoic base and precious metal deposits, East Tianshan, Xinjiang, China. *Episodes* **28**, 23–36.

Martin, H. (1999). Adakitic magmas: modern analogues of Archaean granitoids. *Lithos* **46**, 411–429.

Martin, H., Smithies, R. H., Rapp, R., Moyen, J. F. & Champion, D. (2005). An overview of adakite, tonalite-trondhjemite-granodiorite (TTG), and sanukitoid: relationships and some implications for crustal evolution. *Lithos* **79**, 1–24.

Mollo, S. & Hammer, J. (2017). Dynamic crystallization in magmas. *EMU Notes Mineral* **16**, 373–418.

Moyen, J. F. (2009). High Sr/Y and La/Yb ratios: The meaning of the "adakitic signature. *Lithos* **112**, 556–574.

Muntener, O. & Ulmer, P. (2006). Experimentally derived high-pressure cumulates from hydrous arc magmas and consequences for the seismic velocity structure of lower arc crust. *Geophysical Research Letters* **33**, L21308.

Muntener, O., Ulmer, P. & Perez, R. A. (2008). Role of garnet and amphibole fractionation in the genesis of high Mg# granitoids. *Geochimica Et Cosmochimica Acta* **72**, A665–A665.

Nandedkar, R. H., Ulmer, P. & Müntener, O. (2014). Fractional crystallization of primitive hydrous arc magmas: an experimental study at 0.7 GPa. *Contributions to Mineralogy and Petrology* **167**, 1015–1107.

Norman, M., Garcia, M. O. & Pietruszka, A. J. (2005). Trace-element distribution coefficients for pyroxenes, plagioclase, and olivine in evolved tholefites from the 1955 eruption of Kilauea Volcano, Hawai'i, and petrogenesis of differentiated rift-zone lavas. *American Mineralogist* **90**, 888–899.

Pearce, J. A. (2014). Immobile element fingerprinting of ophiolites. *Elements* **10**, 101–108.

Peccerillo, A. & Taylor, S. R. (1976). Geochemistry of eocene calc-alkaline volcanic-rocks from Kastamonu Area, Northern Turkey. *Contributions to Mineralogy and Petrology* **58**, 63–81.

Pouchou, J. L. & Pichoir, F. (1991). Quantitative-analysis of homogeneous or stratified microvolumes applying the model pap. *Electron Probe Quantitation* 31–75.

Putirka, K. D. (2008). Thermometers and barometers for volcanic systems. *Minerals, Inclusions and Volcanic Processes* **69**, 61–120.

Qian, Q., Gao, J., Klemd, R., He, G. Q., Song, B. A., Liu, D. Y. & Xu, R. H. (2009). Early Paleozoic tectonic evolution of the Chinese South Tianshan Orogen: constraints from SHRIMP zircon U–Pb geochronology and geochemistry of basaltic and dioritic rocks from Xiate, NW China. *International Journal of Earth Sciences* **98**, 551–569.

Qian, Q., Gao, J., Xiong, X. M., Long, L. L. & Huang, D. Z. (2006). Petrogenesis and tectonic settings of Carboniferous volcanic rocks from north Zhaosu, western Tianshan Mountains: constraints from petrology and geochemistry. *Acta Petrologica Sinica* **22**, 1307–1323 [in Chinese with English abstract].

Qian, Q. & Hermann, J. (2013). Partial melting of lower crust at 10-15 kbar: constraints on adakite and TTG formation. *Contributions to Mineralogy and Petrology* **165**, 1195–1224.

Qin, K. Z., Su, B. X., Sakyi, P. A., Tang, D. M., Li, X. H., Sun, H., Xiao, Q. H. & Liu, P. P. (2011). SIMS zircon U–Pb geochronology and Sr–Nd isotopes of Ni-Cu-bearing mafic-ultramafic intrusions in Eastern Tianshan and Beishan in correlation with flood basalts in Tarim basin (NW China): constraints on a ca. 280 ma mantle plume. *American Journal of Science* **311**, 237–260.

Ramos, F. C., Wolff, J. A. & Tollstrup, D. L. (2005). Sr isotope disequilibrium in Columbia River flood basalts: Evidence for rapid shallow-level open-system processes. *Geology* **33**, 457–460.

Rapp, R. P., Shimizu, N., Norman, M. D. & Applegate, G. S. (1999). Reaction between slab-derived melts and peridotite in the mantle wedge: experimental constraints at 3.8 GPa. *Chemical Geology* **160**, 335–356.

Ridolfi, F., Renzulli, A. & Puerini, M. (2010). Stability and chemical equilibrium of amphibole in calc-alkaline magmas: an overview, new thermobarometric formulations and application to subduction-related volcanoes. *Contributions to Mineralogy and Petrology* **160**, 45–66.

Rodriguez, C., Selles, D., Dungan, M., Langmuir, C. & Leeman, W. (2007). Adakitic dacites formed by intracrustal crystal fractionation of water-rich parent magmas at Nevado de Longav volcano (36.2 degrees S; Andean Southern Volcanic Zone, central Chile). *Journal of Petrology* **48**, 2033–2061.

Rooney, T. O., Franceschi, P. & Hall, C. M. (2011). Water-saturated magmas in the Panama Canal region: a precursor to adakite-like magma generation? *Contributions to Mineralogy and Petrology* **161**, 373–388.

Samaniego, P., Robin, C., Chazot, G., Bourdon, E. & Cotten, J. (2010). Evolving metasomatic agent in the Northern Andean subduction zone, deduced from magma composition of the long-lived Pichincha volcanic complex (Ecuador). *Contributions to Mineralogy and Petrology* **160**, 239–260.

Sato, M., Shuto, K., Uematsu, M., Takahashi, T., Ayabe, M., Takanashi, K., Ishimoto, H. & Kawabata, H. (2013). Origin of late oligocene to middle miocene adakitic andesites, high magnesian andesites and basalts from the back-arc margin of the SW and NE Japan arcs. *Journal of Petrology* **54**, 481–524.

Sengör, A. M. C., Natalin, B. A. & Burtman, V. S. (1993). Evolution of the altaid tectonic collage and paleozoic crustal growth in Eurasia. *Nature* **364**, 299–307.

Severs, M. J., Beard, J. S., Fedele, L., Hanchar, J. M., Mutchler, S. R. & Bodnar, R. J. (2009). Partitioning behavior of trace elements between dacitic melt and plagioclase, orthopyroxene, and clinopyroxene based on laser ablation ICPMS analysis of silicate melt inclusions. *Geochimica Et Cosmo chimica Acta* **73**, 2123–2141.

Shimizu, K., Liang, Y., Sun, C. G., Jackson, C. R. M. & Saal, A. E. (2017). Parameterized lattice strain models for REE partitioning between amphibole and silicate melt. *American Mineralogist* **102**, 2254–2267.

Shu, L. S., Wang, B., Zhu, W. B., Guo, Z. J., Charvet, J. & Zhang, Y. (2011). Timing of initiation of extension in the Tianshan, based on structural, geochemical and geochronological analyses of bimodal volcanism and olistostrome in the Bogda Shan (NW China). *International Journal of Earth Sciences* **100**, 1647–1663.

Sisson, T. W. & Grove, T. L. (1993). Experimental investigations of the role of H2O in calc-alkaline differentiation and subduction zone magmatism. *Contributions to Mineralogy and Petrology* **113**, 143–166.

Stracke, A., Hofmann, A. W. & Hart, S. R. (2005). FOZO, HIMU, and the rest of the mantle zoo. *Geochemistry, Geophysics, Geosystems* **6**, Q05007.

Streck, M. J., Leeman, W. P. & Chesley, J. (2007). High-magnesian andesite from Mount Shasta: A product of magma mixing and contamination, not a primitive mantle melt. *Geology* **35**, 351–354.

Su, C. Q., Jiang, C. Y., Xia, M. Z., Wei, W. & Pan, R. (2009). Geochemistry and zircons SHRIMP U–Pb age of volcanic rocks of Aqishan Formation in the eastern area of north Tianshan, *China. Acta Petrologica Sinica* **25**, 901–915 [in Chinese with English abstract].

Sun, S. S. & McDonough, W. F. (1989). Chemical and isotopic systematics of oceanic basalts: implications for mantle composition and processes. *Geological Society London Special Publications* **42**, 313–345.

Tang, D. M., Qin, K. Z., Li, C. S., Qi, L., Su, B. X. & Qu, W. J. (2011). Zircon dating, Hf-Sr–Nd-Os isotopes and PGE geochemistry of the Tianyu sulfide-bearing mafic-ultramafic intrusion in the Central Asian Orogenic Belt, NW China. *Lithos* **126**, 84–98.

Tang, G. J., Cawood, P. A., Wyman, D. A., Wang, Q. & Zhao, Z. H. (2017a). Evolving mantle sources in postcollisional early permian-triassic magmatic rocks in the heart of Tianshan Orogen (Western China). *Geochemistry, Geophysics, Geosystems* **18**, 4110–4122.

Tang, G. J., Chung, S. L., Wang, Q., Wyman, D. A., Dan, W., Chen, H. Y. & Zhao, Z. H. (2014). Petrogenesis of a Late Carboniferous mafic dike-granitoid association in the western Tianshan: Response to the geodynamics of oceanic subduction. *Lithos* **202-203**, 85–99.

Tang, G. J., Wang, Q., Wyman, D. A., Sun, M., Li, Z. X., Zhao, Z. H., Sun, W. D., Jia, X. H. & Jiang, Z. Q. (2010). Geochronology and geochemistry of Late Paleozoic magmatic rocks in the Lamasu-Dabate area, northwestern Tianshan (west China): Evidence for a tectonic transition from arc to post-collisional setting. *Lithos* **119**, 393–411.

Tang, G. J., Wang, Q., Wyman, D. A., Chung, S. L., Chen, H. Y. & Zhao, Z. H. (2017b). Genesis of pristine adakitic magmas by lower crustal melting: A perspective from amphibole composition. *Journal of Geophysical Research-Solid Earth* **122**, 1934–1948.

Tang, G. J., Wang, Q., Wyman, D. A., Li, Z. X., Xu, Y. G. & Zhao, Z. H. (2012). Metasomatized lithosphere-asthenosphere interaction during slab roll-back: Evidence from Late Carboniferous gabbros in the Luotuogou area. *Lithos* **155**, 67–80.

Tang, G. J., Wang, Q., Wyman, D. A., Sun, M., Li, Z. X., Zhao, Z. H., Sun, W. D., Jia, X. H. & Jiang, Z. Q. (2010). Geochronology and geochemistry of Late Paleozoic magmatic rocks in the Lamasu-Dabate area, northwestern Tianshan (west China): Evidence for a tectonic transition from arc to post-collisional setting. *Lithos* **119**, 393–411.

Tiepolo, M., Langone, A., Morishita, T., Yuhara, M. & Italy, P. (2012). On the recycling of amphibole-rich ultramafic intrusive rocks in the arc crust: Evidence from Shikanoshima Island (Kyushu, Japan). *Journal of Petrology* **53**, 1255–1285.

Tiepolo, M., Tribuzio, R. & Langone, A. (2011). High-Mg andesite petrogenesis by amphibole crystallization and ultramafic crust assimilation: Evidence from Adamello hornblendites (Central Alps, Italy). *Journal of Petrology* **52**, 1011–1045.

Tiepolo, M., Vannucci, R., Bottazzi, P., Oberti, R., Zanetti, A. & Foley, S. (2000). Partitioning of rare earth elements, Y, Th, U, and Pb between pargasite, kaersutite, and basanite to trachyte melts: Implications for percolated and veined mantle. *Geochemistry, Geophysics, Geosystems* **1, 2000GC000064**.

Tilmann, F., Ni, J., Hearn, T., Ma, Y. S., Rapine, R., Kind, R., Mechie, J., Saul, J., Haines, S., Klemperer, S., Brown, L., Pananont, P., Ross, A., Nelson, K. D., Guo, J. & Zhao, W. (2003). Seismic imaging of the downwelling Indian lithosphere beneath central Tibet. *Science* **300**, 1424–1427.

Ubide, T., Mollo, S., Zhao, J. X., Nazzari, M. & Scarlato, P. (2019). Sector-zoned clinopyroxene as a recorder of magma history, eruption triggers, and ascent rates. *Geochimica et Cosmochimica Acta* **251**, 265–283.

Ulmer, P., Kaegi, R. & Muntener, O. (2018). Experimentally derived intermediate to silica-rich arc magmas by fractional and equilibrium crystallization at 1.0 GPa: an evaluation of phase relationships, compositions, liquid lines of descent and oxygen fugacity. *Journal of Petrology* **59**, 11–58.

Ustunisik, G., Kilinc, A. & Nielsen, R. L. (2014). New insights into the processes controlling compositional zoning in plagioclase. *Lithos* **200**, 80–93.

Valley, J. W., Kinny, P. D., Schulze, D. J. & Spicuzza, M. J. (1998). Zircon megacrysts from kimberlite: oxygen isotope variability among mantle melts. *Contributions to Mineralogy and Petrology* **133**, 1–11.

Valley, J. W., Lackey, J. S., Cavosie, A. J., Clechenko, C. C., Spicuzza, M. J., Basei, M. A. S., Bindeman, I. N., Ferreira, V. P., Sial, A. N., King, E. M., Peck, W. H., Sinha, A. K. & Wei, C. S. (2005). 4.4 billion years of crustal maturation: oxygen isotope ratios of magmatic zircon. *Contributions to Mineralogy and Petrology* **150**, 561–580.

Vervoort, J. D., Patchett, P. J., Albarede, F., Blichert-Toft, J., Rudnick, R. & Downes, H. (2000). Hf-Nd isotopic evolution of the lower crust. *Earth and Planetary Science Letters* **181**, 115–129.

Wang, Q., McDermott, F., Xu, J. F., Bellon, H. & Zhu, Y. T. (2005). Cenozoic K-rich adakitic volcanic rocks in the Hohxil area, northern Tibet: lower-crustal melting in an intracontinental setting. *Geology* **33**, 465–468.

Wang, Q., Wyman, D. A., Xu, J. F., Jian, P., Zhao, Z. H., Li, C. F., Xu, W., Ma, J. L. & He, B. (2007a). Early cretaceous adakitic granites in the northern dabie complex, central China: Implications for partial melting and delamination of thickened lower crust. *Geochimica Et Cosmochimica Acta* **71**, 2609–2636.

Wang, Q., Wyman, D. A., Zhao, Z. H., Xu, J. F., Bai, Z. H., Xiong, X. L., Dai, T. M., Li, C. F. & Chu, Z. Y. (2007b). Petrogenesis of Carboniferous adakites and Nb-enriched arc basalts in the Alataw area, northern Tianshan Range (western China): Implications for Phanerozoic crustal growth in the Central Asia orogenic belt. *Chemical Geology* **236**, 42–64.

Wang, Q., Xu, J. F., Jian, P., Bao, Z. W., Zhao, Z. H., Li, C. F., Xiong, X. L. & Ma, J. L. (2006a). Petrogenesis of adakitic porphyries in an extensional tectonic setting, dexing, South China: Implications for the genesis of porphyry copper mineralization. *Journal of Petrology* **47**, 119–144.

Wang, Q., Zhao, Z. H., Xu, J. F., Wyman, D. A., Xiong, X. L., Zi, F. & Bai, Z. H. (2006b). Carboniferous adakite-high-Mg andesite-Nb-enriched basaltic rock suites in the Northern Tianshan area: Implications for Phanerozoic crustal growth in the Central Asia Orogenic Belt and Cu-Au mineralization. *Acta Petrologica Sinica* **22**, 11–30.

Wang, Y. H., Xue, C. J., Liu, J. J., Wang, J. P., Yang, J. T., Zhang, F. F., Zhao, Z. N., Zhao, Y. J. & Liu, B. (2015). Early Carboniferous adakitic rocks in the area of the Tuwu deposit, eastern Tianshan, NW China: Slab melting and implications for porphyry copper mineralization. *Journal of Asian Earth Sciences* **103**, 332–349.

Wang, Y. H., Xue, C. J., Liu, J. J. & Zhang, F. F. (2018). Origin of the subduction-related Carboniferous intrusions associated with the Yandong porphyry Cu deposit in eastern Tianshan, NW China: constraints from geology, geochronology, geochemistry, and Sr–Nd-Pb-Hf-O isotopes. *Mineralium Deposita* **53**, 629–647.

Wang, Y. H., Zhang, F. F., Liu, J. J. & Que, C. Y. (2016). Carboniferous magmatism and mineralization in the area of the Fuxing Cu deposit, Eastern Tianshan, China: Evidence from zircon U–Pb ages, petrogeochemistry, and Sr–Nd-Hf-O isotopic compositions. *Gondwana Research* **34**, 109–128.

Winchester, J. A. & Floyd, P. A. (1977). Geochemical discrimination of different magma series and their differentiation products using immobile elements. *Chemical Geology* **20**, 325–343.

Xia, B., Zhang, L. F. & Zhang, L. (2016). Petrogenesis and tectonic implications of Permian post-collisional granitoids in the Chinese southwestern Tianshan. *Journal of Asian Earth Sciences* **130**, 60–74.

Xia, L. Q., Xia, Z. C., Xu, X. Y., Li, X. M. & Ma, Z. P. (2008). Relative contributions of crust and mantle to the generation of the Tianshan Carboniferous rift-related basic lavas. *Journal of Asian Earth Sciences* **31**, 357–378.

Xia, L. Q., Xu, X. Y., Xia, Z. C., Li, X. M., Ma, Z. P. & Wang, L. S. (2004). Petrogenesis of Carboniferous rift-related volcanic rocks in the Tianshan, northwestern China. *Geological Society of America Bulletin* **116**, 419–433.

Xiao, B., Chen, H. Y., Hollings, P., Han, J. S., Wang, Y. F., Yang, J. T. & Cai, K. (2017). Magmatic evolution of the

Tuwu-Yandong porphyry Cu belt, NW China. *Gondwana Research* **43**, 74–91.

Xiao, W. J. & Santosh, M. (2014). The western Central Asian orogenic belt: A window to accretionary orogenesis and continental growth. *Gondwana Research* **25**, 1429–1444.

Xiao, W. J., Windley, B. F., Allen, M. B. & Han, C. M. (2013). Paleozoic multiple accretionary and collisional tectonics of the Chinese Tianshan orogenic collage. *Gondwana Research* **23**, 1316–1341.

Xie, H. J., Wu, G., Zhu, M. T., Zhong, W., Liu, J., Mei, M. & Wang, Y. W. (2013). Qiarbahete Sanukitoids and adakitic rocks in NW Tianshan: age and geochemical constraints on their petrogenesis and tectonic settings. *International Geology Review* **55**, 1941–1958.

Xie, W., Luo, Z. Y., Xu, Y. G., Chen, Y. B., Hong, L. B., Ma, L. & Ma, Q. (2016a). Petrogenesis and geochemistry of the Late Carboniferous rear-arc (or back-arc) pillow basaltic lava in the Bogda Mountains. *Lithos* **244**, 30–42.

Xie, W., Xu, Y. G., Chen, Y. B., Luo, Z. Y., Hong, L. B., Ma, L. & Liu, H. Q. (2016b). High-alumina basalts from the Bogda Mountains suggest an arc setting for Chinese Northern Tianshan during the Late Carboniferous. *Lithos* **256-257**, 165–181.

Xiong, X. L., Adam, J. & Green, T. H. (2005a). Rutile stability and rutile/melt HFSE partitioning during partial melting of hydrous basalt: implications for TTG genesis. *Chemical Geology* **218**, 339–359.

Xiong, X. L., Cai, Z. Y., Niu, H. C., Chen, Y. B., Wang, Q., Zhao, Z. H. & Wu, J. H. (2005b). The late Paleozoic adakites in eastern Tianshan area and their metallogenetic significance. *Acta Petrologica Sinica* **21**, 967–976 [in Chinese with English abstract].

Xu, J. F., Shinjo, R., Defant, M. J., Wang, Q. & Rapp, R. P. (2002). Origin of Mesozoic adakitic intrusive rocks in the Ningzhen area of east China: Partial melting of delaminated lower continental crust? *Geology* **30**, 1111–1114.

Xu, X. Y., Wang, H. L., Li, P., Chen, J. L., Ma, Z. P., Zhu, T., Wang, N. & Dong, Y. P. (2013). Geochemistry and geochronology of Paleozoic intrusions in the nalati (Narati) area in Western Tianshan, Xinjiang, China: "implications for Paleozoic tectonic evolution. *Journal of Asian Earth Sciences* **72**, 33–62.

Xue, S. C., Li, C., Qin, K. Z. & Tang, D. M. (2016). A non-plume model for the Permian protracted (266-286 Ma) basaltic magmatism in the Beishan-Tianshan region, Xinjiang, Western China. *Lithos* **256-257**, 243–249.

Yan, Y. H., Xue, C. J., Zhang, Z. C., Ding, Z. X., Yang, W. H. & Han, Z. H. (2013). Geochemistry and genesis of the Qunjisayi granite porphyry in the west of Awulale area, Western Tianshan Mountains. *Acta Petrologica Et Mineralogica* **32**, 139–153 [in Chinese with English abstract].

Yang, W. B., Niu, H. C., Shan, Q., Luo, Y., Sun, W. D., Li, C. Y., Li, N. B. & Yu, X. Y. (2012). Late Paleozoic calc-alkaline to shoshonitic magmatism and its geodynamic implications, Yuximolegai area, western Tianshan, Xinjiang. *Gondwana Research* **22**, 325–340.

Ye, H. M., Ye, X. T. & Zhang, C. L. (2013). Geochemistry and geodynamic implications of Nileke Permian volcanic rocks in Western Tianshan, NW China. *Acta Petrologica Sinica* **29**, 3389–3401 [in Chinese with English abstract].

Yin, J. Y., Chen, W., Xiao, W. J., Yuan, C., Long, X. P., Cai, K. D. & Zhang, B. (2016). Late Carboniferous adakitic granodiorites in the Qiongkusitai area, western Tianshan, NW China: Implications for partial melting of lower crust in the southern Central Asian Orogenic Belt. *Journal of Asian Earth Sciences* **124**, 42–54.

Yin, J. Y., Chen, W., Xiao, W. J., Yuan, C., Zhang, B., Cai, K. D. & Long, X. P. (2017). Geochronology, petrogenesis, and tectonic significance of the latest Devonian-early Carboniferous I-type granites in the Central Tianshan, NW China. *Gondwana Research* **47**, 188–199.

Yogodzinski, G. M. & Kelemen, P. B. (1998). Slab melting in the Aleutians: implications of an ion probe study of clinopyroxene in primitive adakite and basalt. *Earth and Planetary Science Letters* **158**, 53–65.

Yu, X., Yang, S. F., Chen, H. L., Chen, Z. Q., Li, Z. L., Batt, G. E. & Li, Y. Q. (2011). Permian flood basalts from the Tarim Basin, Northwest China: SHRIMP zircon U–Pb dating and geochemical characteristics. *Gondwana Research* **20**, 485–497.

Zellmer, G. F., Iizuka, Y., Miyoshi, M., Tamura, Y. & Tatsumi, Y. (2012). Lower crustal H2O controls on the formation of adakitic melts. *Geology* **40**, 487–490.

Zhang, C. L. & Zou, H. B. (2013a). Comparison between the Permian mafic dykes in Tarim and the western part of Central Asian Orogenic Belt (CAOB), NW China: Implications for two mantle domains of the Permian Tarim Large Igneous Province. *Lithos* **174**, 15–27.

Zhang, C. L. & Zou, H. B. (2013b). Permian A-type granites in Tarim and western part of Central Asian Orogenic Belt (CAOB): Genetically related to a common Permian mantle plume? *Lithos* **172-173**, 47–60.

Zhang, C. L., Zou, H. B., Yao, C. Y. & Dong, Y. G. (2014). Origin of Permian gabbroic intrusions in the southern margin of the Altai Orogenic belt: A possible link to the Permian Tarim mantle plume? *Lithos* **204**, 112–124.

Zhang, J., Humphreys, M. C. S., Cooper, G. F., Davidson, J. P. & Macpherson, C. G. (2017). Magma mush chemistry at subduction zones, revealed by new melt major element inversion from calcic amphiboles. *American Mineralogist* **102**, 1353–1367.

Zhang, L., Ren, Z. Y., Xia, X. P., Li, J. & Zhang, Z. F. (2015). IsotopeMaker: A Matlab program for isotopic data reduction. *International Journal of Mass Spectrometry* **392**, 118–124.

Zhang, L. C., Xiao, W. J., Qin, K. Z. & Zhang, Q. (2006). The adakite connection of the Tuwu-Yandong copper porphyry belt, eastern Tianshan, NW China: trace element and Sr–Nd-Pb isotope geochemistry. *Mineralium Deposita* **41**, 188–200.

Zhang, Y. Y., Yuan, C., Sun, M., Li, J., Long, X. P., Jiang, Y. D. & Huang, Z. Y. (2020). Molybdenum and boron isotopic evidence for carbon-recycling via carbonate dissolution in subduction zones. *Geochimica Et Cosmochimica Acta* **278**, 340–352.

Zhao, J. (2013). Study on the metallogenic settings and metallogenic regularity of copper deposits in western Awulale Mountain, Xinjiang. Ph.D. dissertation of Chang'an University, pp. 1–151 (in Chinese with English abstract).

Zhao, Z. H., Bai, Z. H., Xiong, X. L., Mei, H. J. & Wang, Y. X. (2003). 40Ar/39Ar chronological study of Late Paleozoic volcanic-hypabyssal igneous rocks in western Tianshan, Xinjiang. *Geochimica* **32**, 317–327 [in Chinese with English abstract].

Zhao, Z. H., Xiong, X. L., Wang, Q., Wyman, D. A., Bao, Z. W., Bai, Z. H. & Qiao, Y. L. (2008). Underplating-related adakites in Xinjiang Tianshan. *Lithos* **102**, 374–391.

Zheng, J., Griffin, W. L., O'Reilly, S. Y., Zhang, M., Pearson, N. & Luo, Z. (2006). The lithospheric mantle beneath the southwestern Tianshan area, northwest China. *Contributions to Mineralogy and Petrology* **151**, 457–479.

Zheng, J. H., Mao, J. W., Chai, F. M. & Yang, F. Q. (2016). Petrogenesis of permian a-type granitoids in the Cihai iron ore district, Eastern Tianshan, NW China: Constraints on the timing of iron mineralization and implications for a non-plume tectonic setting. *Lithos* **260**, 371–383.

Zhu, Y. F., Guo, X. & Zhou, J. (2006a). Petrology and geochemistry of a. +epsilon(Nd) gabbro body in Baluntai region, central Tianshan mountains, *Xinjiang. Acta Petrologica Sinica* **22**, 1178–1192 [in Chinese with English abstract].

Zhu, Y. F., Zhou, J. & Guo, X. A. (2006b). Petrology and Sr–Nd isotopic geochemistry of the Carboniferous volcanic rocks in the western Tianshan Mountains, NW China. *Acta Petrologica Sinica* **22**, 1341–1350 [in Chinese with English abstract].

Zonenshain, L. P., Kuzmin, M. I. & Natapov, L. M. (1990). *Geology of the USSR: A Plate Tectonic Synthesis, Geodynamic Series*. Washington, DC: American Geophysical Union.